

The Pennsylvania State University

The Graduate School

MESOSCALE ATMOSPHERIC SIMULATIONS
OF MARINE-LAYER STRUCTURE AND REFRACTIVITY
IN THE SOUTHERN CALIFORNIA BIGHT

A Thesis in

Meteorology

by

Robert Travis Williams, Jr.

Submitted in Partial Fulfillment
of the Requirements
for the Degree of

Master of Science

August 1997



19970625 028

REPORT DOCUMENTATION PAGE

Form Approved
OMB No. 0704-0188

Public reporting burden for this collection of information is estimated to average 1 hour per response, including the time for reviewing instructions, searching existing data sources, gathering and maintaining the data needed, and completing and reviewing the collection of information. Send comments regarding this burden estimate or any other aspect of this collection of information, including suggestions for reducing this burden, to Washington Headquarters Services, Directorate for Information Operations and Reports, 1215 Jefferson Davis Highway, Suite 1204, Arlington, VA 22202-4302, and to the Office of Management and Budget, Paperwork Reduction Project (0704-0188), Washington, DC 20503.

1. AGENCY USE ONLY (Leave blank)			2. REPORT DATE	3. REPORT TYPE AND DATES COVERED
			18 JUN 97	
4. TITLE AND SUBTITLE MESOSCALE ATMOSPHERIC SIMULATIONS OF MARINE-LAYER STRUCTURE AND REFRACTIVITY IN THE SOUTHERN CALIFORNIA BIGHT			5. FUNDING NUMBERS	
6. AUTHOR(S) ROBERT TRAVIS WILLIAMS				
7. PERFORMING ORGANIZATION NAME(S) AND ADDRESS(ES) PENNSYLVANIA STATE UNIVERSITY			8. PERFORMING ORGANIZATION REPORT NUMBER 97-062	
9. SPONSORING/MONITORING AGENCY NAME(S) AND ADDRESS(ES) DEPARTMENT OF THE AIR FORCE AFIT/CI 2950 P STREET WRIGHT-PATTERSON AFB OH 45433-7765			10. SPONSORING/MONITORING AGENCY REPORT NUMBER	
11. SUPPLEMENTARY NOTES				
12a. DISTRIBUTION AVAILABILITY STATEMENT			12b. DISTRIBUTION CODE	
13. ABSTRACT (Maximum 200 words)				
14. SUBJECT TERMS			15. NUMBER OF PAGES 114	
			16. PRICE CODE	
17. SECURITY CLASSIFICATION OF REPORT	18. SECURITY CLASSIFICATION OF THIS PAGE	19. SECURITY CLASSIFICATION OF ABSTRACT	20. LIMITATION OF ABSTRACT	

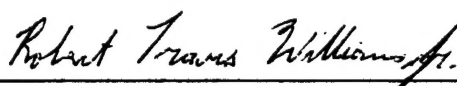
ABSTRACT

Calculation of electromagnetic (EM) propagation in the littoral (marine coastal zone) can be a challenging problem for current numerical propagation models because of the sparsity of meteorological data necessary to describe the propagation medium. Advanced mesoscale atmospheric numerical models, however, represent a potentially important additional source of information to assist in the determination of the refractivity structure. These meteorological models are capable of predicting high-resolution three dimensional fields of water vapor, temperature, and pressure, which determine the refractivity. Due to inadequate resolution, lack of initial data, and poor representation of physical processes, previous meteorological models have been unable to predict all required details of the refractivity structure. It is believed, however, that with sufficient improvement such models can simulate characteristics of the marine boundary layer depth, inversion height, and inversion strength, on temporal scales from an hour to several days. It may also be possible to estimate the sub-grid scale statistics of the critical fields.

The Penn State/National Center for Atmospheric Research non-hydrostatic mesoscale model (MM5) is used to test the predictability of marine temperature and moisture structures in the coastal zone of Southern California during the VOCAR (Variability of Coastal Atmospheric Refractivity) experiment of 1993. Hundreds of soundings taken at several sites in the VOCAR study area are analyzed to characterize the dependence of atmospheric refractivity and marine-layer structure on time of day and distance offshore. High-vertical resolution numerical simulations are performed using MM5 and are evaluated against the special data over a period of about one week. The

ability of a mesoscale numerical model to predict both short-term (1-6 hours) and longer-range (days) variations in marine-layer structure and refractivity is demonstrated. The major conclusions are that the numerical model is capable of predicting (1) the basic evolution of marine boundary layer depth over a period of 7 days, (2) inversion structures in temperature and water vapor that account for the observed strength of trapping and ducting layers in the refractivity (M) profiles, and (3) gravity wave propagation in and above the marine boundary layer that affects the strength/existence of the trapping layer and the elevated/surface wave ducting layer on time scales of 1-4 hours.

I grant The Pennsylvania State University the nonexclusive right to use this work for the University's own purposes and to make single copies of the work available to the public on a not-for-profit basis if copies are not otherwise available.



Robert Travis Williams, Jr.

We approve the thesis of Robert Travis Williams, Jr.

Date of Signature

Nelson L. Seaman

Nelson L. Seaman
Assistant Professor of Meteorology
Thesis Advisor

May 8, 1997

George S. Young

George S. Young
Associate Professor of Meteorology

May 8, 1997

Dennis W. Thomson

Dennis W. Thomson
Professor of Meteorology
Head of the Department of Meteorology

12 May 97

TABLE OF CONTENTS

LIST OF FIGURES.....	vi
LIST OF TABLES	xv
ACKNOWLEDGMENTS	xvi
Chapter 1. INTRODUCTION.....	1
1.1 Statement of the Problem	1
1.2 Atmospheric Refraction.....	3
1.3 The Marine Boundary Layer.....	9
1.4 Thesis Objectives	15
Chapter 2. MODEL DESCRIPTION.....	17
2.1 The PSU/NCAR Mesoscale Model Version 5.1.....	17
2.2 Computational Domains.....	18
2.3 Model Physics	21
Chapter 3. EXPERIMENTAL DESIGN	26
3.1 Dynamic Initialization.....	26
3.1.1 Multiscale Four-Dimensional Data Assimilation	27
3.1.2 Marine Boundary Layer Initialization	29
3.2 Model Physics.....	30
Chapter 4. CASE DESCRIPTION.....	37
4.1 Observed Synoptic Scale Conditions	37
4.2 Refractive Conditions.....	54
Chapter 5. EXPERIMENTAL RESULTS	64
5.1 Synoptic Scale Results	64
5.2 Mesoscale Results (25 August, 1200z - 27 August, 1200z).....	81
5.3 Gravity Waves.....	97
Chapter 6. SUMMARY AND CONCLUSIONS.....	107
REFERENCES.....	112

LIST OF FIGURES

Figure 1.1	Modified Refractivity Profiles for a Standard Atmosphere (dashed) and for San Nicolas Island, 24 Aug 1993, 1200Z (solid). The trapping layer (dark stipple) occurs where $dM/dz < 0$. The duct (light stipple) extends from M_{min} to the point on the M profile directly below M_{min}	8
Figure 1.2	Observed soundings measured by aircraft as part of ASTEX on 0000 UTC 13 June 1992 northeast of Santa Maria Island in the Azores: (a) temperature (K), (b) wind speed ($m s^{-1}$), (c) liquid water content ($g kg^{-1}$), and (d) total water content ($g kg^{-1}$). Data points are horizontally averaged values of aircraft data measured as part of the same study. (Duynkerke et al. 1995).....	10
Figure 1.3	Area called the Southern California Bight, location of the Variability of Coastal Atmospheric Refractivity (VOCAR) experiment. (Aug/Sep 1993).....	11
Figure 1.4	Observed climatological height of inversion base in summer over the northeast Pacific from Neiburger et al. (1961) (hundreds of meters). Contour interval is 200m.....	12
Figure 1.5	Observed average summer cross section of temperature ($^{\circ}C$) from San Francisco to Honolulu. Subtropical inversion layer is shown by stippled shading and contour interval is $2^{\circ}C$. (Neiburger et al. 1961).....	13
Figure 1.6	Percentage of observations with no inversion during the months June-September. (Neiburger et al. 1961).....	14
Figure 2.1	Model grids for this study on a Lambert conformal projection. Coarse Grid Mesh (CGM) standard latitudes are 30 N and 60 N and central longitude is 120 W.....	20
Figure 3.1	Simulated west-east cross section through San Nicolas Island depicting the MBL structure at the end of a pre-forecast period without the MBL initialization scheme (Valid: 25 August 1993, 0000 Z). Potential temperature is solid, 1 K contours, and water vapor mixing ratio is dashed; $1 g kg^{-1}$ contours	31

Figure 3.2	Simulated west-east cross section through San Nicolas Island depicting the MBL structure at the end of a pre-forecast period with Leidner's MBL initialization scheme (Valid: 25 August 1993, 0000 Z). Potential temperature is solid, 1 K contours, and water vapor mixing ratio is dashed; 1 g kg ⁻¹ contours	32
Figure 3.3	San Nicolas Island observed Skew-T diagram, 0000z, 25 August, 1993. The sharp gradients in temperature and moisture near 960 mb mark the top of the MBL.	33
Figure 3.4	Simulated west-east cross section through Vandenburg 4 August 1990, 1200 Z. Cross section is a 12-h forecast from 4-km mesh using normal values of background vertical diffusion (1.0 m ² s ⁻¹). Potential temperature is solid, 1 K contours, and water vapor mixing ratio is dashed; 1 g kg ⁻¹ contours (Leidner 1995)	35
Figure 3.5	Simulated west-east cross section through Vandenburg 4 August 1990, 1200 Z. Cross section is a 12-h forecast from 4-km mesh using reduced background vertical diffusion (0.1 m ² s ⁻¹). Potential temperature is solid, 1 K contours, and water vapor mixing ratio is dashed; 1 g kg ⁻¹ contours (Leidner 1995).....	36
Figure 4.1	500 mb Geopotential Height (GPH) Analysis, 1200z, 24 August 1993. The East Pacific Ridge axis is along 140° W longitude with troughing over the northwestern United States. Locations used for Figs. 4.4 and 5.3 are marked by heavy dots.	38
Figure 4.2	500 mb Geopotential Height Analysis, 1200z, 27 August 1993. The East Pacific Ridge axis extends to the northwest and southeast from the High at 132° W longitude. This time corresponds to the period of strongest subsidence.	39
Figure 4.3	500 mb Geopotential Height Analysis, 1200z, 31 August 1993. The East Pacific Ridge has weakened and the High has moved to the northwest. A belt of lower heights extends from northern California to Hawaii.....	40
Figure 4.4	Time series of 500 mb GPH for three locations (see heavy dot, Fig 4.1) approximately 450 km west of the California coast. Values are from the 1200z analysis for each day of the case period, 24-31 August 1993.....	41

Figure 4.5	Sea Level Pressure (SLP) analysis, 1200z, 24 August 1993. The East Pacific High is located at 140° W longitude while Tropical Storm Hilary is just off the Baja peninsula. Inverted troughing extends from T. S. Hilary up into northern California.....	43
Figure 4.6	Sea Level Pressure (SLP) analysis, 1200z, 27 August 1993. The East Pacific High has moved slightly to the southeast and the remains of Hilary are in the northern Gulf of California. Inverted troughing over California persists, but the pressure gradient has weakened west of San Francisco.....	44
Figure 4.7	Sea Level Pressure (SLP) analysis, 1200z, 31 August 1993. The East Pacific High has moved nearly 9° latitude to the north. A synoptic scale Low has formed off the California coast with another Low pressure system in the northern Gulf of California.....	45
Figure 4.8	Storm track for Tropical Storm Hilary during the case period. The 12z positions are plotted using standard meteorological symbols.....	46
Figure 4.9	850 mb Wind analysis, 1200z, 24 August 1993. Note the cyclonic circulation southwest of the VOCAR region and southerly flow off the coast of the Baja Peninsula.....	47
Figure 4.10	850 mb Wind analysis, 1200z, 25 August 1993. The cyclonic circulation southwest of the VOCAR region has moved to the north. Weak southerly flow exists west of extreme northern Mexico. Tropical Storm Hilary is seen near 25° N.....	48
Figure 4.11	850 mb Wind analysis, 1200z, 26 August 1993. Hilary, now a tropical depression, is near 27.5° N. The flow pattern from Hilary is advecting moisture into the VOCAR region, which exhibits southerly flow.....	49
Figure 4.12	San Nicolas Island observed Skew-T diagram, 1200z, 24 August, 1993. The sharp gradients in temperature and moisture near 960 mb mark the top of the MBL. Winds flow is southerly in a deep layer above the MBL.....	50
Figure 4.13	San Nicolas Island observed Skew-T diagram, 1200z, 25 August, 1993. Note the moistening of the layer from 700-810 mb. Also, the deep layer of southerly flow above the MBL persists.....	51

Figure 4.14	San Nicolas Island observed Skew-T diagram, 1200z, 26 August, 1993. Moistening of the atmosphere above the MBL continues, resulting in a shallow dry layer just above the MBL. Also, the inversion base has lowered to around 985 mb	52
Figure 4.15	San Nicolas Island observed Skew-T diagram, 1200z, 27 August, 1993. The deep layer of southerly flow has evolved into easterly flow from 620-780 mb. The remarkably thin dry layer atop the MBL persists and the inversion base is near 1000 mb	53
Figure 4.16	Observed refractive structure at San Nicolas Island during the case period. Time is along the abscissa, height in meters MSL is along the ordinate. Dark shading represents the trapping layer. The ducting layer extends from the trapping layer top to the bottom edge of the light shaded region.....	56
Figure 4.17	Observed refractive structure at San Clemente Island during the case period. Time is along the abscissa, height in meters MSL is along the ordinate. Dark shading represents the trapping layer. The ducting layer extends from the trapping layer top to the bottom edge of the light shaded region.....	57
Figure 4.18	Observed refractive structure at the Research Vessel Pt. Sur during the case period. Time is along the abscissa, height in meters MSL is along the ordinate. Dark shading represents the trapping layer. The ducting layer extends from the trapping layer top to the bottom edge of the light shaded region.....	58
Figure 4.19	Observed refractive structure at Camp Pendleton during the case period. Time is along the abscissa, height in meters MSL is along the ordinate. Dark shading represents the trapping layer. The ducting layer extends from the trapping layer top to the bottom edge of the light shaded region.....	59
Figure 4.20	Time/Height plot of the observed duct base at: San Nicolas Island (NSI), San Clemente Island (NUC), Research Vessel Pt. Sur (SUR), and Camp Pendleton (CPN). Time is along the abscissa, height in meters AGL is along the ordinate. Note, plots on the abscissa indicate the presence of a surface duct.....	60
Figure 4.21	Time/Height plot of the observed trapping layer base at: San Nicolas Island (NSI), San Clemente Island (NUC), Research Vessel Pt. Sur (SUR), and Camp Pendleton (CPN). Time is along the abscissa, height in meters MSL is along the ordinate.....	61

Figure 4.22	Time/Height plot of the observed trapping layer top at: San Nicolas Island (NSI), San Clemente Island (NUC), Research Vessel Pt. Sur (SUR), and Camp Pendleton (CPN). Time is along the abscissa, height in meters MSL is along the ordinate. Note, the trapping layer top is coincident with the top of the EM duct.....	62
Figure 5.1	Simulated 500 mb GPH, 1200z, 27 August, 1993. The East Pacific Ridge axis extends to the northwest and southeast from the High at 133° W longitude.....	65
Figure 5.2	Simulated 500 mb GPH, 1200z, 31 August, 1993. The East Pacific Ridge has weakened and the High has moved to the northwest. A belt of lower heights extends from northern California to Hawaii.	67
Figure 5.3	Time series of simulated 500 mb GPH for the same locations in Fig. 4.4. The model has captured the synoptic scale trend in 500 mb GPH with a maximum error of only 20 m.....	68
Figure 5.4	Location of cross-sections used in Chapter 5. Tick marks are hundreds of kilometers from the north, west, or southwest end of the respective cross-sections. The box delineates the area over which the vertical velocities were averaged for the profiles in Figs. 5.6-5.8.....	69
Figure 5.5	San Nicolas Island vertical velocity profiles for 28 August, 0000z. The unaveraged profile is the dashed line while the spatially and temporally averaged profile is the solid line. Vertical velocity ($m s^{-1}$) is plotted on the abscissa and height MSL (m) is plotted on the ordinate.....	71
Figure 5.6	Averaged vertical velocity profiles at San Nicolas Island. The left hand graph is for 25 August 1993. The right hand graph is for 26 August 1993. The solid line is 0000z and the dashed line is 1200z. Vertical velocity ($m s^{-1}$) is plotted on the abscissa and height MSL (m) is plotted on the ordinate.....	72
Figure 5.7	Averaged vertical velocity profiles at San Nicolas Island. The left hand graph is for 27 August 1993. The right hand graph is for 28 August 1993. The solid line is 0000z and the dashed line is 1200z. Vertical velocity ($m s^{-1}$) is plotted on the abscissa and height MSL (m) is plotted on the ordinate.....	73

Figure 5.8	Averaged vertical velocity profiles at San Nicolas Island. The left hand graph is for 29 August 1993. The right hand graph is for 30 August 1993. The solid line is 0000z and the dashed line is 1200z. Vertical velocity ($m s^{-1}$) is plotted on the abscissa and height MSL (m) is plotted on the ordinate.....	74
Figure 5.9	(a) Vertical motion of the observed trapping layer, simulated trapping layer, and simulated vertical velocity at the mid-point of the simulated trapping layer at San Nicolas Island. (b) Fourier representation filtering out temporal variations less than 16 hours in scale.....	75
Figure 5.9	(c) Vertical motion of the observed trapping layer and simulated vertical velocity at the mid-point of the observed trapping layer at Camp Pendleton. (d) Fourier representation filtering out temporal variations less than 16 hours in scale.....	76
Figure 5.10	Simulated refractive structure at San Nicolas Island during the case period. Time is along the abscissa, height in meters MSL is along the ordinate. Dark shading represents the trapping layer. The ducting layer extends from the trapping layer top to the bottom edge of the light shaded region.....	78
Figure 5.11	Simulated refractive structure at San Clemente Island during the case period. Time is along the abscissa, height in meters MSL is along the ordinate. Dark shading represents the trapping layer. The ducting layer extends from the trapping layer top to the bottom edge of the light shaded region.....	79
Figure 5.12	Simulated refractive structure at Camp Pendleton during the case period. Time is along the abscissa, height in meters MSL is along the ordinate. Dark shading represents the trapping layer. The ducting layer extends from the trapping layer top to the bottom edge of the light shaded region.....	80
Figure 5.13	North to south cross-section (25 August, 1200z) of simulated water vapor mixing ratio (top, contour interval $1.0 g kg^{-1}$), simulated vertical velocity (bottom, contour interval $0.5 cm s^{-1}$), and wind vectors in the plane. Note: positive vertical velocities (solid), negative vertical velocities (dashed).....	83

Figure 5.14	North to south cross-section (26 August, 1200z) of simulated water vapor mixing ratio (top, contour interval 1.0 g kg^{-1}), simulated vertical velocity (bottom, contour interval 0.5 cm s^{-1}), and wind vectors in the plane. Note: positive vertical velocities (solid), negative vertical velocities (dashed).	85
Figure 5.15	North to south cross-section (27 August, 1200z) of simulated water vapor mixing ratio (top, contour interval 1.0 g kg^{-1}), simulated vertical velocity (bottom, contour interval 0.5 cm s^{-1}), and wind vectors in the plane. Note: positive vertical velocities (solid), negative vertical velocities (dashed).	86
Figure 5.16	San Nicolas Island simulated Skew-T diagram, 1200z, 25 August, 1993. Note the MBL top is near 950 mb with low level northwesterly flow and southwesterly flow just above the MBL.	87
Figure 5.17	San Nicolas Island simulated Skew-T diagram, 1200z, 26 August, 1993. Moistening of the atmosphere above the MBL continues, resulting in a shallow dry layer just above the MBL. Also, the inversion base has lowered to around 975 mb.	88
Figure 5.18	San Nicolas Island simulated Skew-T diagram, 1200z, 27 August, 1993. The deep layer of southerly flow has evolved into easterly flow from 580-925 mb. The remarkably thin dry layer atop the MBL persists and the inversion base is near 1000 mb.	89
Figure 5.19	Observed (solid) and simulated (dashed) modified refractivity profiles for San Nicolas Island, 25 August, 1200z. An elevated duct exists from approximately 180-550 m. (b_o is the observed duct base, b_s is the simulated duct base)....	90
Figure 5.20	Observed (solid) and simulated (dashed) modified refractivity profiles for San Nicolas Island, 26 August, 1200z. A surface duct extends to approximately 415 m. The simulated profile is after 36 hrs of integration. (b_o is the observed duct base, b_s is the simulated duct base)....	92
Figure 5.21	Observed (solid) and simulated (dashed) modified refractivity profiles for San Nicolas Island, 27 August, 1200z. A surface duct extends to approximately 220 m. The simulated profile is after 60 hrs of integration. (b_o is the observed duct base, b_s is the simulated duct base)....	93

Figure 5.22	North to south cross-section of simulated modified refractivity (top, contour interval 10 M units), simulated trapping layer (top, dashed), and simulated refractive structure (bottom, trapping layer is the dark band, EM duct is the light band) on 25 August, 1200z.	94
Figure 5.23	North to south cross-section of simulated modified refractivity (top, contour interval 10 M units), simulated trapping layer (top, dashed), and simulated refractive structure (bottom, trapping layer is the dark band, EM duct is the light band) on 26 August, 1200z.	95
Figure 5.24	North to south cross-section of simulated modified refractivity (top, contour interval 10 M units), simulated trapping layer (top, dashed), and simulated refractive structure (bottom, trapping layer is the dark band, EM duct is the light band) on 27 August, 1200z.	96
Figure 5.25	Southwest to Northeast cross-section through Baja of simulated modified refractivity (top, contour interval 10 M units), simulated trapping layer (top, dashed), simulated vertical velocity (bottom, contour interval 0.5 cm s^{-1}), and wind vectors in the plane on 27 August, 0700z. Note: positive vertical velocities (solid), negative vertical velocities (dashed).	98
Figure 5.26	Southwest to Northeast cross-section through Baja of simulated modified refractivity (top, contour interval 10 M units), simulated trapping layer (top, dashed), simulated vertical velocity (bottom, contour interval 0.5 cm s^{-1}), and wind vectors in the plane on 27 August, 1000z. Note: positive vertical velocities (solid), negative vertical velocities (dashed).	99
Figure 5.27	Wind field at 400 m AGL on 26 August, 1800z. The region of strongest velocities is over the Baja Peninsula. Isotach contour interval is 5 m s^{-1}	101
Figure 5.28	Wind field at 400 m AGL on 27 August, 0000z. The region of strongest velocities is over the Baja Peninsula. Isotach contour interval is 5 m s^{-1}	102
Figure 5.29	Wind field at 400 m AGL on 27 August, 0600z. The region of strongest velocities is over the Baja Peninsula. Isotach contour interval is 5 m s^{-1}	103

Figure 5.30 West to East cross-section through San Nicolas Island of simulated modified refractivity (top, contour interval 10 M units), simulated trapping layer (top, dashed), simulated vertical velocity (bottom, contour interval 0.5 cm s^{-1}), and wind vectors in the plane on 27 August, 0700z. Note: positive vertical velocities (solid), negative vertical velocities (dashed) 105

Figure 5.31 West to East cross-section through San Nicolas Island of simulated modified refractivity (top, contour interval 10 M units), simulated trapping layer (top, dashed), simulated vertical velocity (bottom, contour interval 0.5 cm s^{-1}), and wind vectors in the plane on 27 August, 0900z. Note: positive vertical velocities (solid), negative vertical velocities (dashed) 106

LIST OF TABLES

Table 1.1	Layer Refractive Values and Properties.....	6
Table 2.1	MM5v1 Prognostic Field Summary.....	19
Table 2.2	VOCAR Computational Grid Summary	19
Table 2.3	Vertical Distribution of Computational Layers	22

ACKNOWLEDGMENTS

I am grateful for Dr. Nelson L. Seaman's valuable advice, guidance, and encouragement throughout my degree program. His quiet patience, strong leadership, and gentle understanding during the course of this research project will always be remembered. I also appreciate the many enlightening conversations with Dr. David R. Stauffer, whose keen insight into everything from marine boundary layer structure to MM5 kept me out of trouble on several occasions. For Dr. George S. Young and Captain David J. Beberwyk, thank you for your encouragement and for helping me maintain the proper perspective. I am very thankful for the United States Air Force's sponsorship of my degree program and the United States Navy's research funding under contract No. N00039-92-C-0100. A special note of thanks is extended to Glenn Hunter for the many times he tolerated my rambling questions and for his adept ability to set me on the right path again. My warmest and deepest debt of gratitude, however, is reserved for Toni (my wife), Jacob (my son), and Kelly (my daughter) -- thank you for enduring my frustrations and sharing my successes. Finally, I praise my Lord and Savior, Jesus Christ, for His precious gift of salvation, His unfailing strength, and for the individuals mentioned above, may He bless them richly.

Chapter 1

INTRODUCTION

1.1 Statement of the Problem

Since the early days of radio communications and the first implementation of radar to detect enemy aircraft in World War II, operators of these systems noted degraded performance in certain geographical areas and at certain times of day. Modern users of systems which rely on the transmission and reception of electromagnetic energy encompass military, civilian, and scientific communities. Most operators of such systems recognize atmospheric refraction as an important source of this degradation. For example, meteorologists have long encountered anomalous propagation behavior under certain circumstances in their attempts to remotely sense the atmosphere. Aviators experience the same type of sensor degradation when engaged in low-level flight in certain locations and at certain times of day. Finally, ships at sea routinely experience poor radar performance as a result of atmospheric refraction in the marine boundary layer (MBL). Propagation assessment systems for shipboard use have been developed to mitigate these effects (Hittney and Richter 1976).

Temporally and spatially varying 3-D meteorological fields impact the atmosphere's 3-D refractive index field, causing refraction of electromagnetic (EM) waves propagating through the atmosphere. EM propagation models accurately predict the behavior of propagating radio waves and microwaves given appropriate values of total atmospheric pressure (p), temperature (T), and atmospheric vapor pressure (e).

Traditionally, EM propagation modeling has used instantaneous meteorological data obtained from point source rawinsondes interpolated or extrapolated along the propagation path to represent conditions for the entire propagation domain (Richter 1994). Using these extremely sparse data, numerical propagation codes generate less than adequate Modified Refractivity (M) profiles to describe the 3-D structure of M fields.

This problem is exacerbated in data void areas, especially over the oceans and in the littorals. Coincidentally, the oceanic and littoral regions are precisely where the most detailed M structure is required due to the impact atmospheric refraction has on coastal defense radar and naval forces at sea. It is the sharp vertical gradients in moisture, and temperature under inversion conditions, which produce atmospheric ducting. Superior representation of meteorological conditions in these regions is therefore quite critical. Specifically, one would expect meteorological conditions conducive for EM ducting in regions typified by Marine Boundary Layers (MBL) capped by large scale subsidence. These conditions are prevalent in the summertime Eastern Pacific ocean, including the Southern California Bight.

One further complication in the analysis and prediction of accurate M profiles in these regions is the generally poor performance of mesoscale meteorological models in representing MBL structure. This poor performance is tied to numerous factors. Foremost, sparse data availability over the oceans and in the littorals results in less than ideal mesoscale model initial conditions. Second, insufficient vertical resolution in many mesoscale models presents two problems associated with MBL accuracy. Turbulent kinetic energy (TKE) submodels require 50 m vertical resolution to capture the internal

MBL structure (Bechtold et al. 1992, Duynkerke and Hignett 1993, Bretherton 1994).

Also, Davies and Alves (1989), demonstrate 10 meter vertical resolution may be necessary for longwave and shortwave radiation to sufficiently heat and cool a cloud topped MBL.

While 50 m vertical resolution in mesoscale models now may be computationally practical on a real-time basis, 10 m resolution is presently too costly for most 3-D model applications. A third factor affecting predictions of sharp vertical MBL structures in some mesoscale models is the vertical diffusion. While necessary for numerical stability, application of a vertical diffusion that is too strong can weaken and smooth significant features, especially the sharp gradients which lead to EM ducting conditions. Finally, insufficient horizontal resolution may limit the ability to simulate important variability in the keys fields, including the propagation of gravity waves.

1.2 Atmospheric Refraction.

Since atmospheric refraction can have a significant impact on both the propagation path and the intensity of transmission from radar and microwave communications systems (Burk and Thompson 1997), it is important to understand the nature of atmospheric refractivity and what parameters govern the refractive index field. Electromagnetic (EM) waves derive their name from the combination of electric and magnetic force fields which combine to produce these waves. The phase velocity (c) of an EM wave is a function of the magnetic permeability (μ) and the dielectric permittivity (ϵ) of the propagating medium (Sauvageot 1992). In a vacuum, $\mu = \epsilon = 1$, and EM waves propagate with a phase velocity equal to the speed of light $c_0 = (3.000 \times 10^8 \text{ m s}^{-1})$. Furthermore, in a vacuum,

propagation occurs along a straight path, that is, with no bending of the ray. Since the relative magnetic permeability of air (μ_r) is nearly unity, the propagation path for radar energy is driven by the atmosphere's relative dielectric permittivity (ϵ_r) given by

$$\epsilon_r = \frac{\epsilon}{\epsilon_0} \quad (1.1)$$

where ϵ is the dielectric permittivity in air and ϵ_0 is the dielectric permittivity in a vacuum. Doviak and Zrnic' (1993) show that ϵ_r is a function of total air pressure (p), temperature (T), and water vapor pressure (e), meteorological quantities which vary both temporally and spatially. The refractive index of a medium (n), related to ϵ_r , is

$$n = \left(\frac{c}{c_0} \right) = \sqrt{\epsilon_r} \quad (1.2)$$

Since the refractive index (n) for air differs from unity in the 5th or 6th significant digit, it is routinely written as the radio refractivity (N) (Bean and Dutton 1966).

$$N = (n - 1) \times 10^6 \quad (1.3)$$

Bean and Dutton go on to show that N can be approximated within 10% using

$$N = \left(\frac{77.6}{T} \right) \left(p + 4810 \frac{e}{T} \right) \quad (1.4)$$

where P is the total atmospheric pressure in hPa, e is the partial pressure of water vapor in hPa, and T is the atmospheric temperature in K. The numerical constants were derived from empirical relationships and are valid in the range of radar and microwave frequencies (Babin 1995). Although horizontal variability in air pressure, temperature, and vapor pressure can impact the radio refractivity N , the dominant impact on refractivity results from changes in the vertical distribution of N and is especially sensitive to the vertical profile of water vapor (e).

The general phenomenon of atmospheric refraction can be divided into three types: normal refraction, subrefraction, or superrefraction. If a layer is subrefractive, radio waves propagating in or through the layer are bent away from the earth, resulting in less than favorable propagation characteristics. On the other hand, superrefractive layers deflect radio waves towards the earth's surface. In extreme cases of superrefractivity, the radio energy can propagate for much greater distances than in normal refractive cases and with little attenuation. These extreme cases are known as ducting. If the superrefractive conditions extend to the surface, then the duct is known as a surface duct, otherwise the duct is said to be elevated. Determination of layer refractive properties is based on the variability of radio refractivity with height (z). The variability of $N(z)$ with respect to height is simply the vertical derivative of equation (1.4), given by

$$\frac{dN}{dz} = \frac{77.6}{T} \frac{dp}{dz} - \frac{77.6p}{T^2} \frac{dT}{dz} - \frac{7.47 \times 10^5 e}{T^3} \frac{dT}{dz} + \frac{3.73 \times 10^5}{T^2} \frac{de}{dz} \quad (1.5)$$

The three types of refraction mentioned above occur for certain values of dN/dz (Babin 1995). These propagation regimes along with associated dN/dz values are summarized in Table 1.1.

Table 1.1
Layer Refractive Values and Properties

Case	dN/dz	Effects
Subrefractive	$> 0 \text{ km}^{-1}$	Radio Waves refracted away from the earth
Normal	$-76 \text{ to } 0 \text{ km}^{-1}$	Radio/microwave performance is poor
Superrefractive	$-156 \text{ to } -77 \text{ km}^{-1}$	Radio waves refracted toward the earth
Superrefractive Duct	$< -157 \text{ km}^{-1}$	Radio waves are trapped Propagation distance increases Attenuation is minimal

One can ascertain the positive and negative contributions of each term on the right hand side of equation (1.5) by simple examination. Since pressure decreases with height the first term is negative. Typically, the change of temperature with respect to height is negative resulting in positive contributions for terms 2 and 3. However, when the layer in question has a temperature inversion, $dT/dz > 0$, the second and third terms yield negative values. The fourth term is negative for standard atmospheric applications, as vapor pressure decreases for increasing height. In some temperature inversion layers where $de/dz > 0$, this term can take on positive values and counter the first three terms to some

degree. Of note, to produce subrefractive conditions ($dN/dz > 0$) in layers with temperature inversions ($dT/dz > 0$), the fourth term must be large and positive.

The previous discussion considered refraction of radio waves by the atmosphere without regard to curvature effects imposed by the earth's surface. In this context, some degree of superrefraction is useful as long as the bending of the rays does not exceed the curvature of the earth. Earth's curvature can be accounted for by shifting our focus to another representation, called the Modified Refractivity (M) (Burk and Thompson 1997).

$$M = N + 1.157z \quad (z \text{ in meters MSL}) \quad (1.6)$$

Whenever layers exist in the atmosphere where $dM/dz < 0$, radio and microwave energy can be trapped in a superrefractive duct (Burk & Thompson 1997). As such, trapping layers can be determined by simple inspection of vertical profiles of M. A typical M profile with potential trapping layers, observed at San Nicolas Island in the Southern California Bight during the Variability of Coastal Atmospheric Refractivity (VOCAR) experiment period, is shown in Figure 1.1. In addition, the figure shows a reference vertical profile of M, based on a Standard Atmosphere, with vapor pressure as a function of height,

$$e(z) = 10.2(1 - 0.0640z) \quad (1.7)$$

for the lowest 7.5 km (Sauvageot 1992). Relatively modest changes in the M profile within a duct can significantly alter the propagation of EM waves over distances of tens of kilometers.

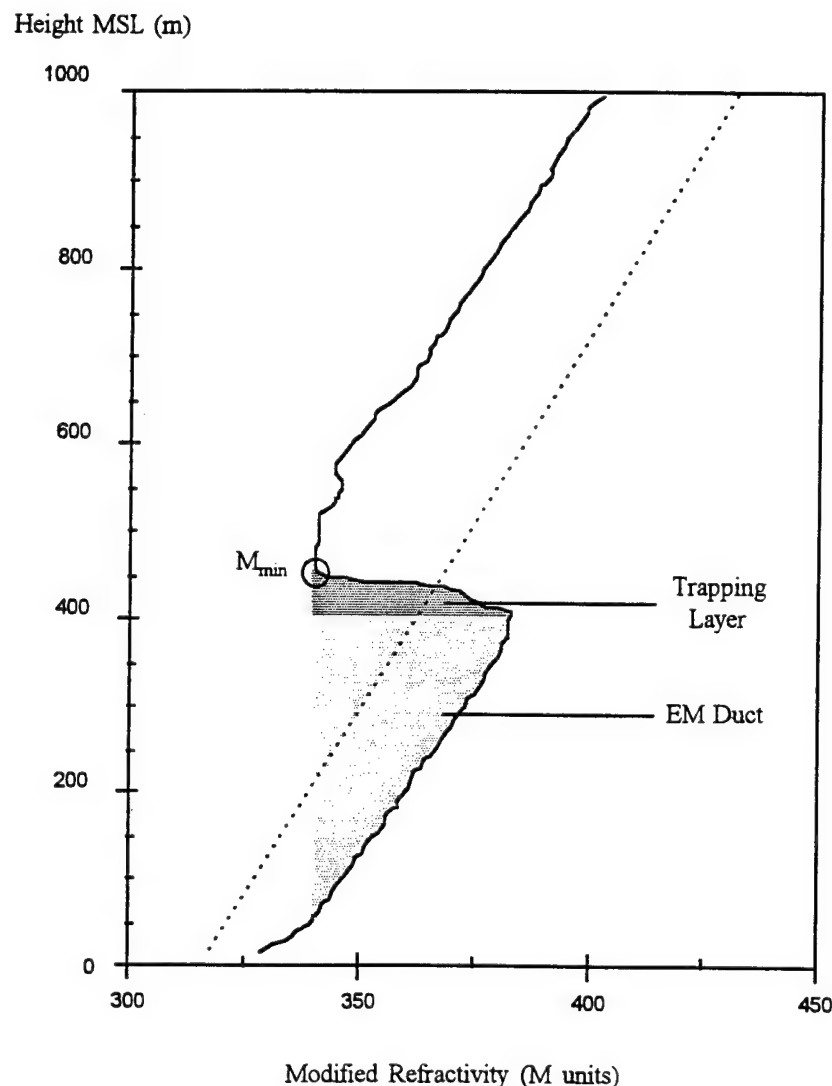


Figure 1.1. Modified Refractivity Profiles for a Standard Atmosphere (dashed) and for San Nicolas Island, 24 Aug 1993, 1200Z (solid). The trapping layer (dark stipple) occurs where $dM/dz < 0$. The duct (light stipple) extends from M_{\min} to the point on the M profile directly below M_{\min} .

1.3 The Marine Boundary Layer (MBL).

The layer of the atmosphere in closest proximity to the ocean surface is known as the MBL. Atmospheric properties and vertical structure of the MBL are governed by numerous physical processes including heat and moisture fluxes from the underlying ocean surface, cloud top radiational cooling at the top of the MBL, synoptic scale subsidence of the free atmosphere overlying the MBL, coastal and mesoscale circulations, and sea surface temperature gradients. Due in large part to the influence of the sea surface, air in the MBL can be markedly different than the free atmosphere above. As a result, large gradients in temperature and moisture typically exist in the interfacial layer (Fig. 1.2)

This research focuses on the impact of the summertime MBL on EM propagation in the Southern California Bight (Fig. 1.3). To fully understand this effect on M profiles, one should consider typical conditions in this region. Thorough investigations of East Pacific climatology has confirmed the sloping nature of the MBL (Bridger et al. 1993, Brost et al. 1982, Neiburger et al. 1961). In particular, the thermal inversion base steadily rises with distance offshore (Figs. 1.4 and 1.5). The shallower marine layer along the coast results from the relatively strong low level winds paralleling the California coast which produce cold water upwelling. (Beardsly et al. 1987, Elliot and O'Brien 1977). The quasi-steady state temperature inversion is typically on the order of 5-20°C over a 200-500 m layer (Neiburger et al. 1961) throughout the summer period. In fact, soundings show evidence of thermal inversions for most of the summer period (Fig. 1.6). The synoptic scale structure of this layer is primarily driven by subsidence aloft from the East

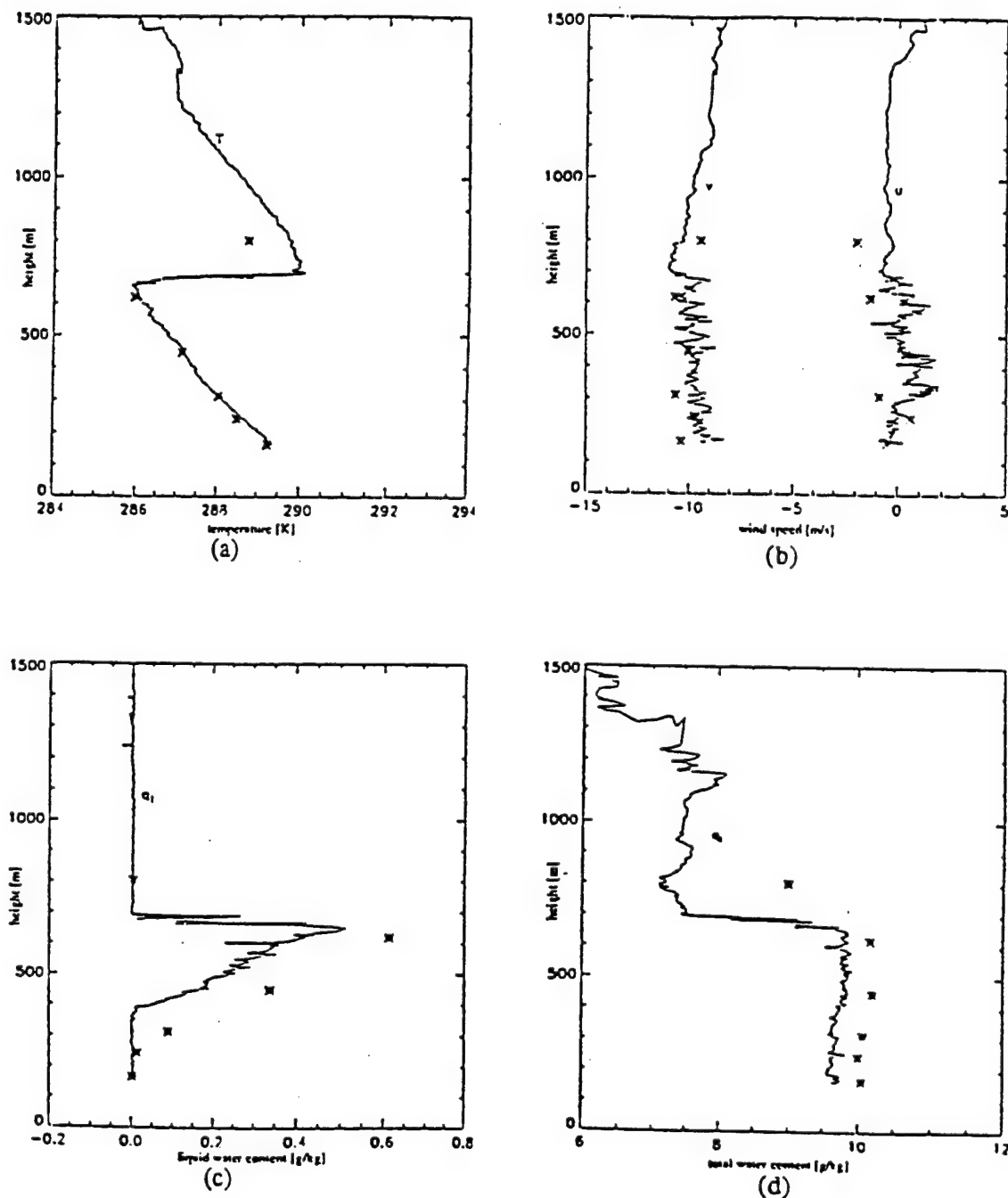


Figure 1.2 Observed soundings measured by aircraft as part of ASTEX on 0000 UTC 13 June 1992 northeast of Santa Maria Island in the Azores: (a) temperature (K), (b) wind speed (m s^{-1}), (c) liquid water content (g kg^{-1}) and (d) total water content (g kg^{-1}). Data points are horizontally averaged values of aircraft data measured as part of the same study. (Duynkerke et al. 1995)

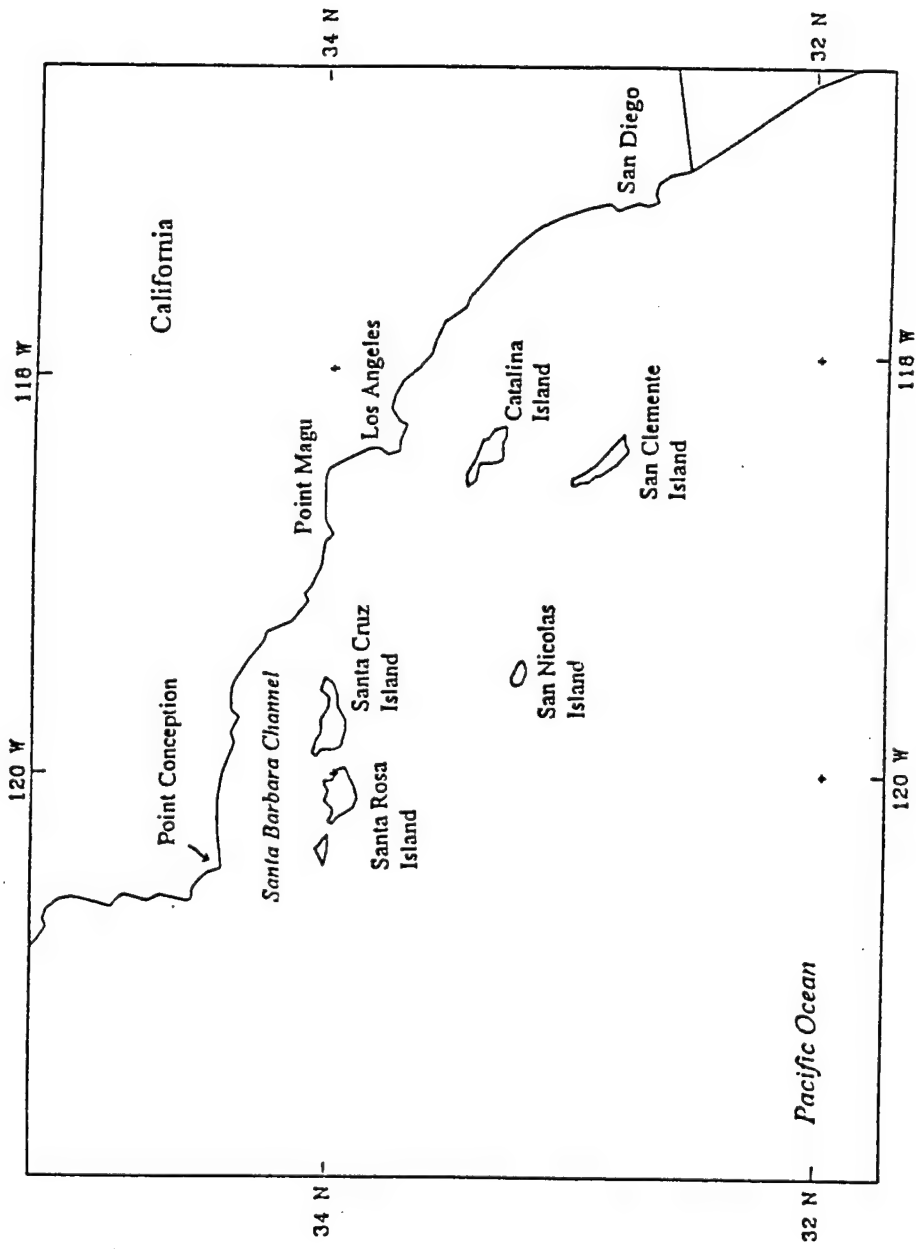


Figure 1.3. Area called the Southern California Bight, location of the Variability of Coastal Atmospheric Refractivity (VOCAR) experiment. (Aug/Sep 1993)

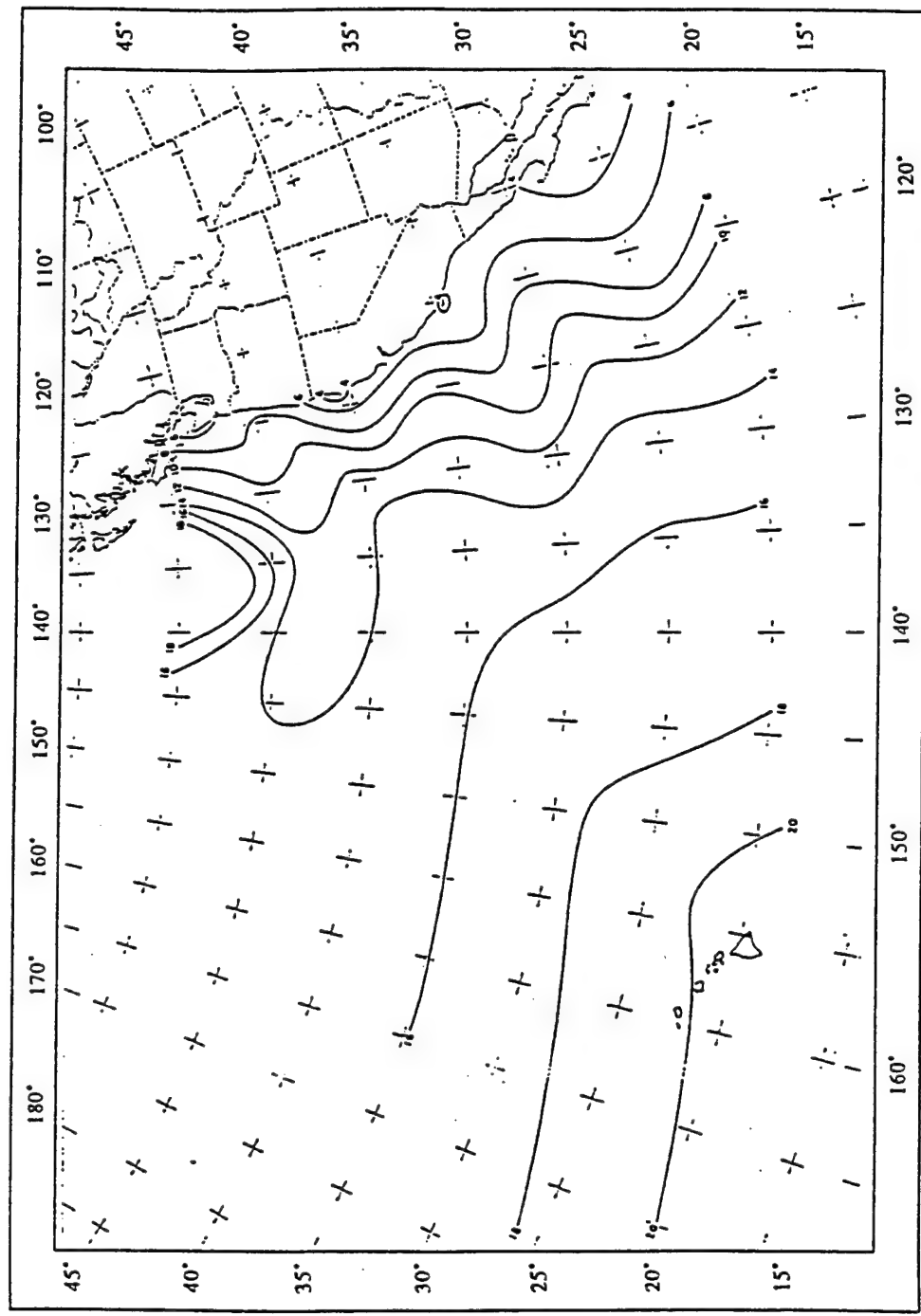


Figure 1.4 Observed climatological height of inversion base in summer over the northeast Pacific from Neiburger et al. (1961) (hundreds of meters). Contour interval is 200 m.

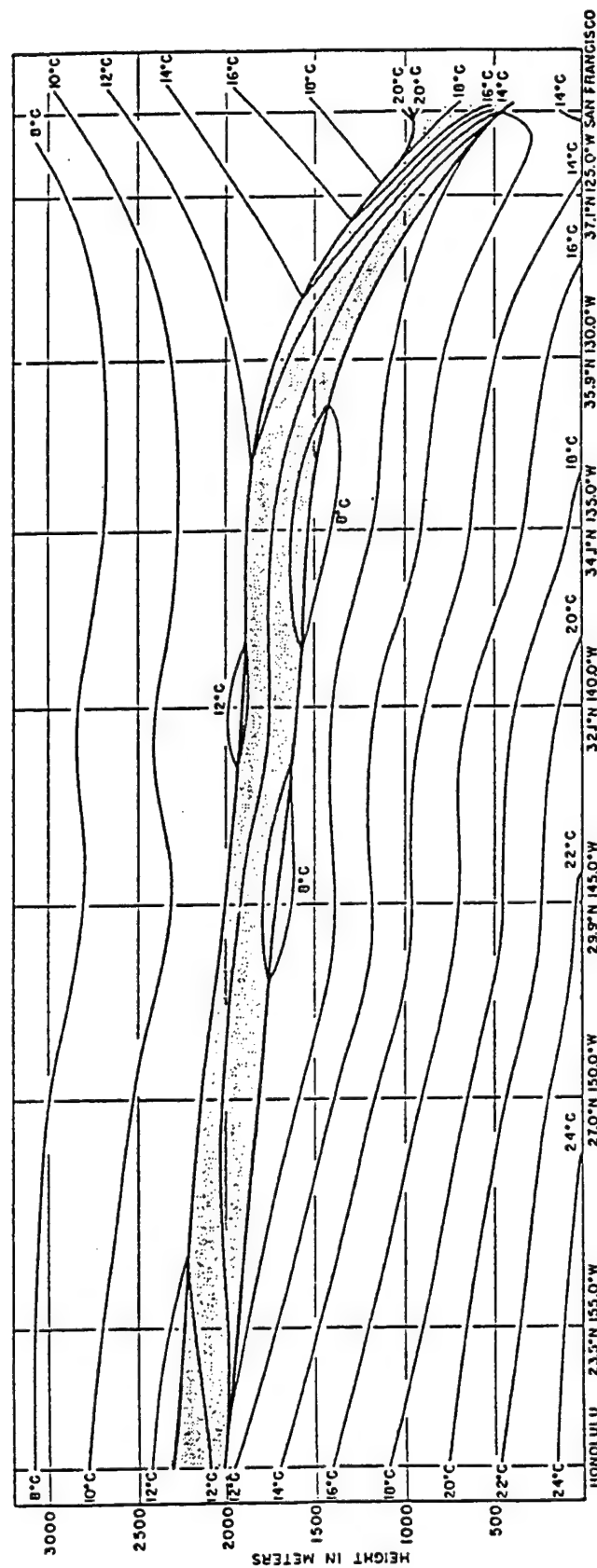


Figure 1.5 Observed average summer cross section of temperature (°C) from San Francisco to Honolulu.
 Subtropical inversion layer is shown by stippled shading and contour interval is 2°C.
 (Neiburger et al. 1961)

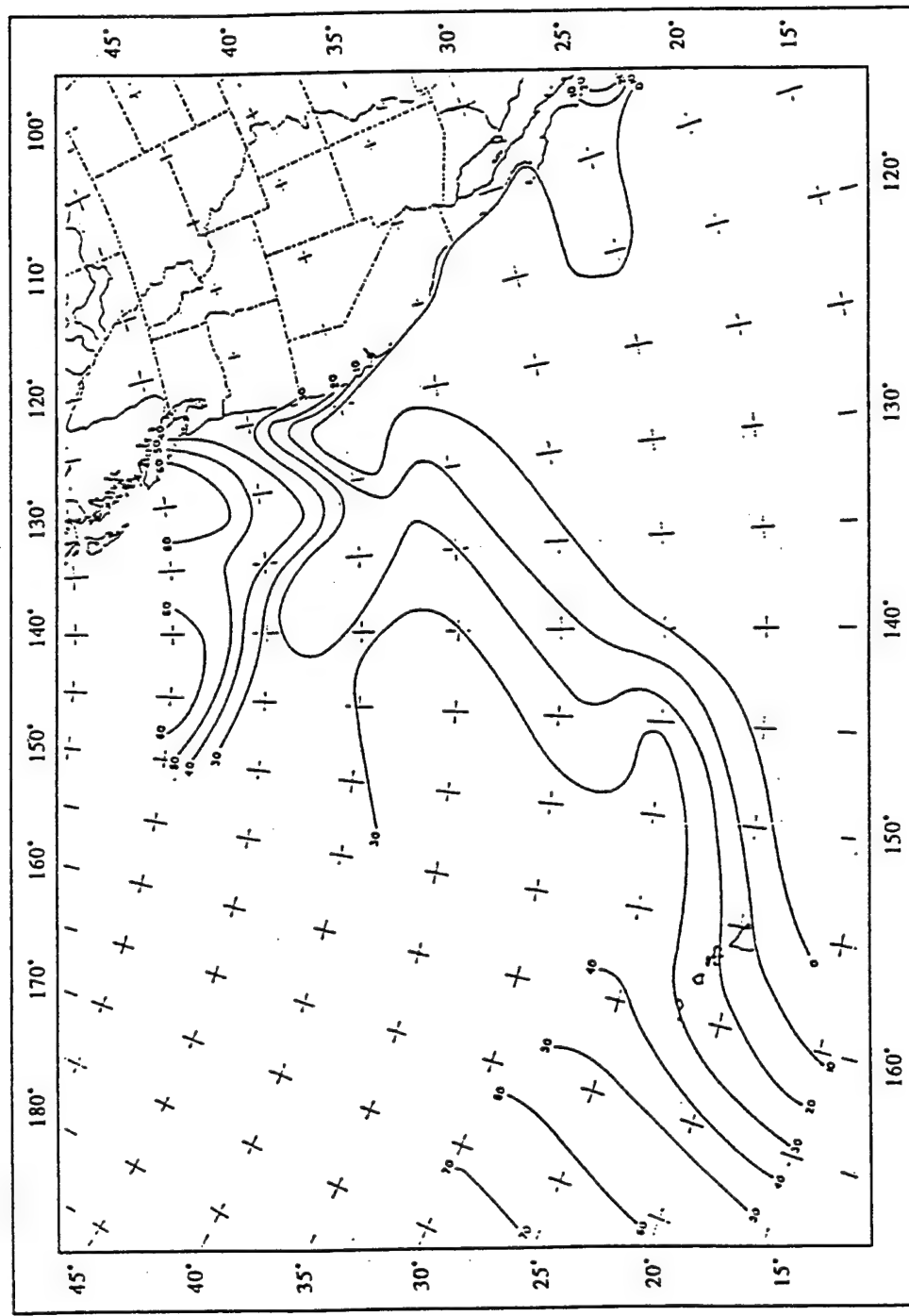


Figure 1.6 Percentage of observations with no inversions during the months June-September. (Neiburger et al. 1961)

Pacific ridge and cooler sea surface temperatures in the coastal zone. Smaller scale variations in the overall structure of the MBL can be driven by mesoscale circulations. For example, the diurnal nature of the sea breeze can suppress MBL depth during the afternoon along the coast due to mass continuity and enhanced subsidence caused by the return flow aloft.

1.4. Thesis Objectives.

Numerical codes used to calculate EM propagation paths, based on the 3-D Modified Refractivity field, are straightforward and routinely employed to reveal layers in which ducting may occur. Atmospheric pressure, temperature, and vapor pressure are required input parameters for these EM propagation codes. Routinely, operators of radar and microwave systems employ rawinsonde data obtained along or near the propagation path to ascertain the M profile. This observed data has neither the temporal nor spatial resolution to adequately portray the true nature of the varying M field (Richter 1994). Advanced mesoscale atmospheric numerical models, however, represent a potentially important source of information to assist in determining the refractivity structure. Therefore, this research will:

- Employ an advanced mesoscale numerical weather prediction system to accurately diagnose the 3-D Modified Refractivity field in the California Bight,

- Investigate the ability of a mesoscale numerical weather prediction system to supply high resolution meteorological quantities to reasonably forecast the 3-D Modified Refractivity field up to a week in advance,
- Focus on a two day period to uncover possible diurnal and transient wave effects on MBL structure, and in turn the M field,
- Examine the longer term temporal variation in MBL depth to ascertain the role of synoptic scale factors, such as subsidence, transient short waves, and cyclone development.

Chapter 2 describes the mesoscale numerical weather prediction system used for this research. Chapter 3 discusses the design and goals of the numerical simulations. A case description of the meteorology associated with the VOCAR study period is presented in Chapter 4. Experimental results are presented in Chapter 5 and conclusions are summarized in Chapter 6.

Chapter 2

MODEL DESCRIPTION

2.1 The PSU/NCAR Mesoscale Model Version 5.1

All simulations for this study were conducted using The Pennsylvania State University/National Center for Atmospheric Research (PSU/NCAR) Mesoscale Model version 5.1 (MM5v1) (Dudhia 1993, Grell et al. 1994). The MM5v1 modeling system is derived from the Navier Stokes equations in a rotating reference frame (2.1), the fully compressible continuity equation (2.2), the ideal gas law (2.3), and the first law of thermodynamics (2.4). The full set of equations are shown below in tensor form; note that all symbols adhere to standard meteorological convention.

$$\frac{\partial u_i}{\partial t} + u_j \frac{\partial u_i}{\partial x_j} = -\frac{1}{\rho} \frac{\partial p}{\partial x_i} - \delta_{i3} g - 2\epsilon_{imn} \Omega_m u_n + \frac{\mu}{\rho} \frac{\partial^2 u_i}{\partial x_k^2} \quad (2.1)$$

$$\frac{\partial \rho}{\partial t} + u_j \frac{\partial \rho}{\partial x_j} = -\rho \frac{\partial u_j}{\partial x_j} \quad (2.2)$$

$$p = \rho RT \quad (2.3)$$

$$\frac{\partial T}{\partial t} + u_j \frac{\partial T}{\partial x_j} = \frac{1}{\rho c_p} \frac{Dp}{Dt} + \frac{\dot{Q}}{c_p} \quad (2.4)$$

The nonhydrostatic form of MM5v1 partitions the state variables (p, T, and ρ) into constant base state fields and perturbation fields. The base state fields are only a function

of height (z) while the perturbation fields are allowed to vary both temporally and spatially. The full state variables and their partitioning are:

$$p(x, y, z, t) = p_0(z) + p'(x, y, z, t) \quad (2.5)$$

$$T(x, y, z, t) = T_0(z) + T'(x, y, z, t) \quad (2.6)$$

$$\rho(x, y, z, t) = \rho_0(z) + \rho'(x, y, z, t) \quad (2.7)$$

while the base state for the wind is zero. The model employs the terrain following non-dimensional pressure-sigma (σ_p) vertical coordinate system, where

$$\sigma = \frac{p_0 - p_t}{p_s - p_t} = \frac{p_0 - p_t}{p^*} \quad (2.8)$$

and p_t is the base state pressure at the top of the model, p_s is the surface base state pressure, and p_0 is the base state pressure on the model sigma surfaces. The model equations, not depicted here, are written in "flux-form" to be mass conservative (Grell et al. 1994). A summary of the prognostic fields, model variables, and units is provided in Table 2.1.

2.2 Computational Domains.

Since both the large scale dynamics associated with the East Pacific Ridge and coastal zone mesoscale circulations may affect inversion height and strength, three computational domains were defined in Lambert-Conformal space for this study (Fig. 2.1). The specifics of these computational grids are summarized in Table 2.2. The lateral extent

Table 2.1
MM5v1 Prognostic Field Summary

Field	Variable	Units
Zonal Wind	p^*u	$cb \text{ m s}^{-1}$
Meridional Wind	p^*v	$cb \text{ m s}^{-1}$
Vertical Motion	p^*w	$cb \text{ m s}^{-1}$
Pressure Perturbation	p^*p'	$cb \text{ Pa}$
Temperature	p^*T	$cb \text{ K}$
Water Vapor Mixing Ratio	p^*q_v	$cb \text{ Kg Kg}^{-1}$
Grid Scale Cloud Water	p^*q_c	$cb \text{ Kg Kg}^{-1}$
Grid Scale Rain Water	p^*q_r	$cb \text{ Kg Kg}^{-1}$

Table 2.2
VOCAR Computational Grid Summary

N/S x E/W Grid Size (km)	N/S x E/W Grid Points	Grid Cell Resolution (km)	Terrain Resolution Data Base (min/km)	Land-Use Resolution Data Base (min/km)
5184 x 6480	49 x 61	108	5/9	10/19
2592 x 1944	73 x 55	36	5/9	10/19
936 x 864	79 x 73	12	.5/.9	10/19

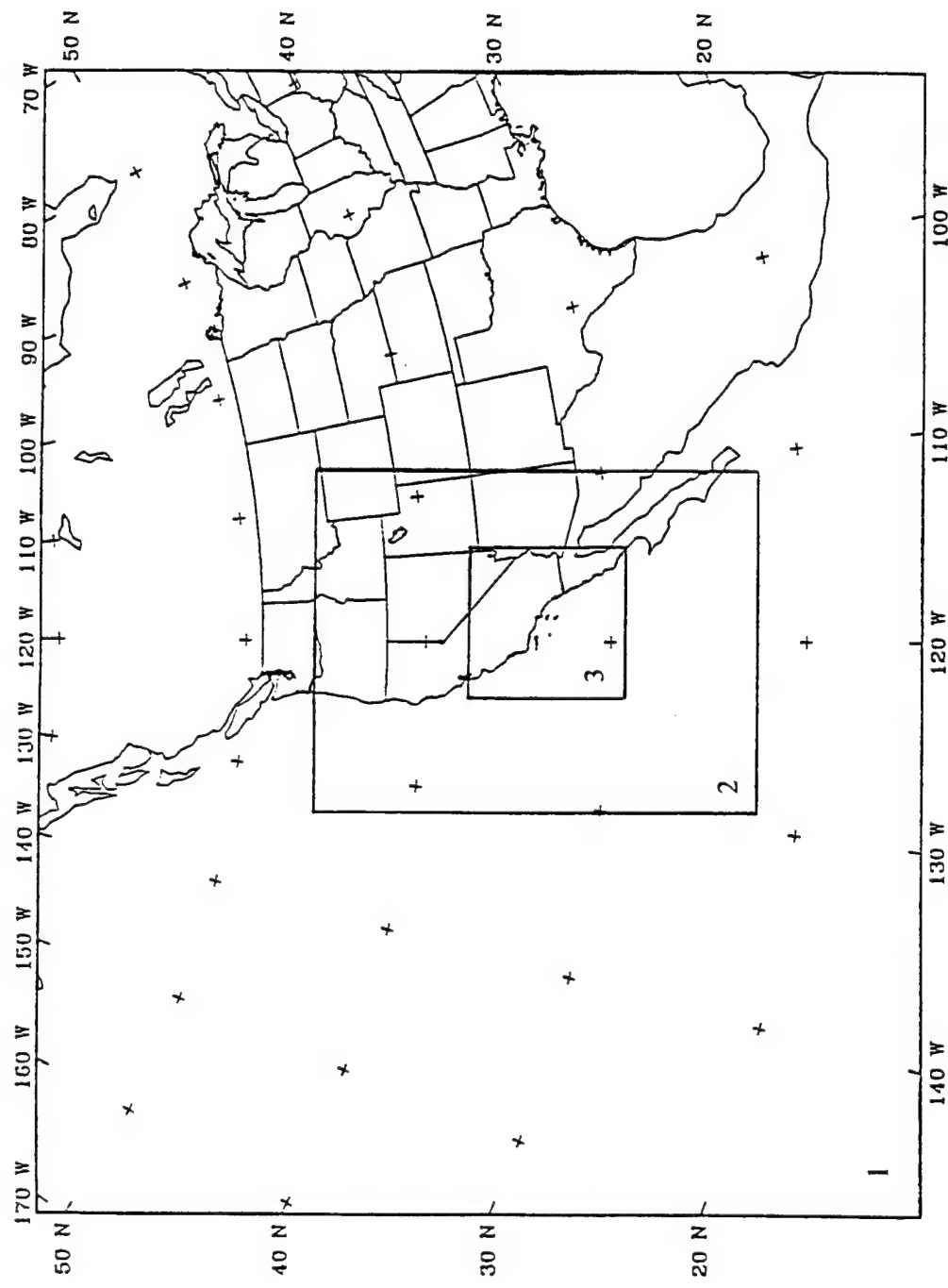


Figure 2.1 Model grids for this study on a Lambert conformal projection. Coarse Grid Mesh (CGM) standard latitudes are 30 N and 60 N and central longitude is 120 W.

of the Coarse Grid Mesh (CGM) is designed to resolve the longwave pattern, transient shortwaves, and large scale subsidence effects from the semi-permanent East Pacific Ridge. The domain specifications also allow for the CGM boundary conditions to be well removed from the VOCAR region.

Fifty-three computational sigma layers, with twenty-one layers in the lowest kilometer, comprise the vertical model structure for this research. The distribution of these model layers is listed in Table 2.3 for a grid cell at Mean Sea Level (MSL), along with their base state pressures, temperatures, and heights. The sigma levels were computed from the non-hydrostatic base state pressure field using equation (2.8) with $p_t = 100$ mb and $p_s = 1000$ mb. The sigma coordinates were specified to provide 40 m vertical resolution in the lowest 600 m. Such fine resolution is necessary to maintain the sharp thermal and moisture gradients associated with the marine inversion.

2.3 Model Physics.

Precipitation processes for this implementation of MM5v1 are calculated explicitly, that is, on the resolved scale. Hence, when a grid volume reaches saturation, the explicit precipitation scheme is activated (Dudhia 1989), which calculates water vapor mixing ratio (q_v), cloud water (q_l), and rainwater (q_r). This method also allows for cloud ice and snow. Of critical importance in the MBL is the accurate representation of q_v and q_l . As discussed earlier, sharp vertical moisture gradients are the primary cause of atmospheric EM ducting. Furthermore, MBL cloud top cooling helps to drive the turbulent processes within the MBL. This fact is especially significant in the California littoral where cold

Table 2.3
Vertical Distribution of Computational Layers

Layer	Sigma Value	Pressure (mb)	Temperature (K)	Height (m)
1	.0144	113.0	181.0	15,038
2	.0433	139.0	191.3	13,908
3	.0723	165.1	199.9	12,924
4	.1012	191.1	207.3	12,050
5	.1302	217.2	213.6	11,262
6	.1591	243.2	219.3	10,544
7	.1881	269.3	224.4	9,883
8	.2170	295.3	229.0	9,270
9	.2460	321.4	233.2	8,697
10	.2749	347.4	237.1	8,160
11	.3039	373.5	240.8	7,654
12	.3328	399.5	244.1	7,175
13	.3618	426.6	247.3	6,721
14	.3907	451.7	250.3	6,288
15	.4198	477.7	253.1	5,875
16	.4486	503.8	255.7	5,479
17	.4776	529.8	258.2	5,099
18	.5065	555.9	260.6	4,738
19	.5355	581.9	262.9	4,384
20	.5644	608.8	265.1	4,045
21	.5934	634.0	267.2	3,718
22	.6223	660.1	269.2	3,401
23	.6513	686.2	271.2	3,095
24	.6802	712.2	273.0	2,798
25	.7092	738.3	274.8	2,510
26	.7381	764.3	276.6	2,230
27	.7671	789.1	278.2	1,971
28	.7961	811.4	289.6	1,743
29	.8124	831.2	280.8	1,546
30	.8318	848.6	281.8	1,374
31	.8487	863.9	282.7	1,227
32	.8634	877.1	283.4	1,102
33	.8760	888.4	284.1	994
34	.8869	898.2	284.7	903
35	.8962	906.6	285.1	826
36	.9046	914.1	285.5	757
37	.9121	920.9	285.9	695
38	.9190	927.1	286.2	639
39	.9252	932.7	286.5	588
40	.9309	937.8	286.8	542
41	.9360	942.4	287.0	501
42	.9410	946.9	287.2	461
43	.9460	951.4	287.5	421
44	.9510	955.9	287.8	381
45	.9561	960.5	288.0	341
46	.9612	965.1	288.2	301
47	.9663	969.7	288.5	261
48	.9715	974.3	288.7	221
49	.9766	979.0	288.9	180
50	.9818	983.6	289.2	140
51	.9870	988.3	289.4	100
52	.9922	993.0	289.7	60
53	.9974	997.7	289.9	20

water upwelling results in little to no positive heat flux from the ocean surface (Leidner 1995). During the summer months over cool ocean waters, however, precipitation is not expected to be important within the circulation of the East Pacific Ridge.

The atmospheric radiation submodel of MM5v1 accounts for both infrared and visible radiative interactions with water vapor, cloud water, rain water, and the earth's surface (Dudhia 1989). This scheme treats longwave absorption by water vapor using the common broadband emissivity method (Stephens 1984). This approach calculates emissivity functions, layer by layer, for incoming and outgoing longwave radiation using empirically derived emissivities as a function of water vapor path (Rodgers 1967). Cloud water and rain water radiative properties are also incorporated into the layer total emissivity defined as:

$$\varepsilon_{\text{tot}} = 1 - T_v T_c T_p \quad (2.9)$$

where the transmissivity functions are given by

$$T_v = 1 = \varepsilon_{\text{vapor}} \quad T_c = \exp(-\alpha_c u_c) \quad T_p = \exp(-\alpha_p u_p) \quad (2.10)$$

In this representation, u_c is the cloud water path, u_p is the rain water path, α_c is the cloud water absorption coefficient, and α_p is the rain water absorption coefficient. The total emissivity function determines the longwave radiative flux at each full sigma level. Once these fluxes are computed, the radiative scheme calculates the longwave heating rate based on the flux divergence in the model half-layers. The downward flux of shortwave

(visible) radiation is a function of solar zenith angle, clear air scattering, water vapor absorption, cloud albedo, and cloud absorption. Values for cloud albedo and absorption depend on both the solar zenith angle and the vertically integrated water path. These values are obtained through bilinear interpolation from a lookup table based on theoretical results (Stephens 1978). Clear air scattering of shortwave radiation is considered uniform and is proportional to the atmosphere's mass path length. Water vapor absorption is based on a method described by Lacis and Hansen (1974). The shortwave heating rate is then calculated as a function of cloud and water vapor absorption. The longwave and shortwave radiative fluxes at the earth's surface are then passed to the Planetary Boundary Layer (PBL) submodel for use in the surface energy balance equation.

A revised version of Blackadar's High-Resolution Planetary Boundary Layer (HIRPBL) (Blackadar 1976, 1979, Zhang and Anthes 1982) code is used to parameterize turbulent boundary layer processes. Based on Blackadar's "force-restore" method, the surface energy budget incorporates the net radiative flux, sensible heat flux, substrate heat flux, and surface moisture flux to predict ground temperature over land. Albedo, moisture availability, emissivity, roughness length, and thermal inertia are specified for up to thirteen land-use categories for inclusion in the surface energy budget calculation of ground temperature. However, the ground (slab) temperature is held constant over water throughout the simulation.

Surface heat and moisture fluxes are calculated via Monin-Obukhov similarity theory. Away from the surface layer, vertical mixing of horizontal momentum, potential temperature, water vapor mixing ratio, cloud water and ice is determined by one of two

PBL regimes. The “nocturnal regime” accounts for cases where the atmosphere is stable, mechanically turbulent, or convectively forced (near neutral). This regime is generally stable or marginally unstable at most. First order K-theory provides closure for model variables in the nocturnal regime. The second PBL regime is free convection, where vertical mixing is based upon the thermal structure of the entire mixed layer. This regime accounts for unstable conditions due to strong surface heating. In the free convective regime, the surface layer interacts, or mixes, with each layer in the PBL at every time step (non-local closure). Above the mixed layer, however, vertical diffusion of the prognostic variables is based on K-theory, where K_z , the eddy diffusivity, is a function of the local Richardson number. Sensitivity tests conducted in a similar MBL study indicate the model’s default background vertical diffusion ($1.0 \text{ m}^2\text{s}^{-1}$) is too high to preserve the strength of temperature and moisture gradients in inversion layers (Leidner 1995). Therefore, this research will use a more realistic background constant vertical diffusion suggested by Leidner, $K_z = 0.01 \text{ m}^2\text{s}^{-1}$.

Chapter 3

EXPERIMENTAL DESIGN

The numerical simulations cover a one week period from August 24 to August 31, 1993. Boundary and initial conditions for the coarse outer grid were derived from the National Weather Service (NWS) global analyses. The two outer grids (108 and 36 km) were run simultaneously allowing for two-way interactive boundary conditions at each time step. The 12 km grid used boundary and initial conditions interpolated from the 36 km output with boundary conditions updated hourly throughout the 168 hour run. These three grids include a 12 hour pre-forecast period (described below) starting at 24/1200z. Specific modifications implemented for this set of MM5v1 model runs include a dynamic initialization strategy, reduced shortwave heating (in cloud), reduced moisture availability in the Los Angeles Basin, and a lower constant value of background vertical diffusion.

3.1 Dynamic Initialization.

As mentioned in earlier discussions, EM propagation is highly sensitive to the MBL structure, especially the vertical structure of moisture and temperature in the relatively thin interfacial region. As such, accurate simulation of the MBL in a mesoscale numerical weather model is equally vital. Also, synoptic scale features, like large scale subsidence from the East Pacific Ridge, are believed to play a dominant role in determining the MBL depth and inversion strength; hence accurate representation of larger scale conditions is required as well. Earlier numerical weather prediction models usually relied on static initialization at the onset of integration, resulting in a period of model “spin-up”. During

this period, the numerical model gradually attained a balance in the dynamic model fields through the geostrophic adjustment process. Moreover, representative grid scale features such as cloud, did not develop until six to twelve hours into the forecast (Leidner 1995).

Advances over the past decade have resulted in various methods of dynamic model initialization, including intermittent and continuous FDDA (nudging, FDDA, 3D-Variational, and 4D Variational analysis). These methods include a pre-forecast period during which model initial conditions are improved through the ingest of additional observations, previous model forecasts (first guess method), current gridded analyses, or climatology. All of these dynamic initialization schemes are designed to minimize error in the initial conditions. In this study, the MM5v1 incorporates two methods of FDDA: Multiscale FDDA and a Marine Boundary Layer Initialization (MBLI) scheme.

3.1.1 Multiscale Four-Dimensional Data Assimilation.

Multiscale FDDA, described in detail by Stauffer and Seaman (1994), can incorporate both observed data and gridded analyses into the model solution through Newtonian relaxation. Fundamentally, both approaches nudge the model primitive equations by attaching an artificial tendency term proportional to the difference between the model state and the data. The observation nudging approach relies on observed data obtained at non-uniform spatial and temporal scales. Although higher than normal spatial and temporal resolution observations exist for the VOCAR period, they were not used for the present set of experiments; these data will be used to evaluate the model results.

For this research, gridded National Weather Service (NWS) global analyses at 12 hour intervals were interpolated to the model's 108 km and 36 km grids and used to nudge the 3-D wind, temperature, and moisture fields. In an analysis nudging scheme, the tendency for any prognostic model variable, α , is a linear combination of the model forcing and the imposed nudging term. A flux form predictive equation would take the form of:

$$\frac{\partial p^* \alpha}{\partial t} = F(\alpha, \bar{x}, t) + G_\alpha W(\bar{x}, t) \varepsilon(\chi) p^*(\alpha_0 - \alpha) \quad (3.1)$$

where F is the model's physical forcing, G is the relative magnitude of the nudging term to other forcing terms, W is the spatial and temporal weighting function, ε is an analysis quality factor, and $(\alpha_0 - \alpha)$ is the difference between the target analysis and the current model solution.

The goal of analysis nudging in this study is to ensure accurate representation in the amplitude and phase of synoptic scale features throughout the free simulation period. (Note: The free simulation is the 156 hour period after a 12-hour dynamic initialization). Analysis nudging based upon the gridded analysis fields was not performed on sigma levels with $\sigma \geq .850$, roughly 1225 meters MSL (the lowest 22 model layers). In this manner, the model's MBL structure is developed without direct interference from the FDDA, which acts only to minimize errors in the overlying troposphere and stratosphere. Furthermore, since the nudging is applied only to the 108 and 36 km domains, the effect of the FDDA is limited to improving the quality of the lateral boundary conditions for the 12

km domain. It is the model solution on this inner domain that is the primary focus of this study.

3.1.2 Marine Boundary Layer Initialization.

The Marine Boundary Layer Initialization (MBLI) scheme is an integral portion of the model's dynamic initialization in this study. Typically, mesoscale model initialization over ocean areas is difficult due in large part to the scarcity of data. Although gridded forecast fields can be used, often, the global models which produce these forecasts cannot resolve mesoscale circulations and marine boundary layer structures. Hence, the early period of a mesoscale weather prediction model is hampered due to poorly represented initial conditions. Leidner (1995) developed and tested a dynamic initialization of the MBL to counter these problems that effectively used a combination of climatological and current data during a 12 hour pre-forecast period to generate a realistic initial MBL structure. Using the MBLI, Leidner found significant improvement in PBL depth and inversion strength (in the initial conditions and the ensuing forecast period) compared to conditions developed from a traditional static initialization.

Owing to the critical impact of MBL structure on EM propagation ducts, this current research adopted the Leidner scheme in a 12 hour pre-forecast dynamic initialization for all domains except the 4 km mesh. In this method, Neiburger's (1961) climatology (Fig. 1.4 and 1.6) is used as a target toward which model temperature and moisture profiles are continuously nudged during the MBLI period. A comparison of the offshore potential temperature and mixing ratio structure, with and without the MBLI

scheme, is shown in Figs. 3.1. and 3.2, for 25 August 1993. Clearly, the model initial conditions contain much stronger vertical gradients at the top of the MBL when this method of dynamic initialization is used, in good agreement with the climatology and soundings obtained during the VOCAR period (Fig. 3.3).

3.2 Model Physics.

Three specific modifications affecting the model's physics were implemented for this set of experiments. First, Leidner (1995) found that the normal calculated absorption of shortwave radiation by marine stratus, using the Dudhia (1989) scheme, causes heating values that exceeded longwave cooling and led to complete dissipation of the cloud deck during the daytime. Many researchers have shown that the shortwave heating rate in low-level clouds is only a fraction, ranging from one-sixth to one-third, of the absolute longwave cooling (Oliver et al. 1978; Stephens 1978; and Duynkerke and Hignett 1993). The erroneously small longwave cooling by Dudhia's (1989) scheme is attributed to its inability to respond to variations in the droplet distributions for different types of clouds, in this case shallow marine stratus clouds. When Leidner (1995) conducted sensitivity tests limiting the shortwave heating rate within clouds to one-third the longwave cooling, he found that MBL clouds in MM5 behaved realistically and only dissipated partially during daytime hours. Therefore, absorption of shortwave radiation by clouds in the MBL was limited in this study to no more than one-third of the calculated model longwave tendency.

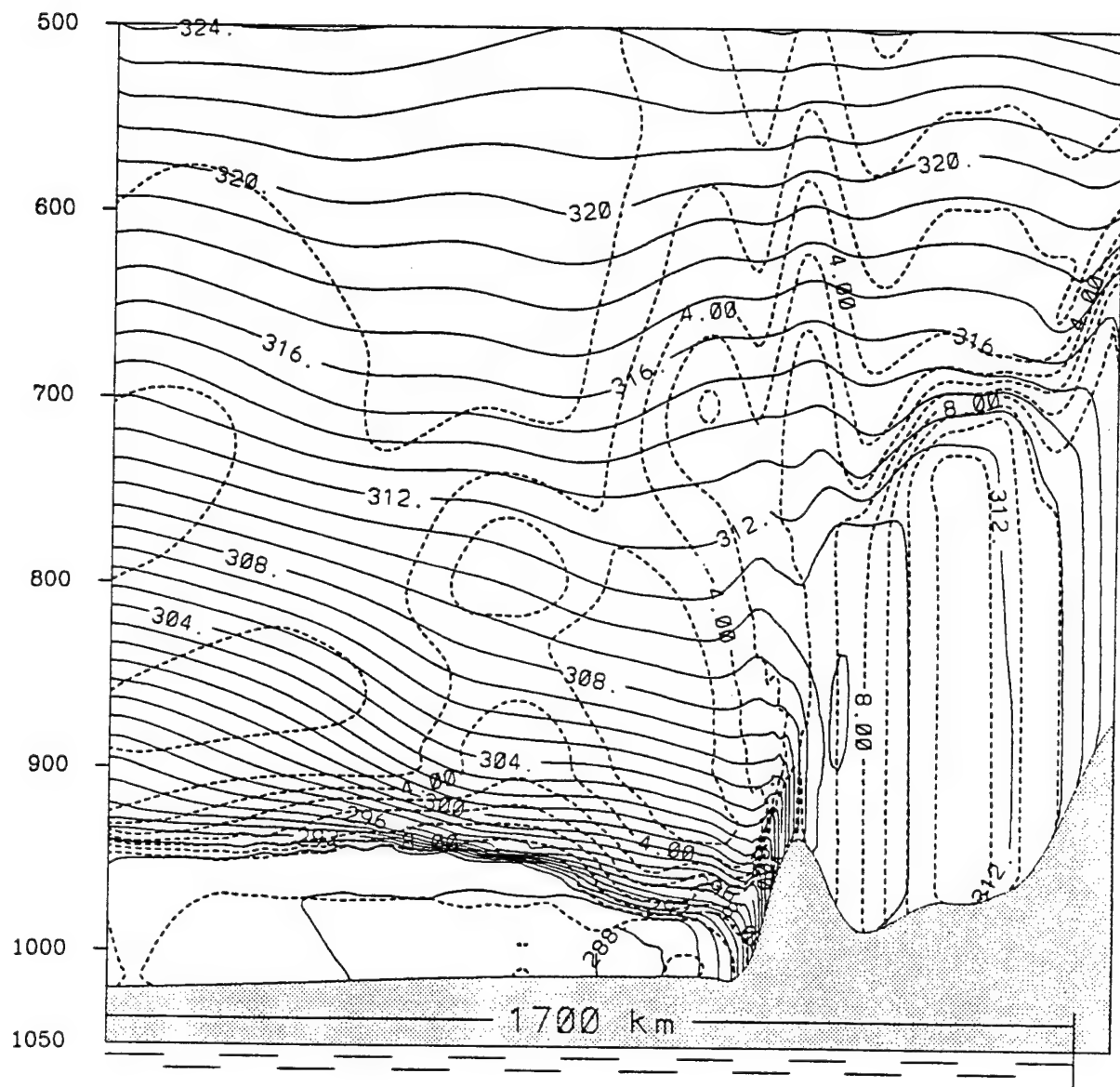


Figure 3.1. Simulated west-east cross section through San Nicolas Island depicting the MBL structure at the end of a pre-forecast period without the MBL initialization scheme (Valid: 25 August 1993, 0000 Z). Potential temperature is solid, 1 K contours, and water vapor mixing ratio is dashed, 1 g kg⁻¹ contours.

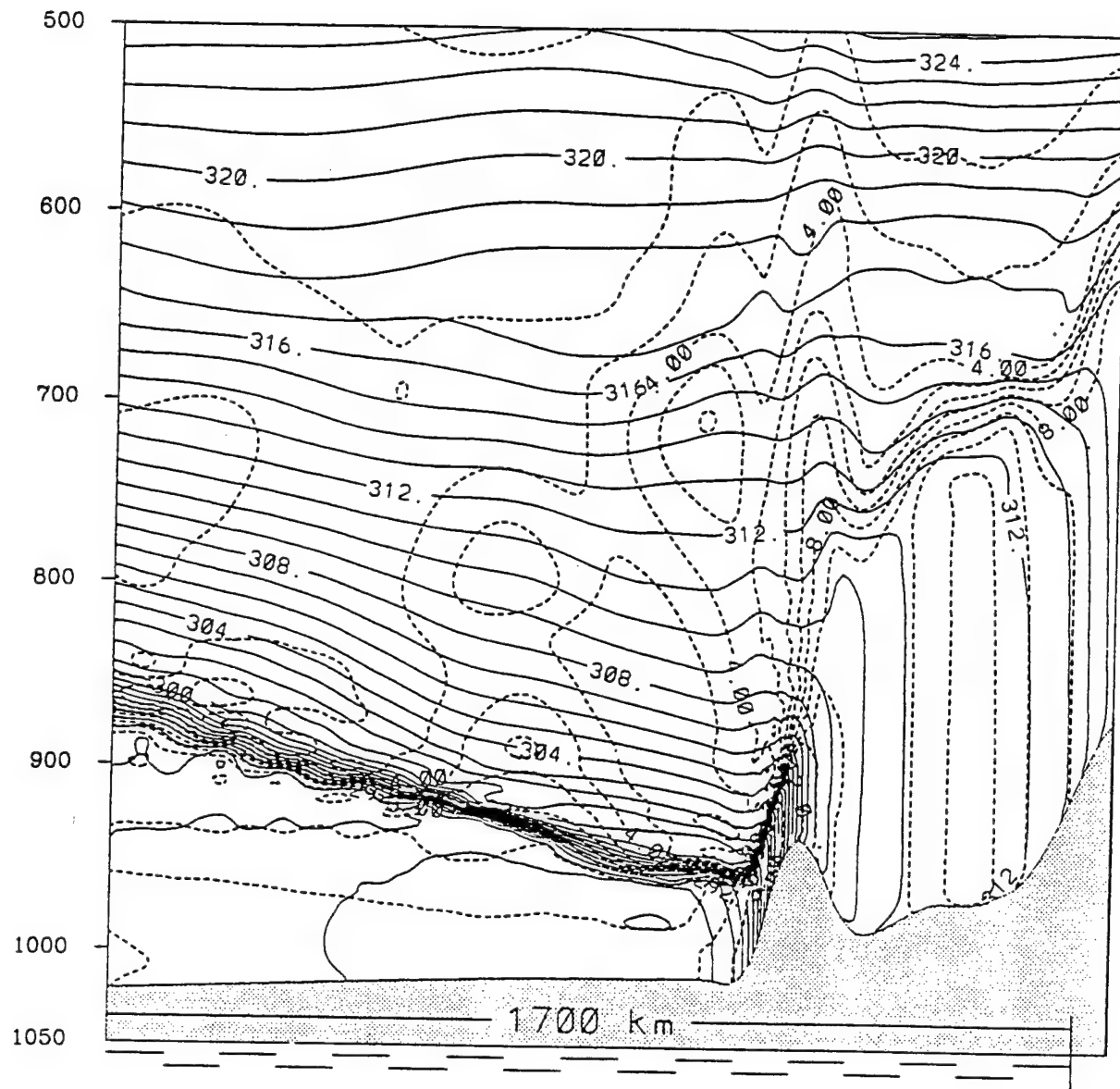


Figure 3.2. Simulated west-east cross section through San Nicolas Island depicting the MBL structure at the end of a pre-forecast period with Leidner's MBL initialization scheme (Valid: 25 August 1993, 0000 Z). Potential temperature is solid, 1 K contours, and water vapor mixing ratio is dashed, 1 g kg⁻¹ contours.

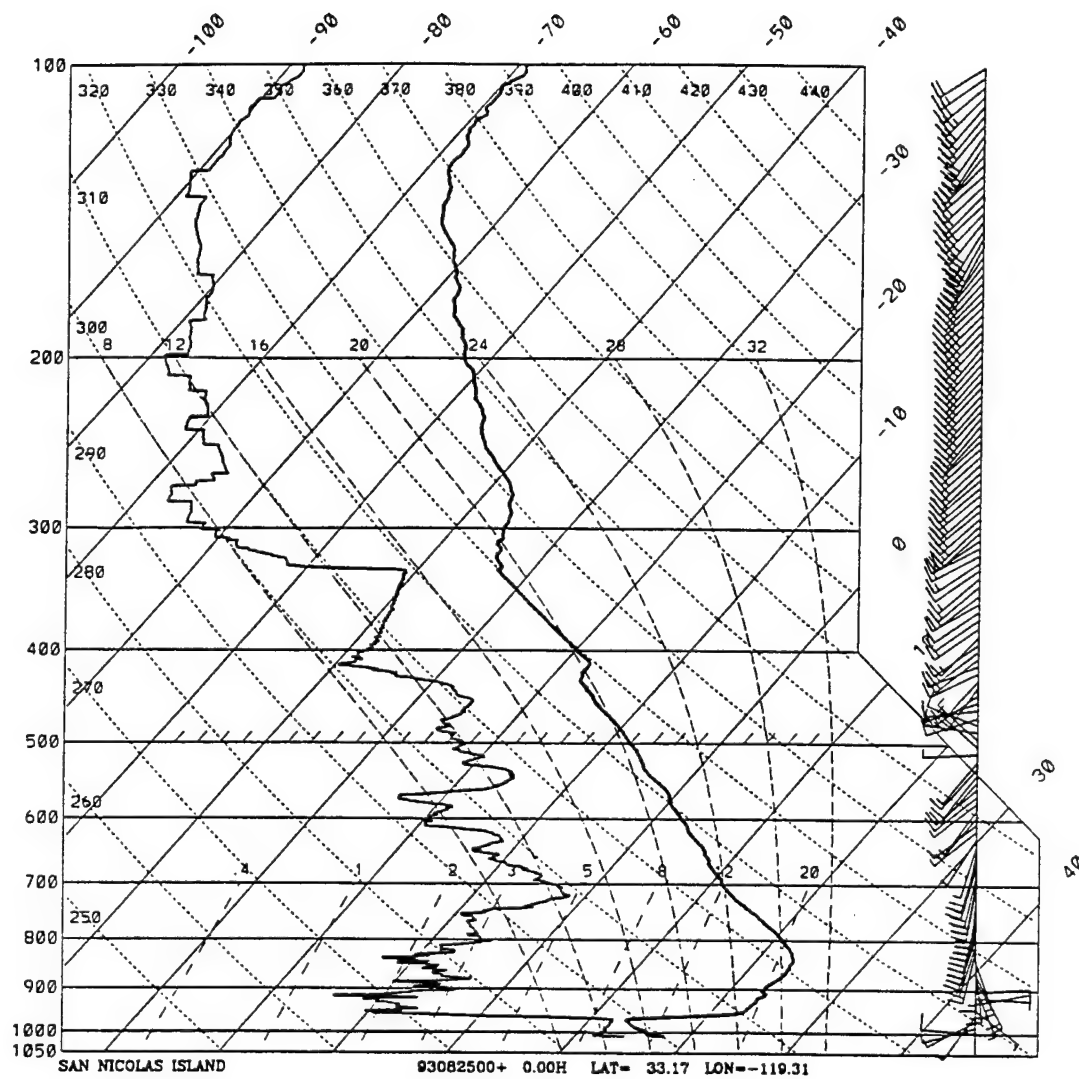


Figure 3.3. San Nicolas Island observed Skew-T diagram, 0000z, 25 August, 1993. The sharp gradients in temperature and moisture near 960 mb mark the top of the MBL.

Second, moisture availability in the Los Angeles Basin was reduced to half the normal values specified in the land-use MM5 look-up tables (Grell et al. 1994), because modeling research has shown that summertime soil moisture over California tends to be lower, for individual land-use types, than is represented in the standard MM5 version (Seaman et al. 1995). Third, the background vertical diffusion was reduced from $1 \text{ m}^2 \text{ s}^{-1}$ to $0.01 \text{ m}^2 \text{ s}^{-1}$. Comparison of MBL potential temperature cross sections based on model runs using these two diffusion values are shown in Figs. 3.4 and 3.5. Leidner (1995) found that the larger diffusion value was too strong to preserve vertical gradients at the top of the MBL or to allow new gradients to evolve in time.

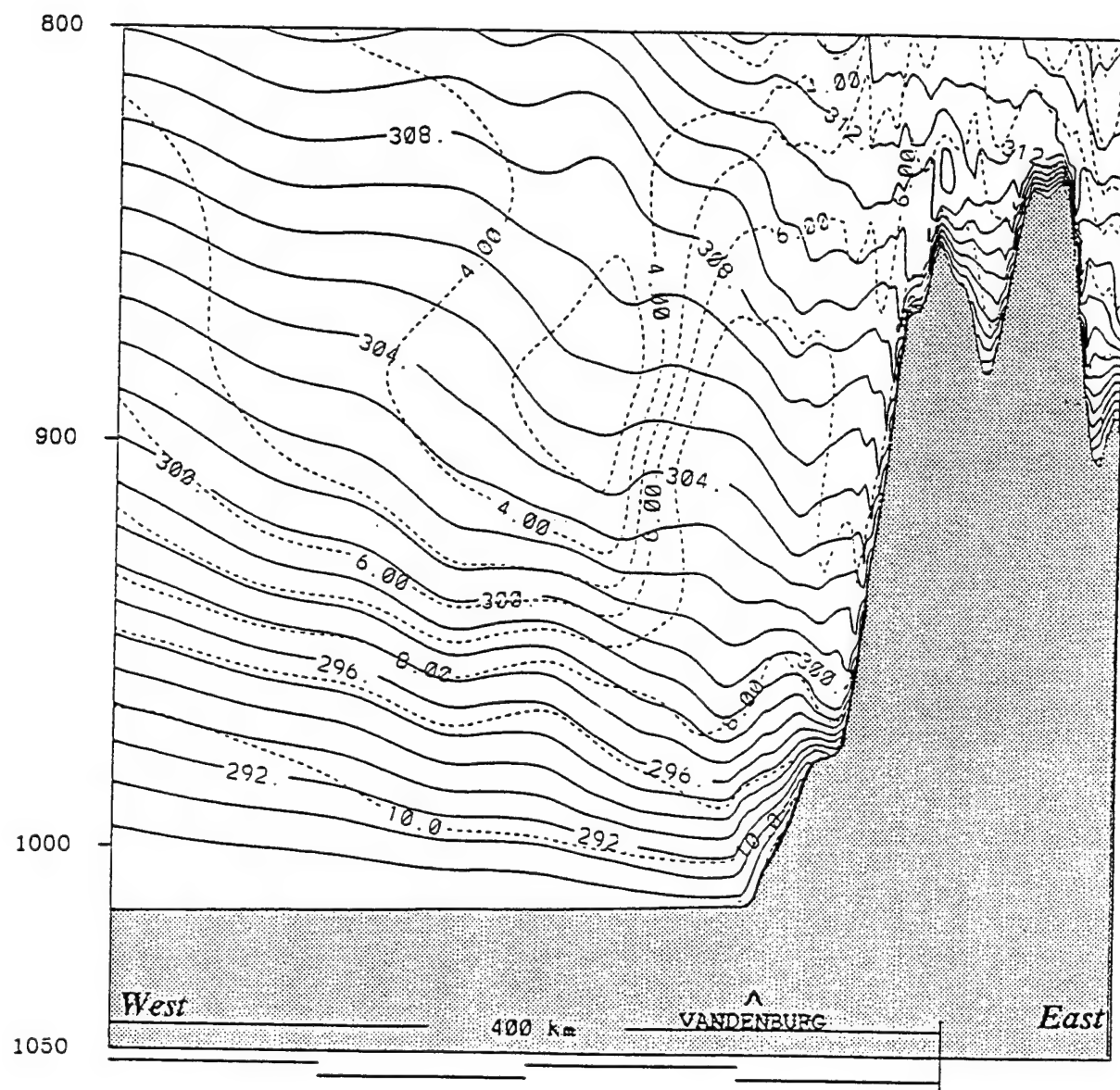


Figure 3.4. Simulated west-east cross section through Vandenburg 4 August 1990, 1200 Z. Cross section is a 12-h forecast from 4-km mesh using normal background vertical diffusion ($1.0 \text{ m}^2 \text{ s}^{-1}$). Potential temperature is solid, 1 K contours, and water vapor mixing ratio is dashed; 1 g kg^{-1} contours (Leidner 1995).

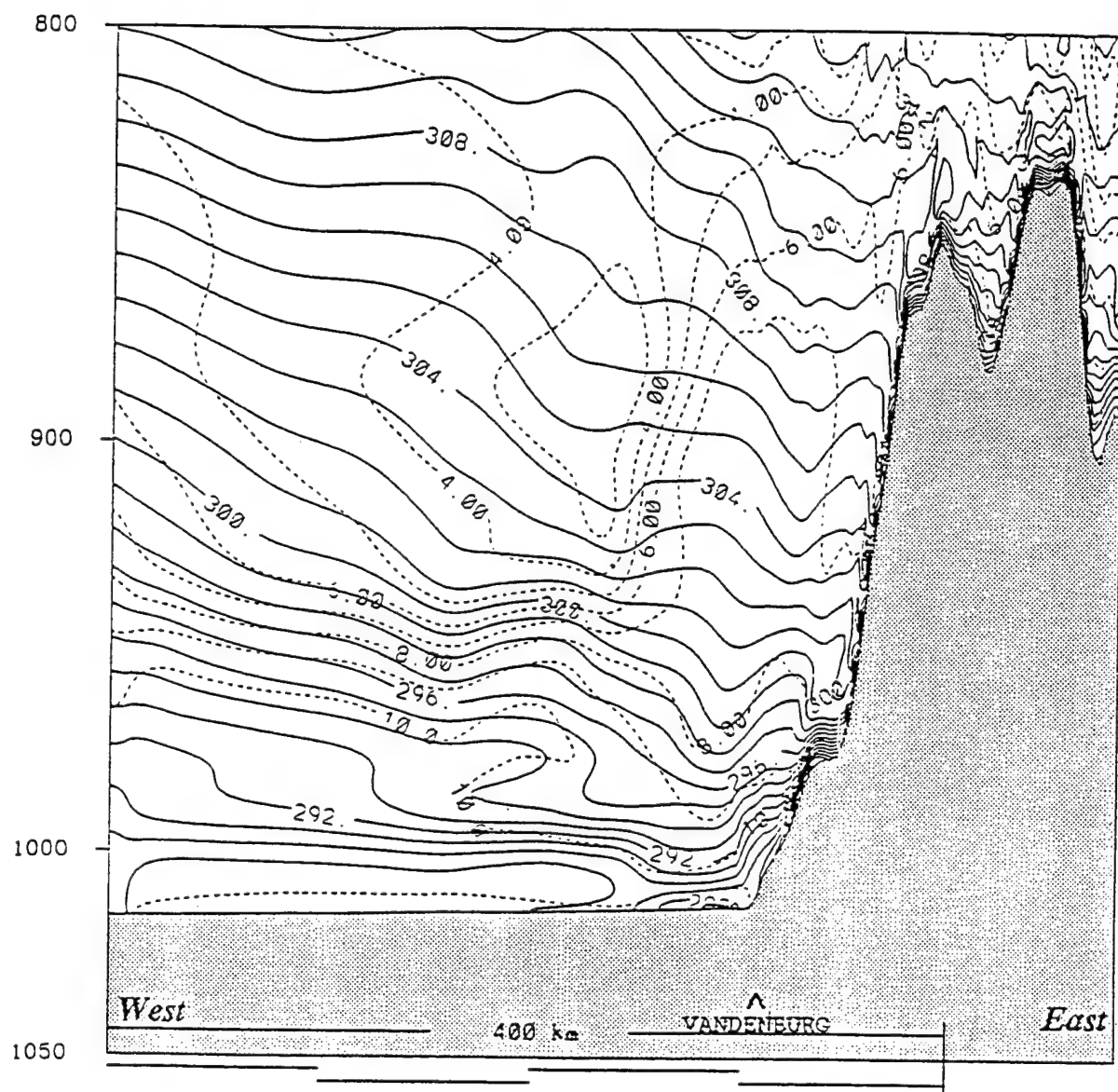


Figure 3.5. Simulated west-east cross section through Vandenburg 4 August 1990, 1200 Z. Cross section is a 12-h forecast from 4-km mesh using reduced background vertical diffusion ($0.1 \text{ m}^2 \text{ s}^{-1}$). Potential temperature is solid, 1 K contours, and water vapor mixing ratio is dashed; 1 g kg^{-1} contours (Leidner 1995).

Chapter 4

CASE DESCRIPTION

This research focuses on the time period from 1200z, 24 August 1993 to 1200z, 31 August 1993. Based on synoptic scale meteorological analysis, this segment of the VOCAR study period provides the best opportunity to investigate the effects of variability in the large scale subsidence on MBL height and accordingly, the EM trapping layer and duct height. The following sections will discuss observed meteorological and refractive conditions during the case period.

4.1 Observed Synoptic Scale Conditions.

The large scale atmospheric dynamics observed at the onset of this period are representative of summer climatological conditions in the East Pacific. The 500 mb geopotential height surface for 1200z, 24 August, shows ridging over the East Pacific with a trough of low heights over the northwest United States (Fig. 4.1). The ridge builds northward and increases in strength through the first three days of the period (Fig. 4.2). During the latter portion of the period (1200z, 31 August), the ridge shifts far to the north to 48°N and 142°W which allows a belt of low heights to emerge farther to the south extending from the Northern California coast to Hawaii (Fig. 4.3). The temporal variation of the 500 mb heights for three representative locations approximately 450 km west of the California coast, not far from the VOCAR area, is shown in Fig. 4.4. The

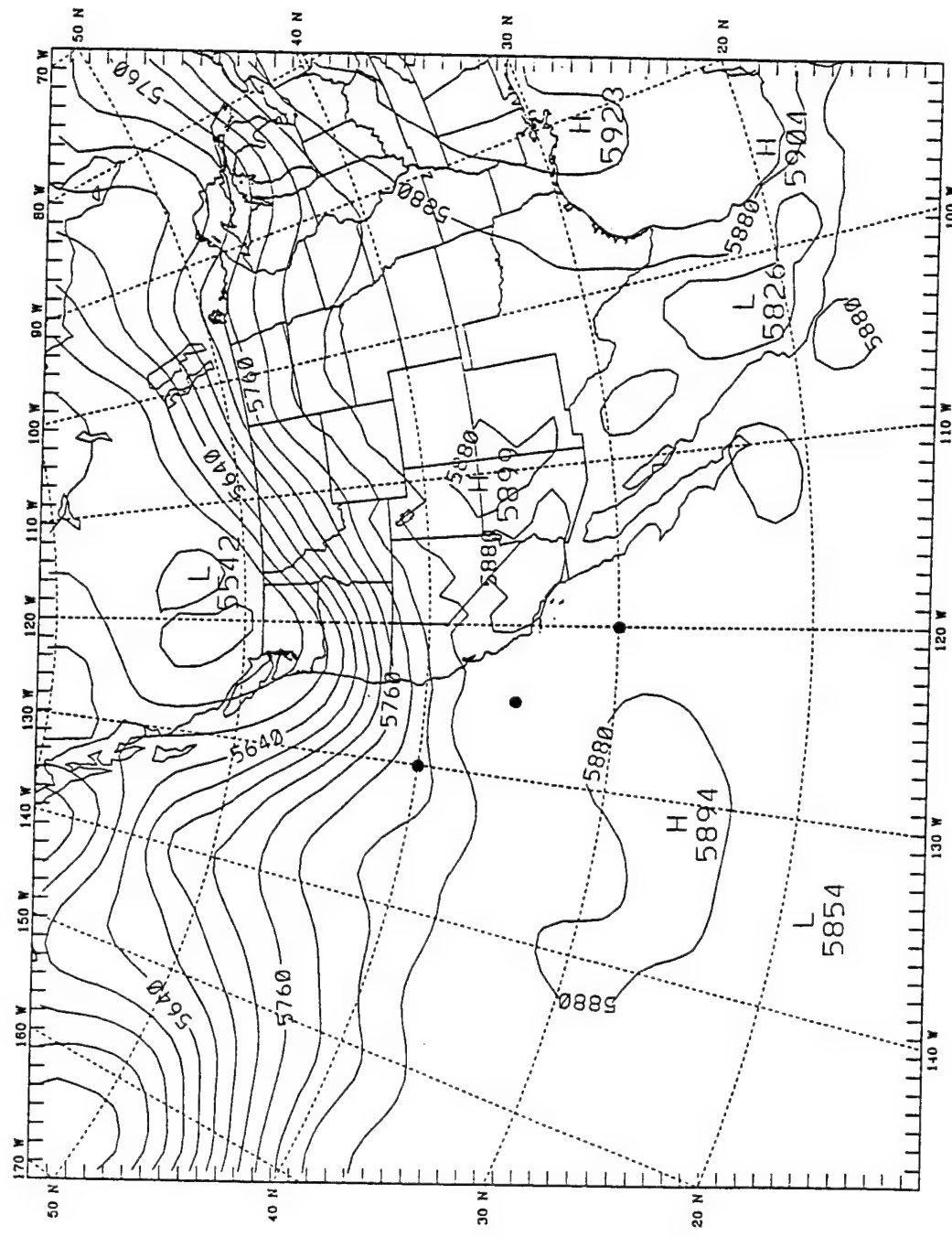


Figure 4.1 500 mb Geopotential Height (GPH) Analysis, 1200z, 24 August 1993. The East Pacific Ridge axis is along 140° W longitude with troughing over the northwestern United States. Locations used for Figs. 4.4 and 5.3 are marked by heavy dots.

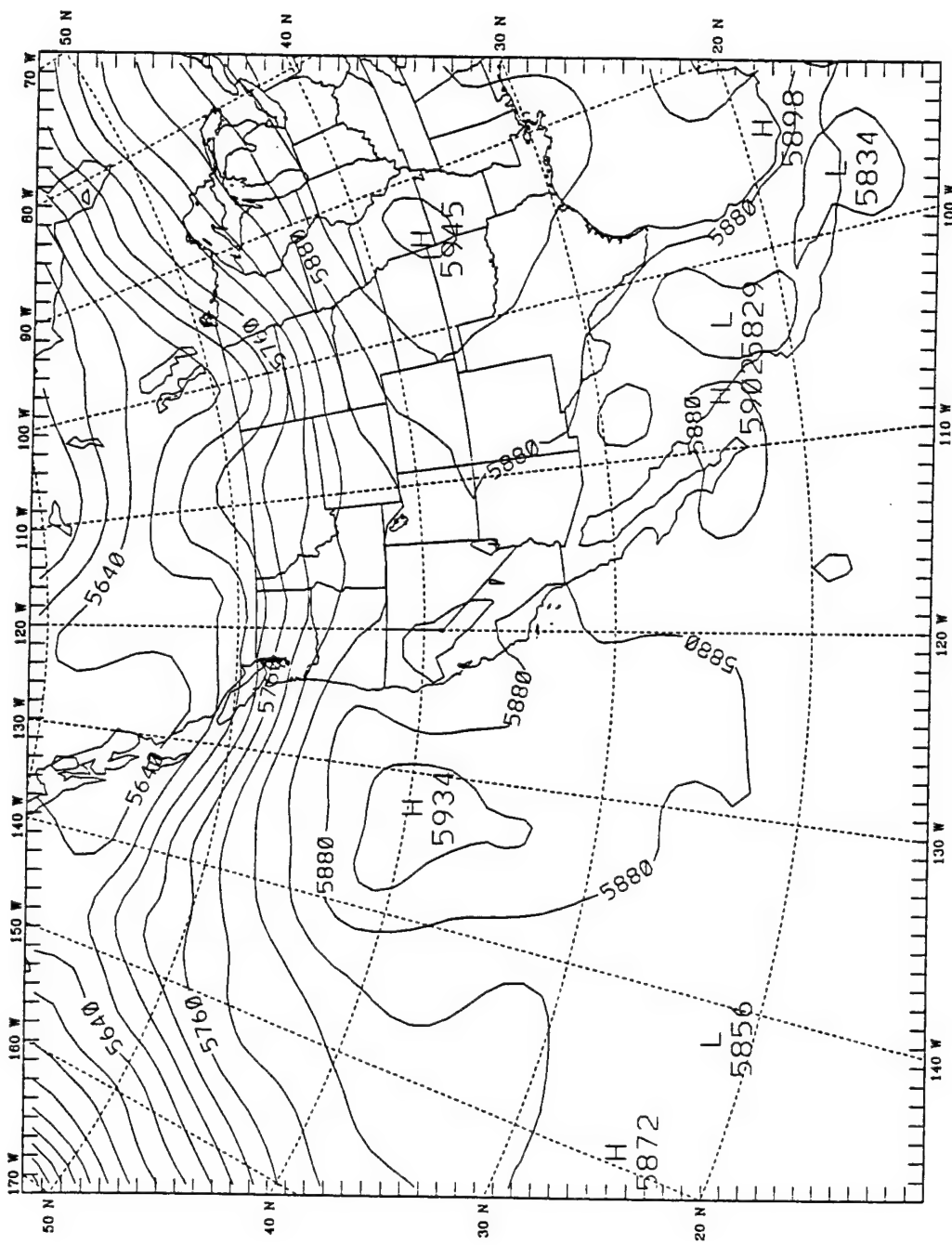


Figure 4.2 500 mb Geopotential Height Analysis, 1200z, 27 August 1993. The East Pacific Ridge axis extends to the northwest and southeast from the High at 132° W longitude. This time corresponds to the period of strongest subsidence.

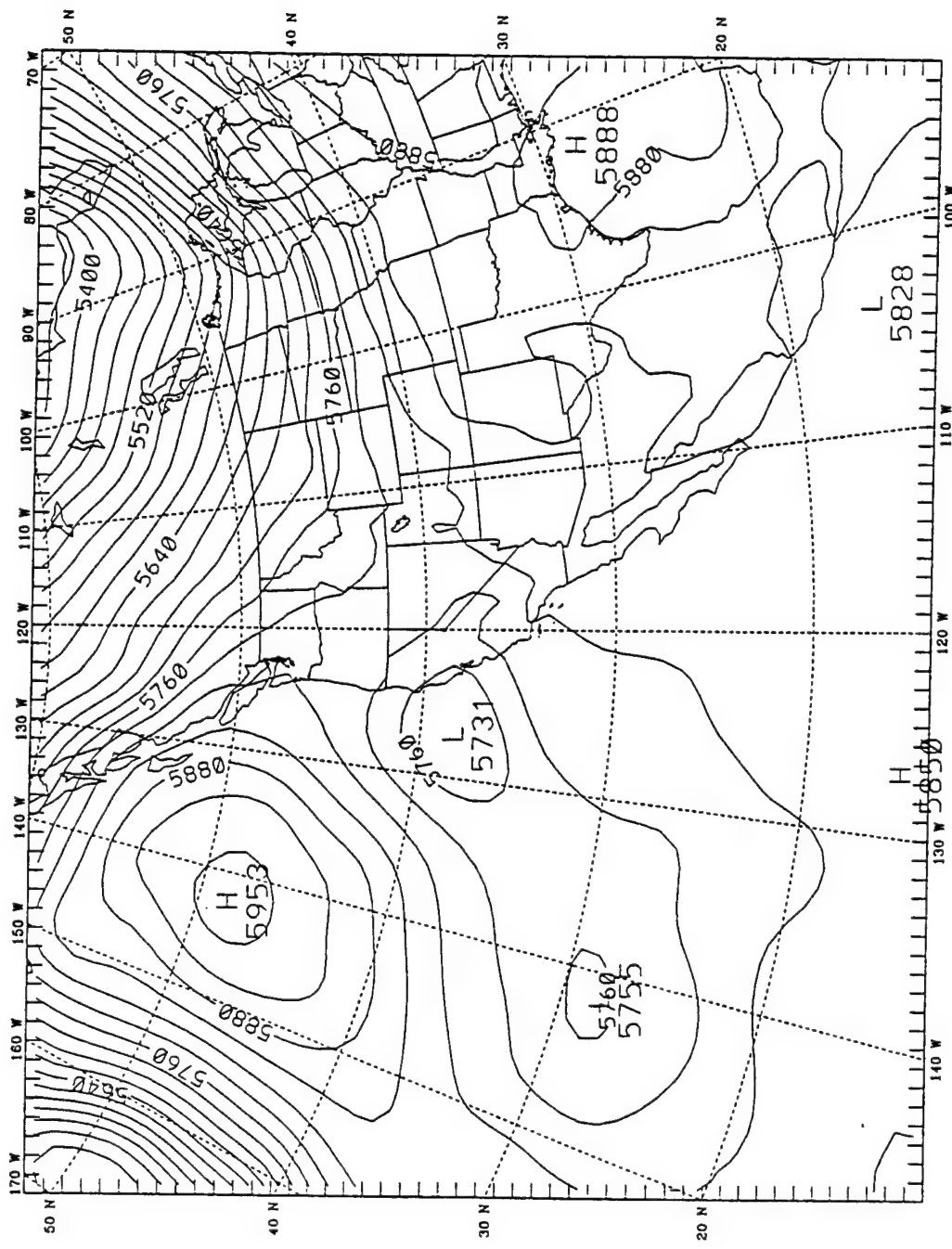


Figure 4.3 500 mb Geopotential Height Analysis, 1200z, 31 August 1993. The East Pacific Ridge has weakened and the High has moved to the northwest. A belt of lower heights extends from northern California to Hawaii.

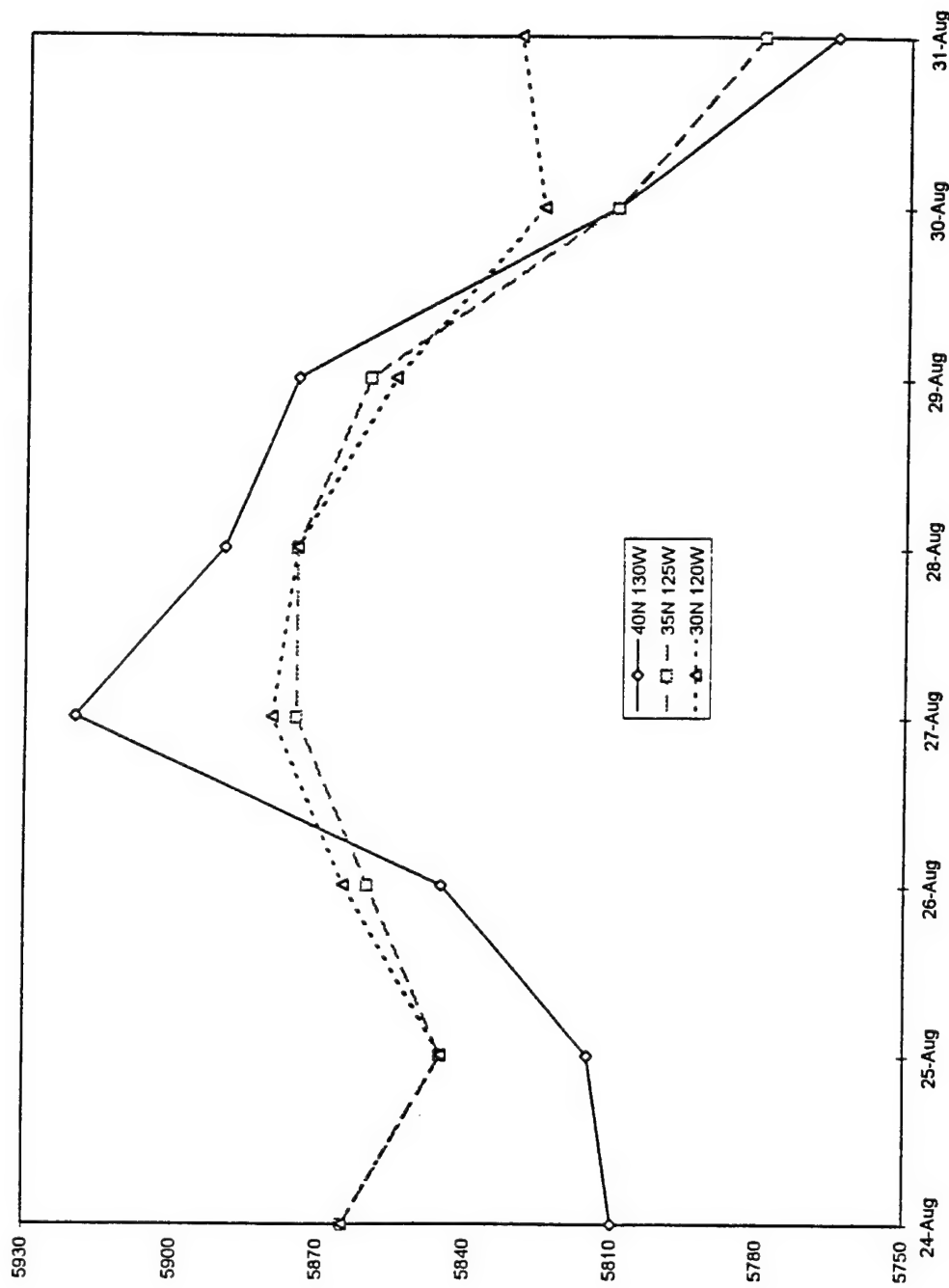


Figure 4.4 Time series of 500 mb GPH for three locations (see heavy dot, Fig 4.1) approximately 450 km west of the California coast. Values are from the 1200z analysis for each day of the case period, 24-31 August 1993.

Figure 4.4

figure indicates the strongest ridging, and hence by implication, the strongest large scale subsidence, occurs on 27 August.

The sea level pressure (SLP) analysis at the beginning of the period clearly shows the semi-permanent East Pacific High associated with the upper level ridge (Fig. 4.5). Also evident is the inverted thermal low pressure trough that routinely forms over Southern California and northwestern Mexico. Of particular note, Tropical Storm Hilary lies just off the southwestern tip of the Baja Peninsula. Over the next three days, little change is observed in the position of the high and inverted trough, while the tropical storm tracks northward along the trough (Fig. 4.6). By the end of the period (1200z, 31 August), the East Pacific High has migrated well to the north with the upper level ridge and a weak synoptic scale cyclone develops off the northern California coast (Fig. 4.7).

Typical conditions for the VOCAR area consist of northerly through northwesterly flow in a deep layer from the surface into the middle troposphere. However, normal 850 mb wind patterns are interrupted by the presence of Tropical Storm Hilary, whose storm track is shown in Fig. 4.8. The tropical storm produces southeasterly 850 mb flow ahead of it, advecting warmer, moist air into the VOCAR region on the 26-27 August (Figs. 4.9-4.11). A weak 850 mb cyclonic circulation initially at 32°N 122°W weakens as the tropical storm approaches, but later reforms and strengthens west of San Francisco Bay as the 500 mb low develops (Figs. 4.3, 4.7, and 4.11).

Upper air observations taken at San Nicolas Island at 1200z on 24-26 August, show the characteristic nature of the summertime MBL (Figs. 4.12-4.15). Note the sharp gradients in moisture and temperature indicating the top of the MBL (around 960 mb in

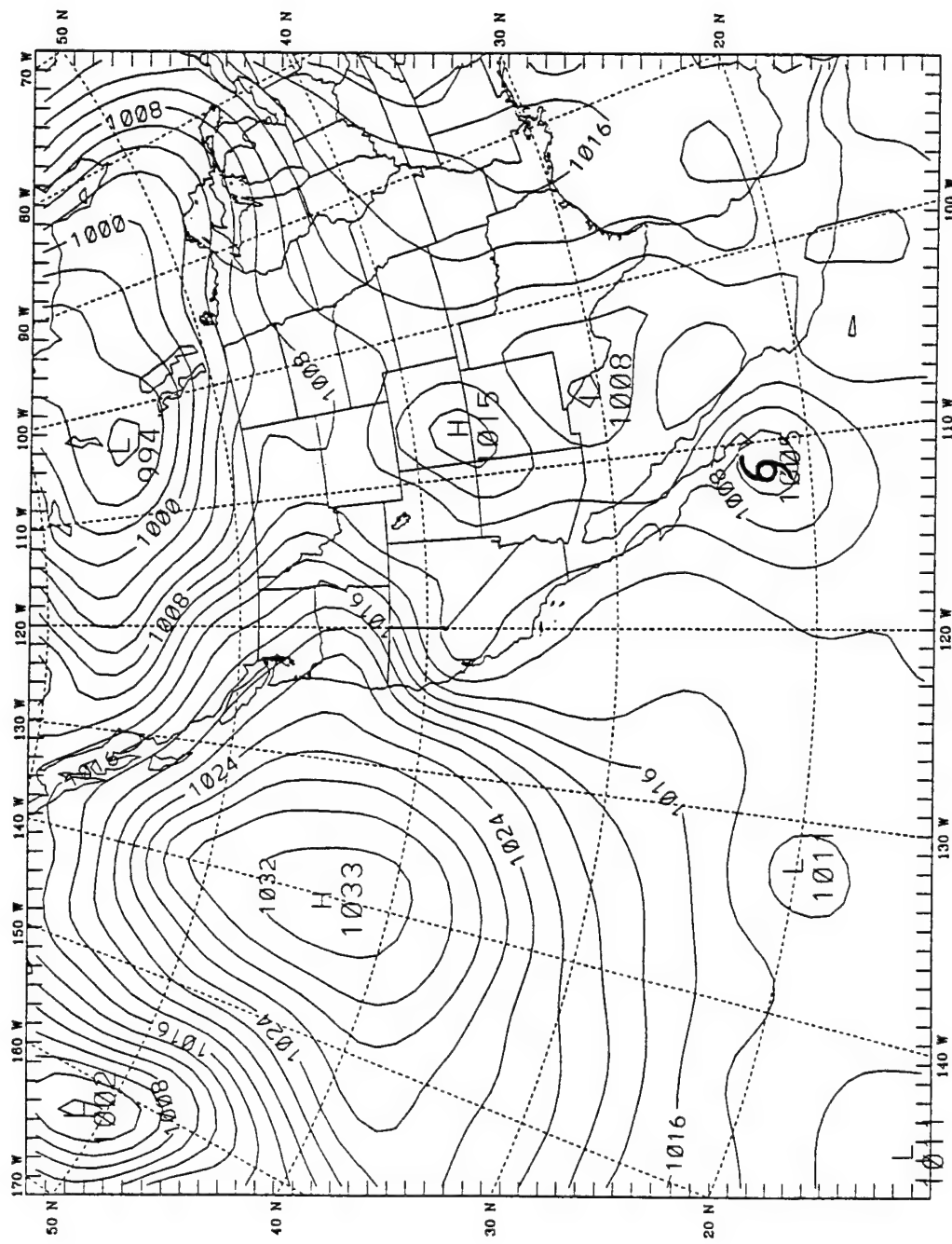


Figure 4.5 Sea Level Pressure (SLP) analysis, 1200z, 24 August 1993. The East Pacific High is located at 140°W longitude while Tropical Storm Hilary is just off the Baja peninsula. Inverted troughing extends from T. S. Hilary up into northern California.

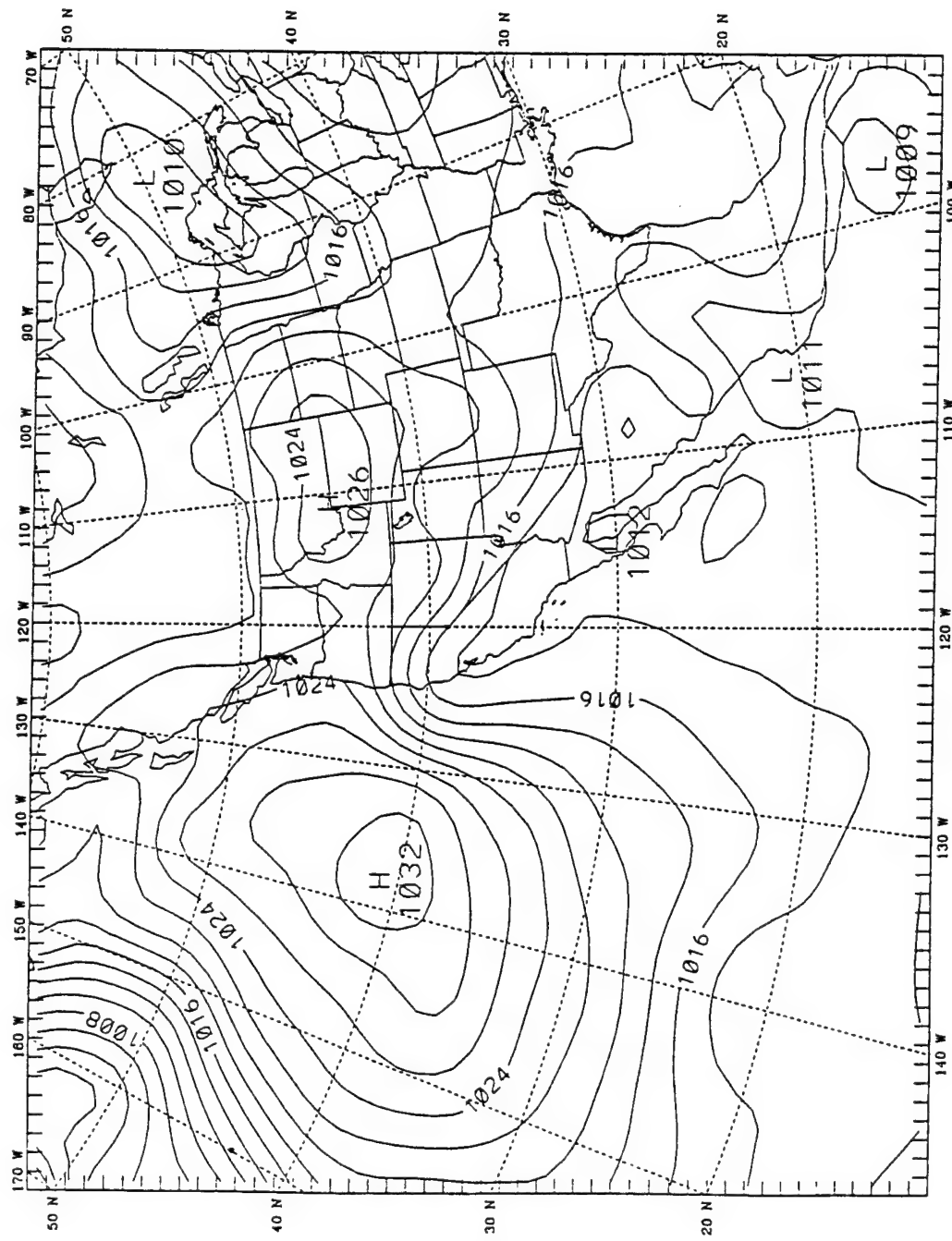


Figure 4.6 Sea Level Pressure (SLP) analysis, 1200z, 27 August 1993. The East Pacific High has moved slightly to the southeast and the remains of Hilary are in the northern Gulf of California. Inverted troughing over California persists, but the pressure gradient has weakened west of San Francisco.

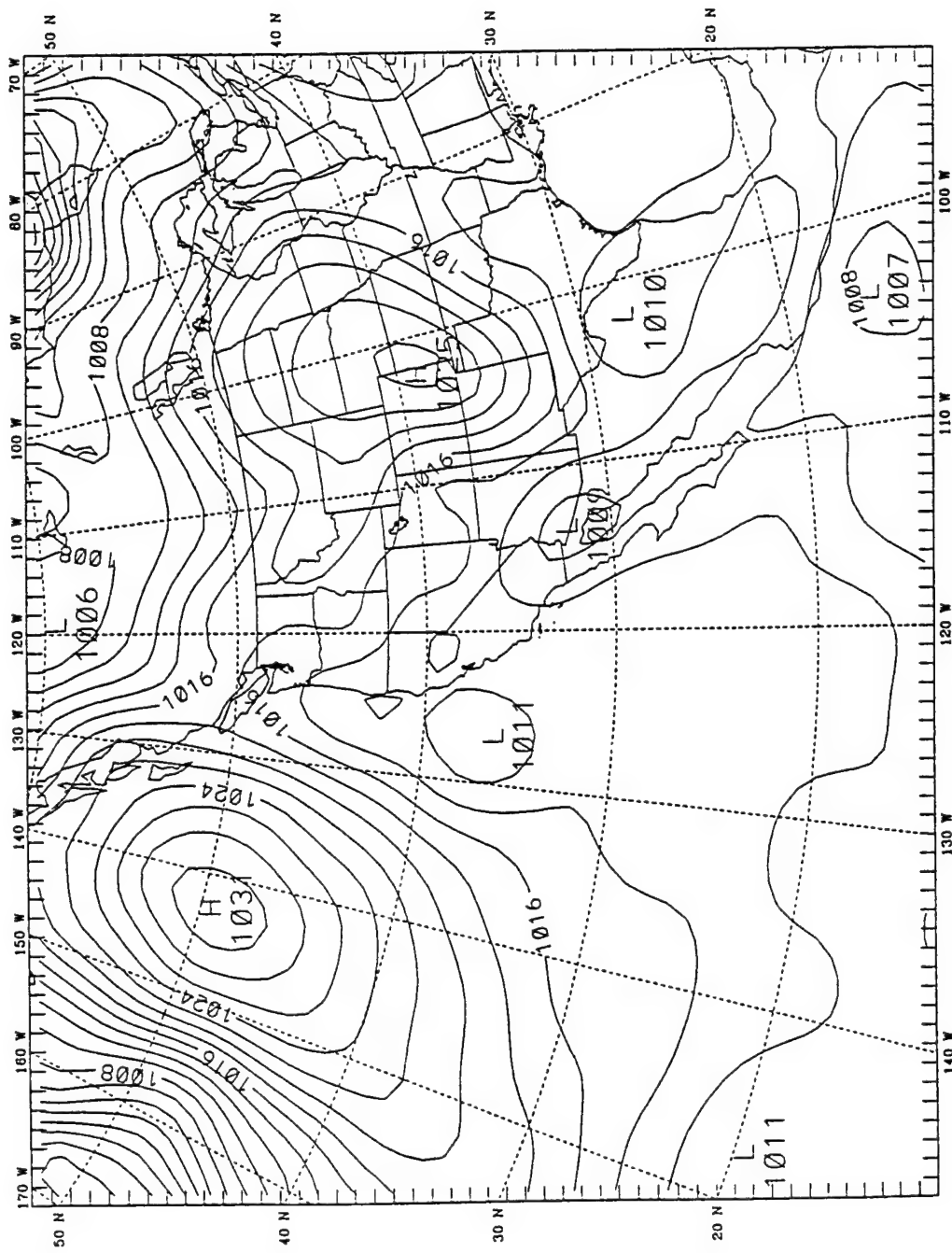


Figure 4.7 Sea Level Pressure (SLP) analysis, 1200z, 31 August 1993. The East Pacific High has moved nearly 9° latitude to the north. A synoptic scale Low has formed off the California coast with another Low pressure system in the northern Gulf of California.

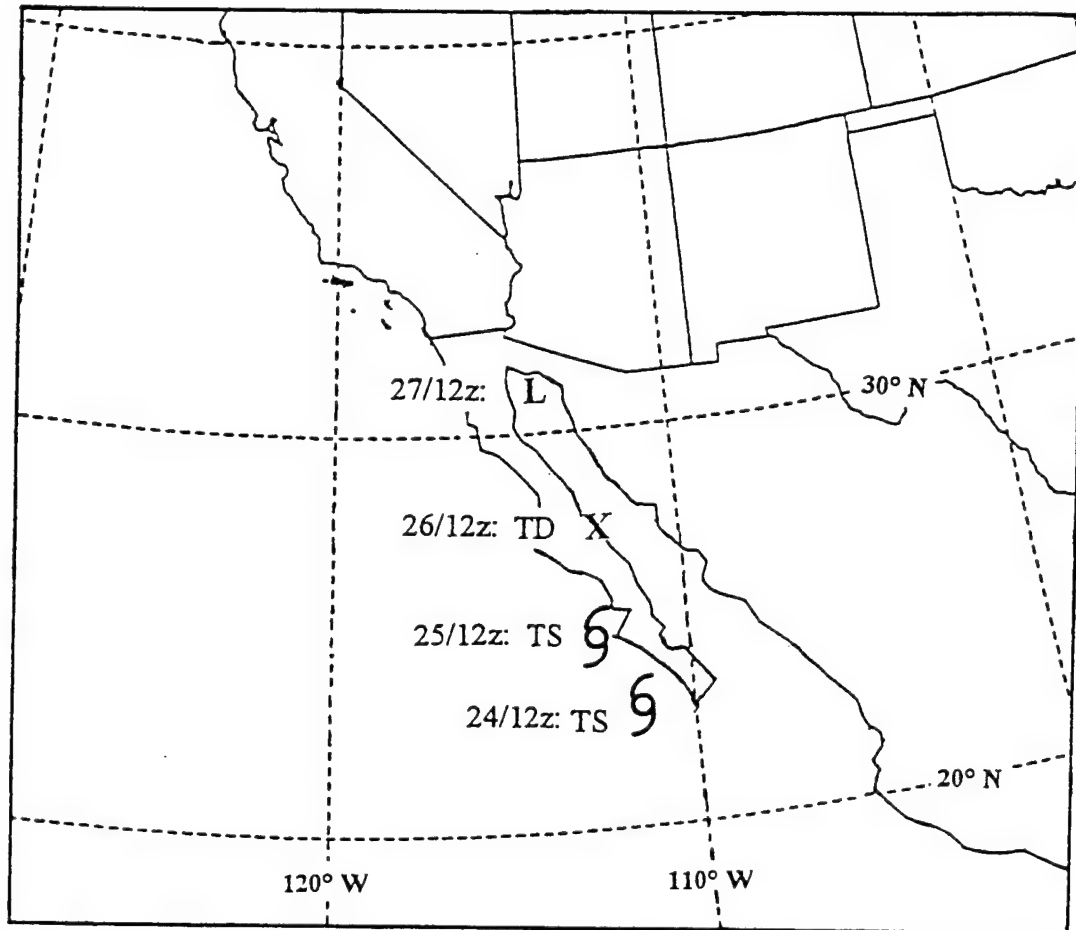


Figure 4.8 Storm track for Tropical Storm Hilary during the case period. The 12z positions are plotted using standard meteorological symbols.

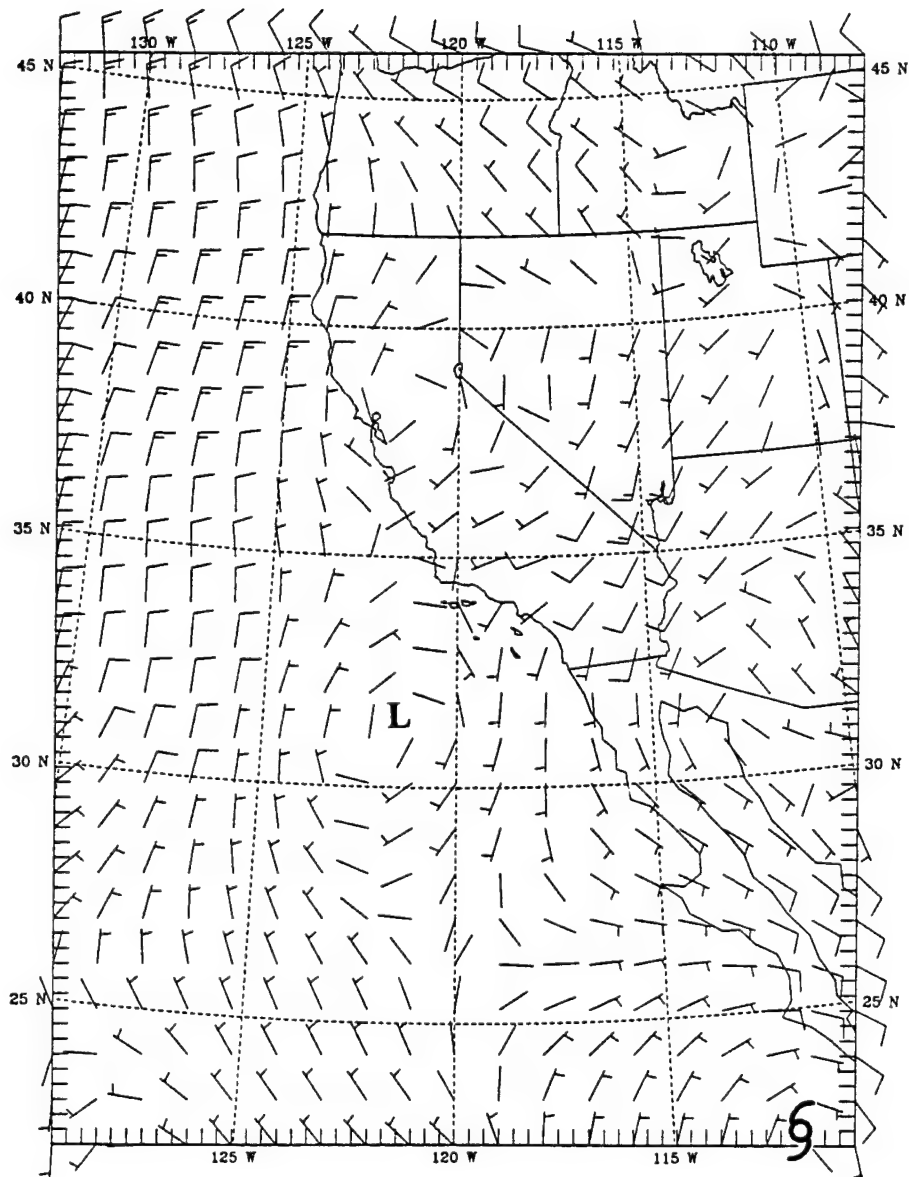


Figure 4.9 850 mb Wind analysis, 1200z, 24 August 1993. Note the cyclonic circulation southwest of the VOCAR region and southerly flow off the coast of the Baja Peninsula.

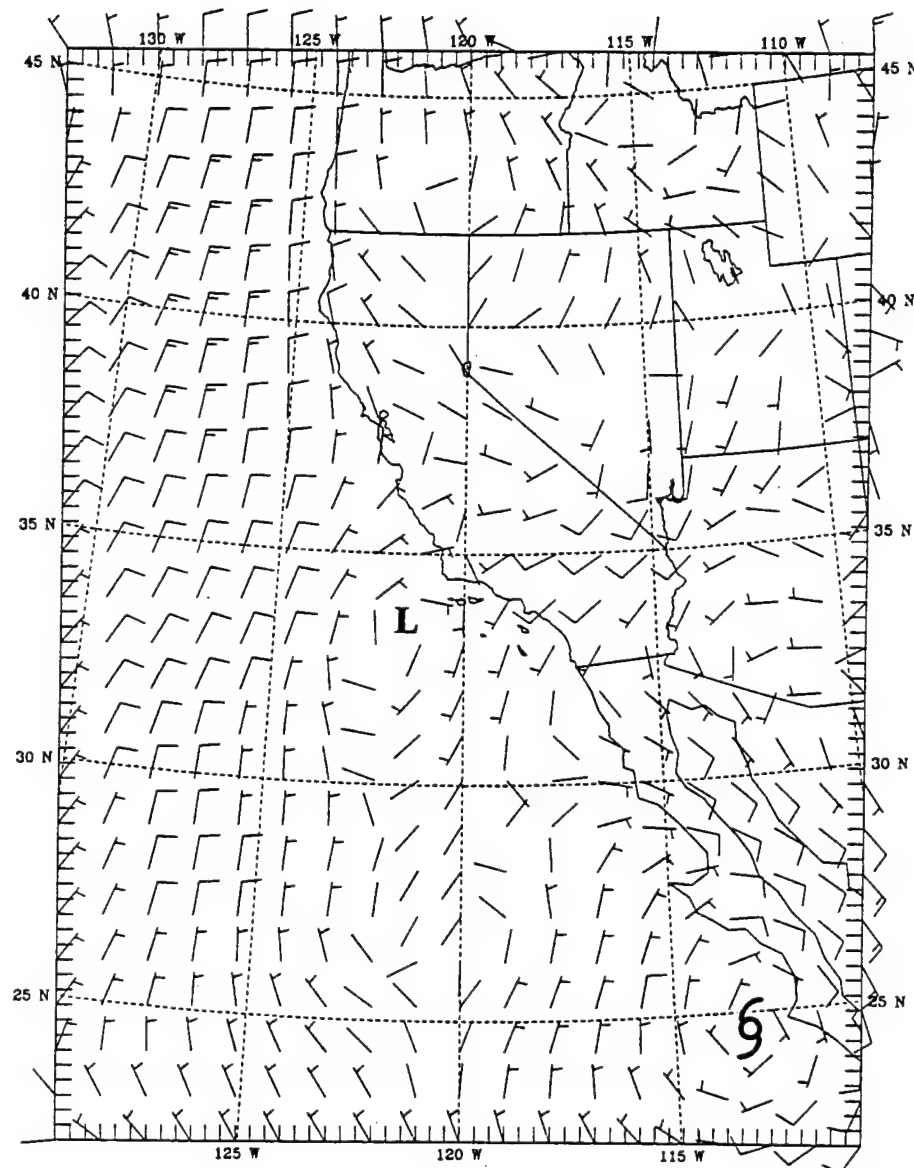


Figure 4.10 850 mb Wind analysis, 1200z, 25 August 1993. The cyclonic circulation southwest of the VOCAR region has moved to the north. Weak southerly flow exists west of extreme northern Mexico. Tropical Storm Hilary is seen near 25° N.

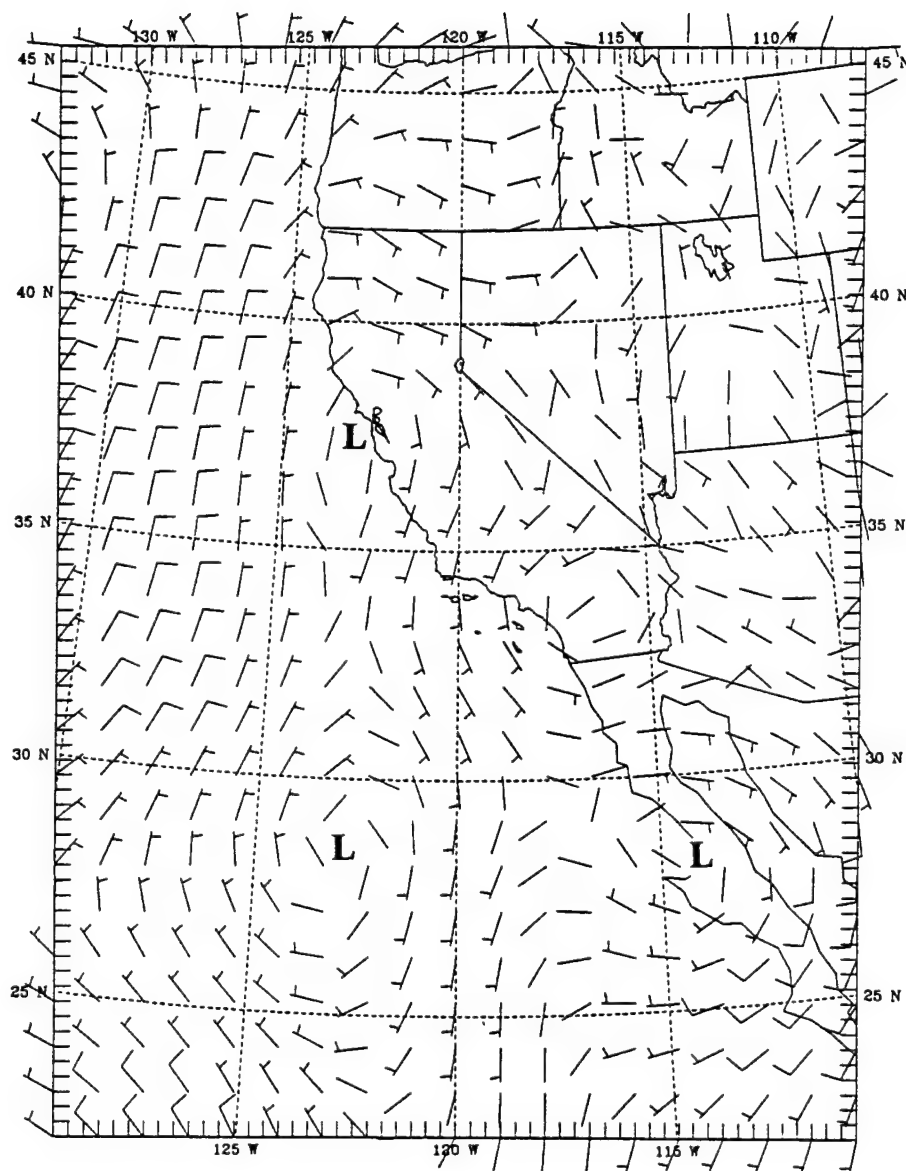


Figure 4.11 850 mb Wind analysis, 1200z, 26 August 1993. Hilary, now a tropical depression, is near 27.5° N. The flow pattern from Hilary is advecting moisture into the VOCAR region, which exhibits southerly flow.

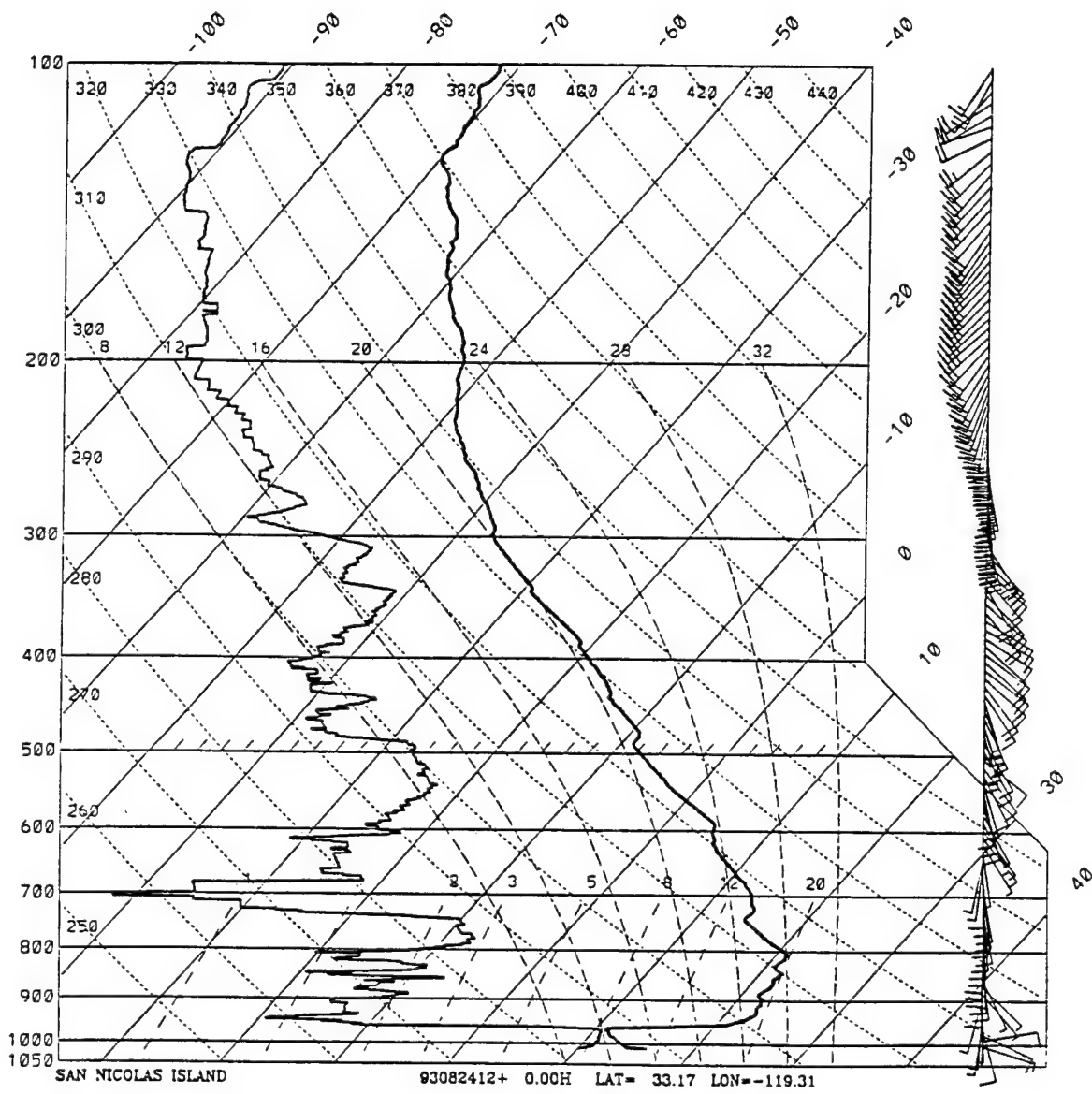


Figure 4.12 San Nicolas Island observed Skew-T diagram, 1200z, 24 August, 1993. The sharp gradients in temperature and moisture near 960 mb mark the top of the MBL. Winds flow is southerly in a deep layer above the MBL.

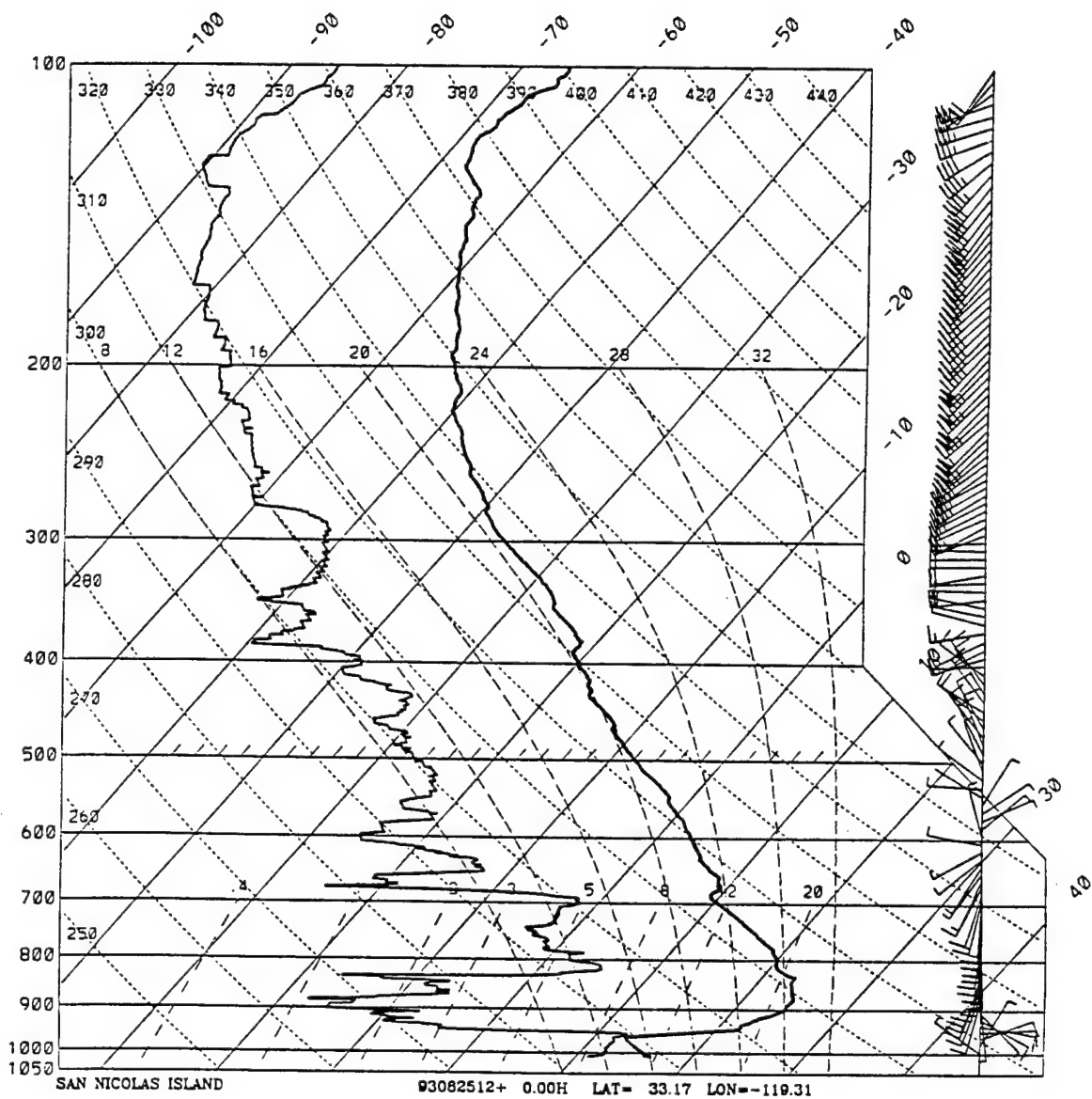


Figure 4.13 San Nicolas Island observed Skew-T diagram, 1200z, 25 August, 1993. Note the moistening of the layer from 700-810 mb. Also, the deep layer of southerly flow above the MBL persists.

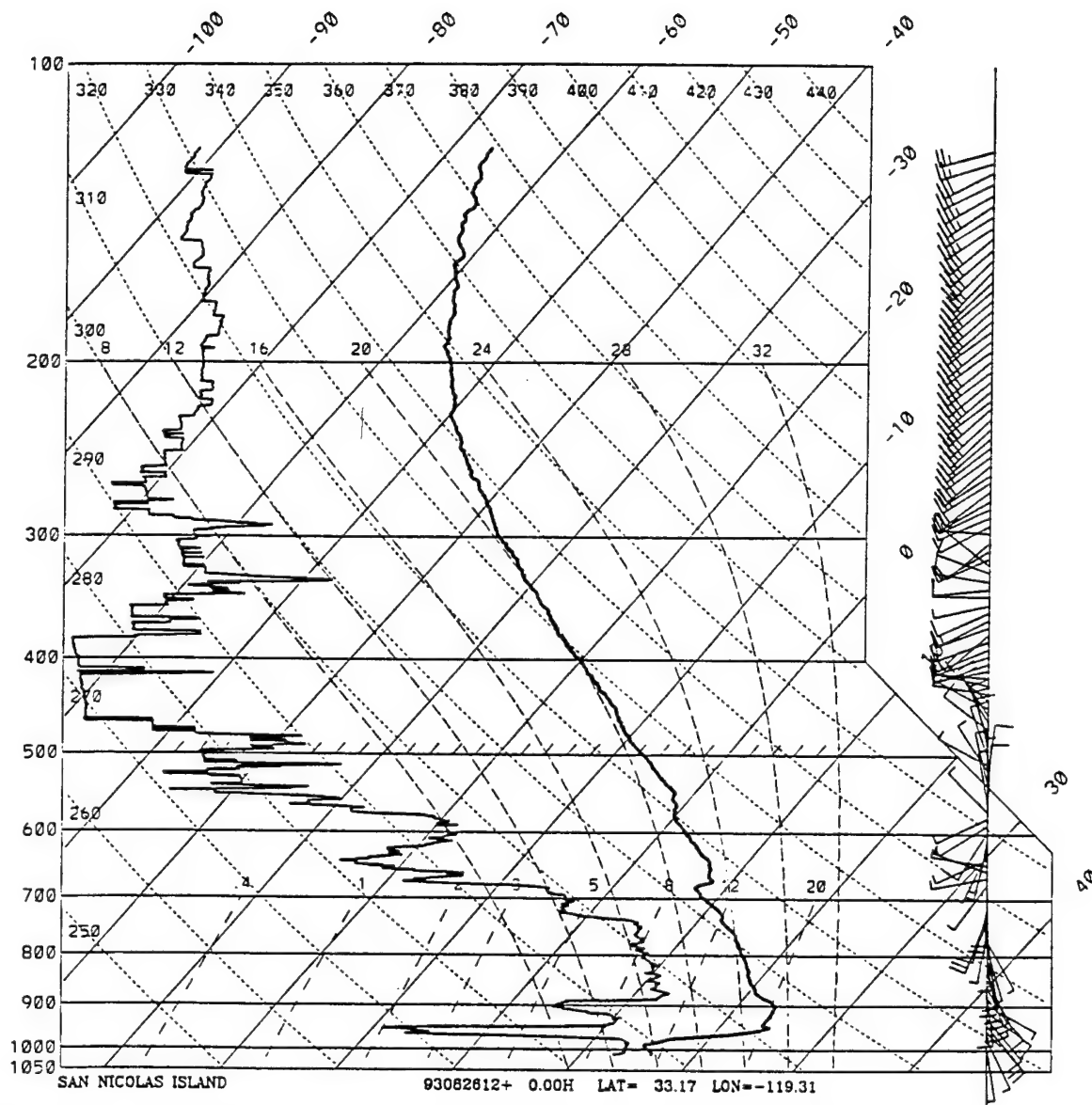


Figure 4.14 San Nicolas Island observed Skew-T diagram, 1200z, 26 August, 1993. Moistening of the atmosphere above the MBL continues, resulting in a shallow dry layer just above the MBL. Also, the inversion base has lowered to around 985 mb.

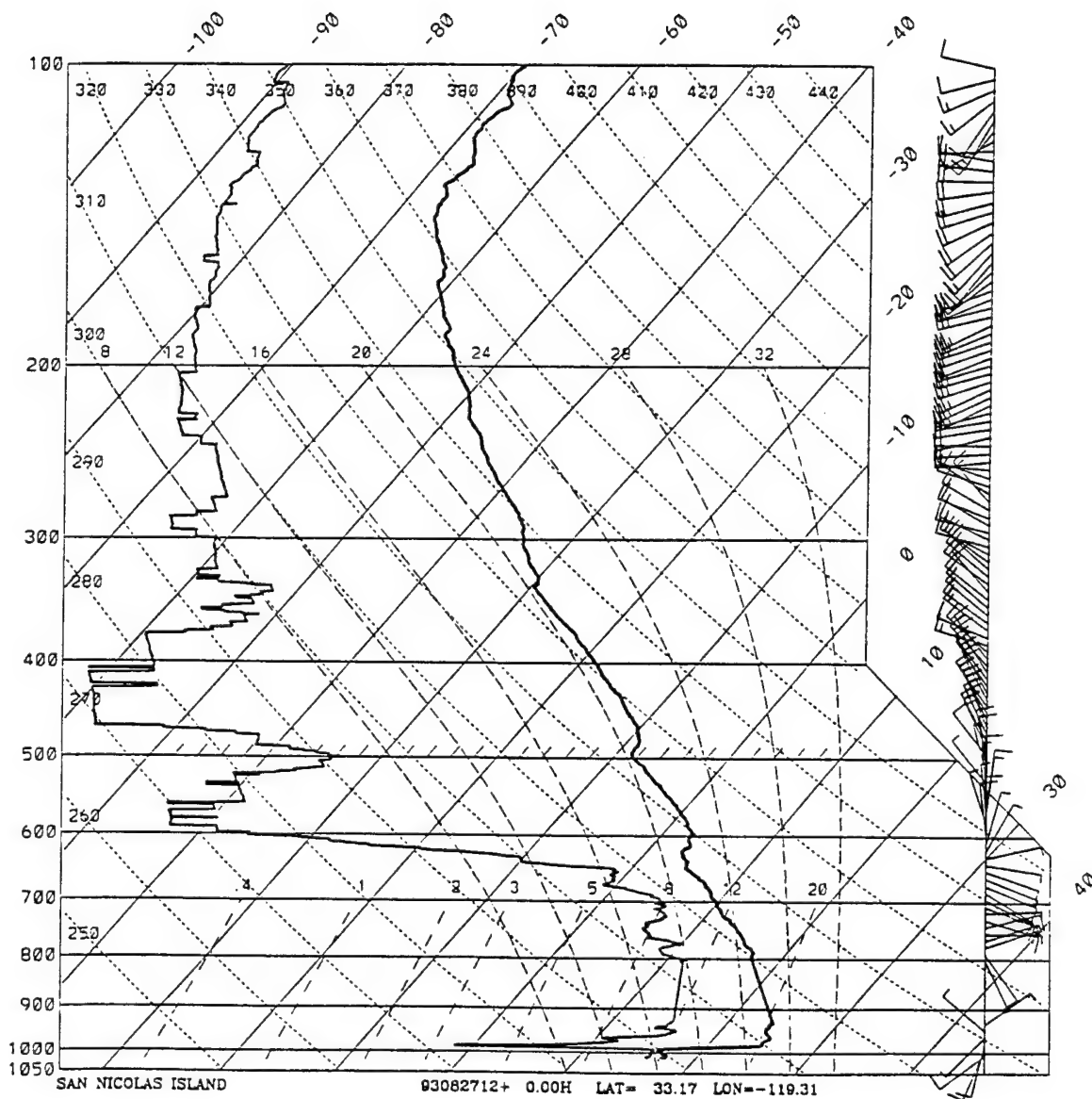


Figure 4.15 San Nicolas Island observed Skew-T diagram, 1200z, 27 August, 1993. The deep layer of southerly flow has evolved into easterly flow from 620-780 mb. The remarkably thin dry layer atop the MBL persists and the inversion base is near 1000 mb.

Fig. 4.12). This series of radiosondes shows little change in the temperature structure, but a very significant change in the moisture structure. Recall that large gradients of moisture produce significant changes in the M-profile. These figures reveal a large increase in moisture in the layer from near 700 mb down to near the top of the MBL. Wind barbs show the persistent southerly to southeasterly flow in this layer, eventually becoming easterly at the top of the moist layer by 27 August. This is the mid-level outflow from Tropical Storm Hilary. As a result, by 26 August, a shallow dry layer is sandwiched between the moist MBL and the moist overlying air advected into the area by the tropical storm. This "dry spike" is even shallower on 27 August. Dropsondes taken at the same time and location (not shown) confirm the "dry spike". Finally, note the lowering of the inversion base by about 40 mb (350 m) throughout the sequence.

4.2 Refractive Conditions.

During the VOCAR intensive observation period, high resolution upper air observations generally were taken every four hours (with the exception of 08z) at San Nicolas Island, San Clemente Island, and Camp Pendleton. Upper air soundings for the first three days of the period were also taken aboard the Naval Post-Graduate School ship, R.V. Pt. Sur, positioned approximately halfway between Point Magu and San Clemente Island (see Fig. 1.3).

From these soundings, details of the refractive structure were calculated, including the EM duct base, trapping layer base, and trapping layer top. Recall from Fig. 1.1 that the top of the trapping layer and the EM duct are coincident and are almost always

coincident with the top of the MBL, marked by the temperature inversion. Figs. 4.16-4.19 show the temporal trend of the refractive conditions for each of the four stations. Each plot demonstrates the lowering of the EM duct and trapping layer through the first half of the case period with the lowest heights observed on 27 August when the duct is at the surface. Thereafter, both layers rise and the duct lifts off the surface to form an elevated duct. This pattern in the change of the duct and trapping layer heights is well correlated with the variation in the 500 mb GPH across the region (Fig. 4.4). A subsequent brief drop in the duct and trapping layer height occurs on 30 August (less noticeably at Camp Pendleton). Recall that the base of the EM duct is determined from the point on the M-profile directly below M_{min} at the top of the trapping layer (See Fig. 1.1). Therefore, as the modified refractivity structure changes such that M_{min} increases or decreases, the duct base rises or lowers. Examination of these time/height refractive layer plots does not indicate a clear diurnal signal, with the possible exception of Camp Pendleton on the coast (Fig. 4.19).

The height of the EM duct base, trapping layer, and top of the duct for all of these four locations has been combined in time-height charts shown in Figs. 4.20-4.22, respectively. The temporal trend of the lowering duct and trapping layer heights in the first half of the period is clear. Likewise, the rising duct and trapping layer in the latter portion of the period is unmistakable. Of note, the EM duct and trapping layer heights for the two island stations lower on 30 August 0000z, while they rise at Camp Pendleton. The generally similar patterns for all four stations shown in these figures confirm that the processes controlling the primary variations occurs on a time scale of several days and

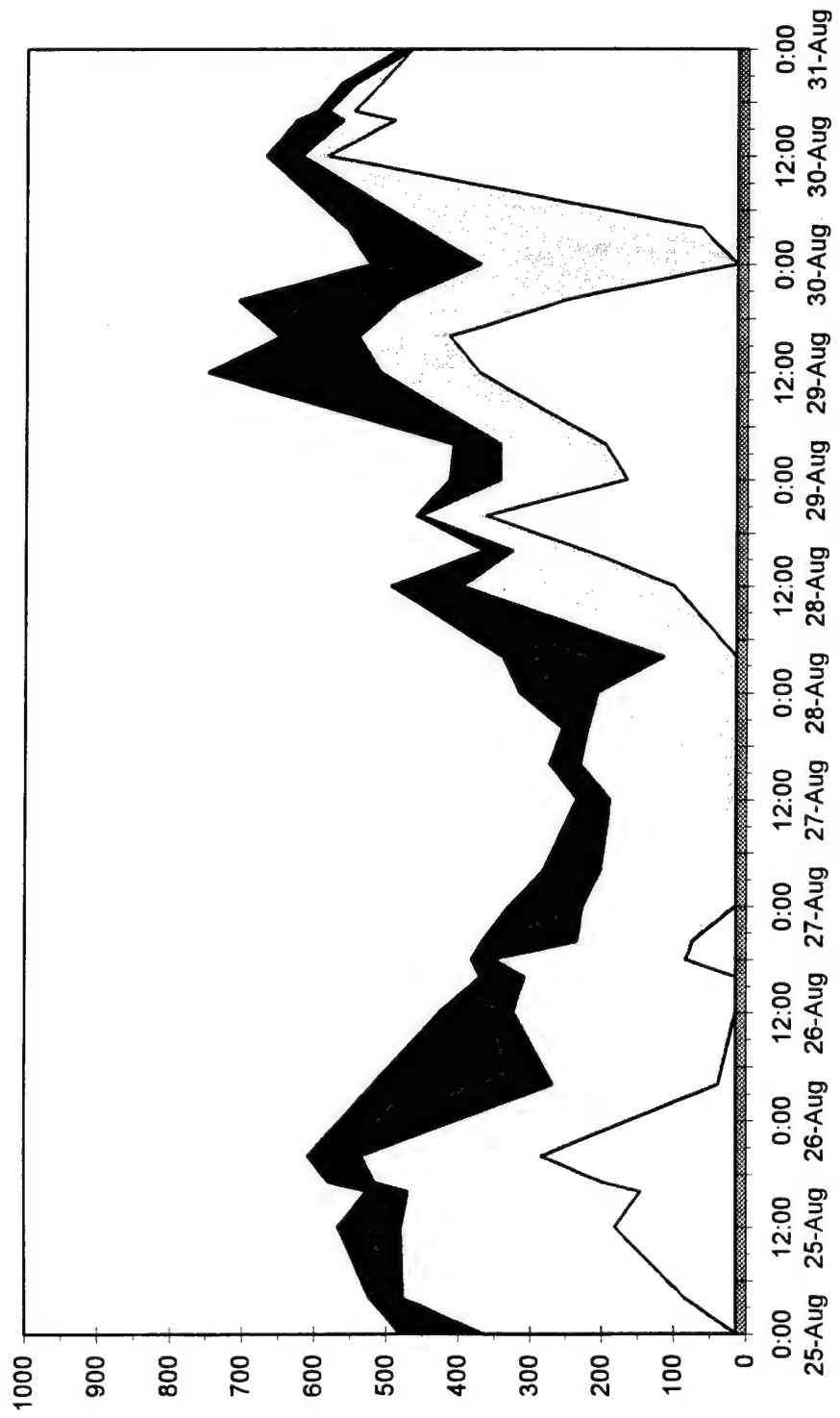


Figure 4.16 Observed refractive structure at San Nicolas Island during the case period. Time is along the abscissa, height in meters MSL is along the ordinate. Dark shading represents the trapping layer. The ducting layer extends from the trapping layer top to the bottom edge of the light shaded region.

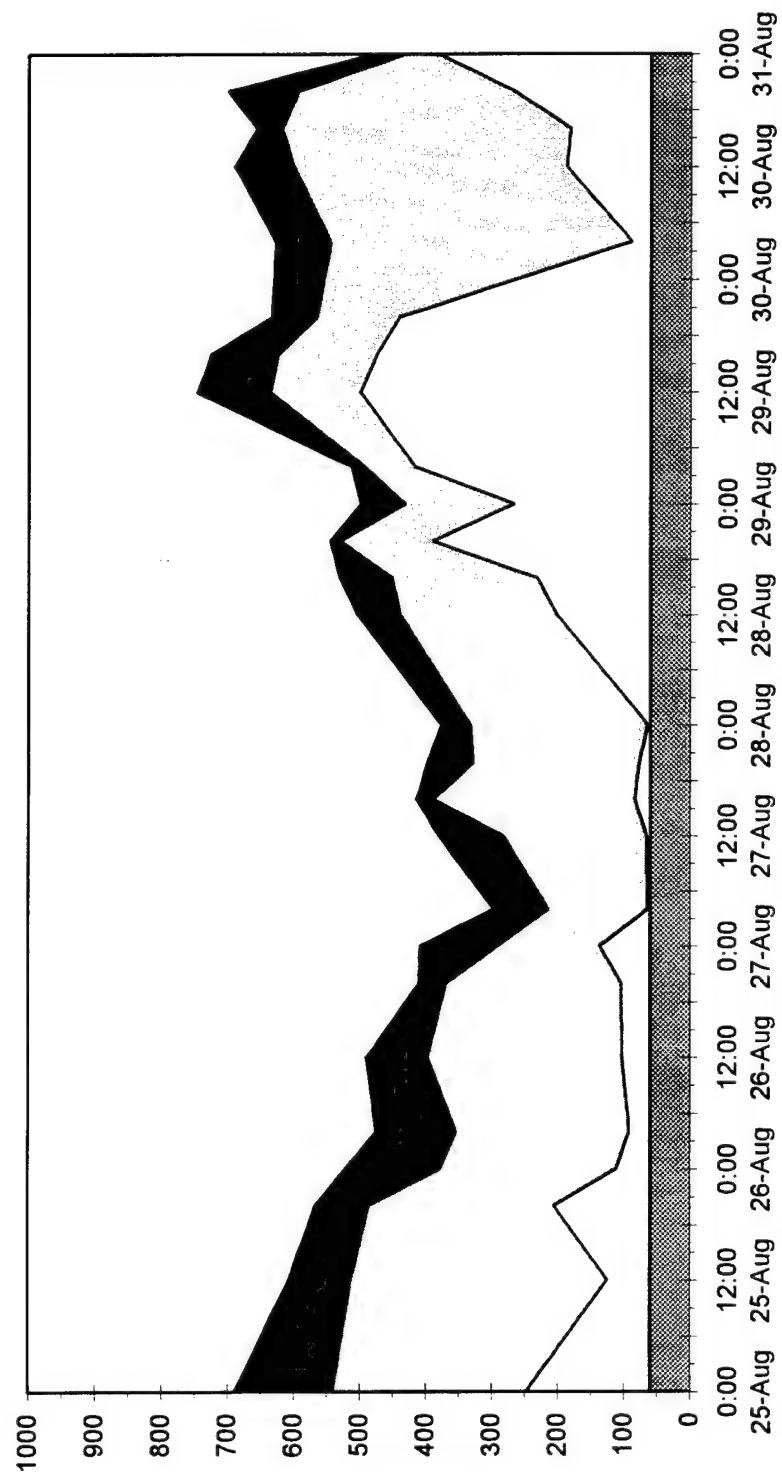


Figure 4.17 Observed refractive structure at San Clemente Island during the case period. Time is along the abscissa, height in meters MSL is along the ordinate. Dark shading represents the trapping layer. The ducting layer extends from the trapping layer top to the bottom edge of the light shaded region.

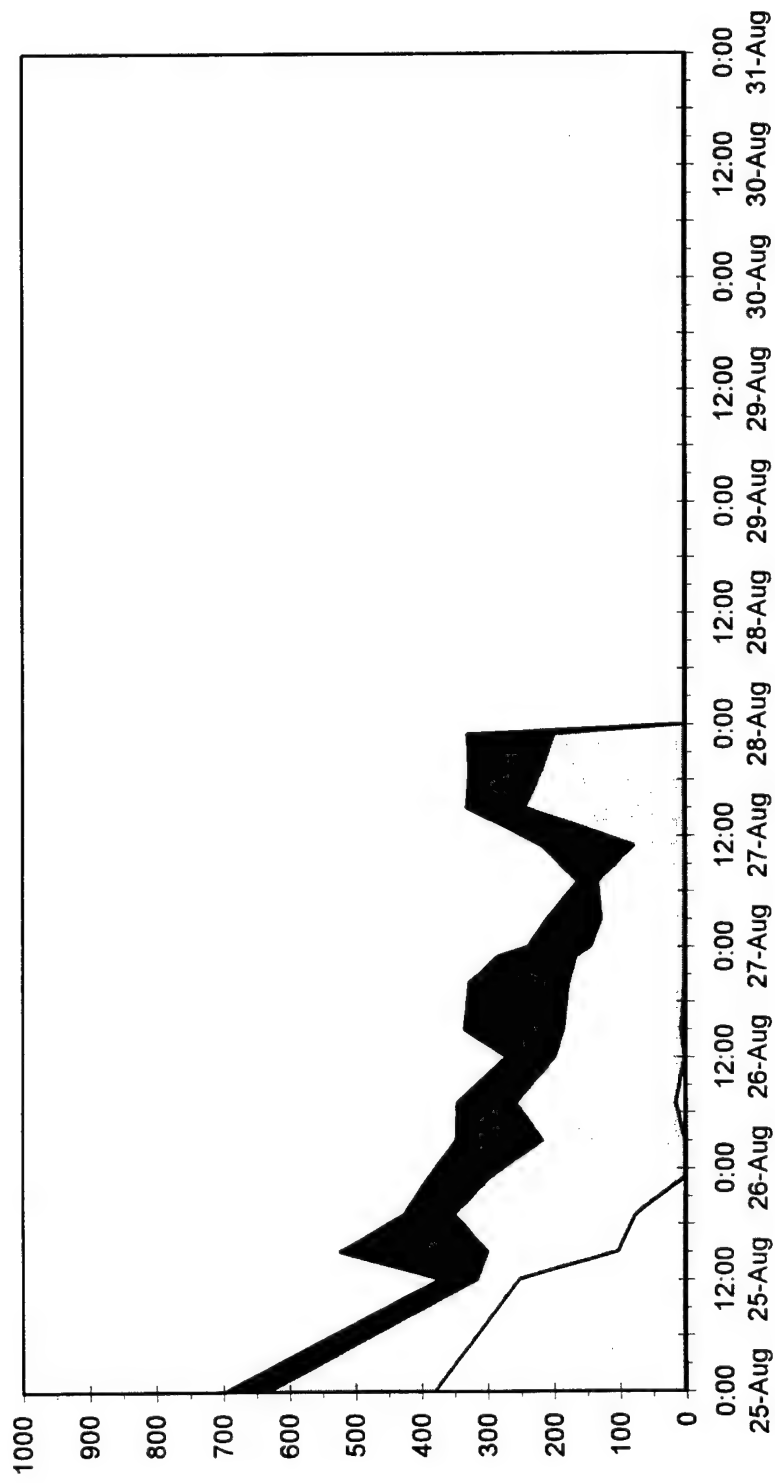


Figure 4.18 Observed refractive structure at the Research Vessel Pt. Sur during the case period. Time is along the abscissa, height in meters MSL is along the ordinate. Dark shading represents the trapping layer. The ducting layer extends from the trapping layer top to the bottom edge of the light shaded region.

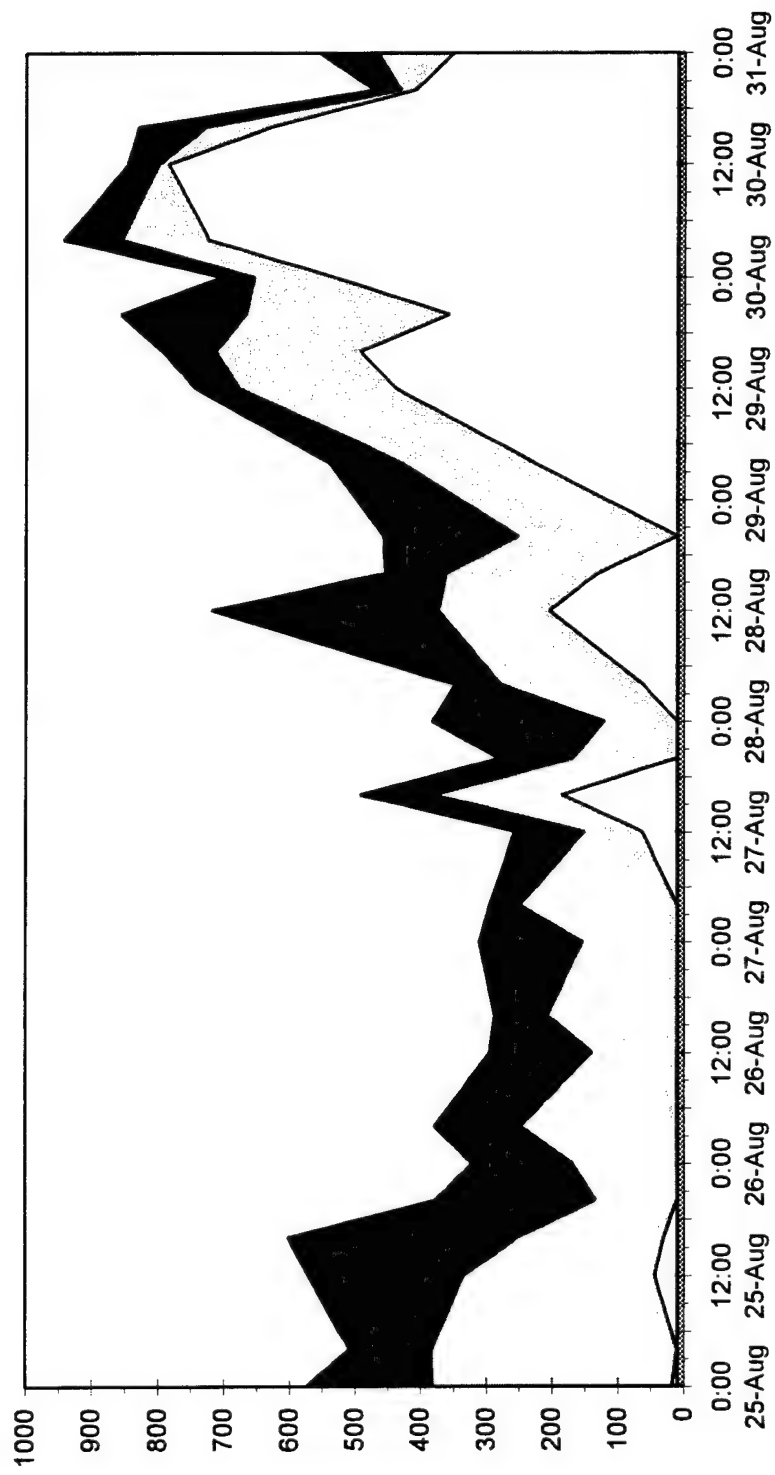


Figure 4.19 Observed refractive structure at Camp Pendleton during the case period. Time is along the abscissa, height in meters MSL is along the ordinate. Dark shading represents the trapping layer. The ducting layer extends from the trapping layer top to the bottom edge of the light shaded region.

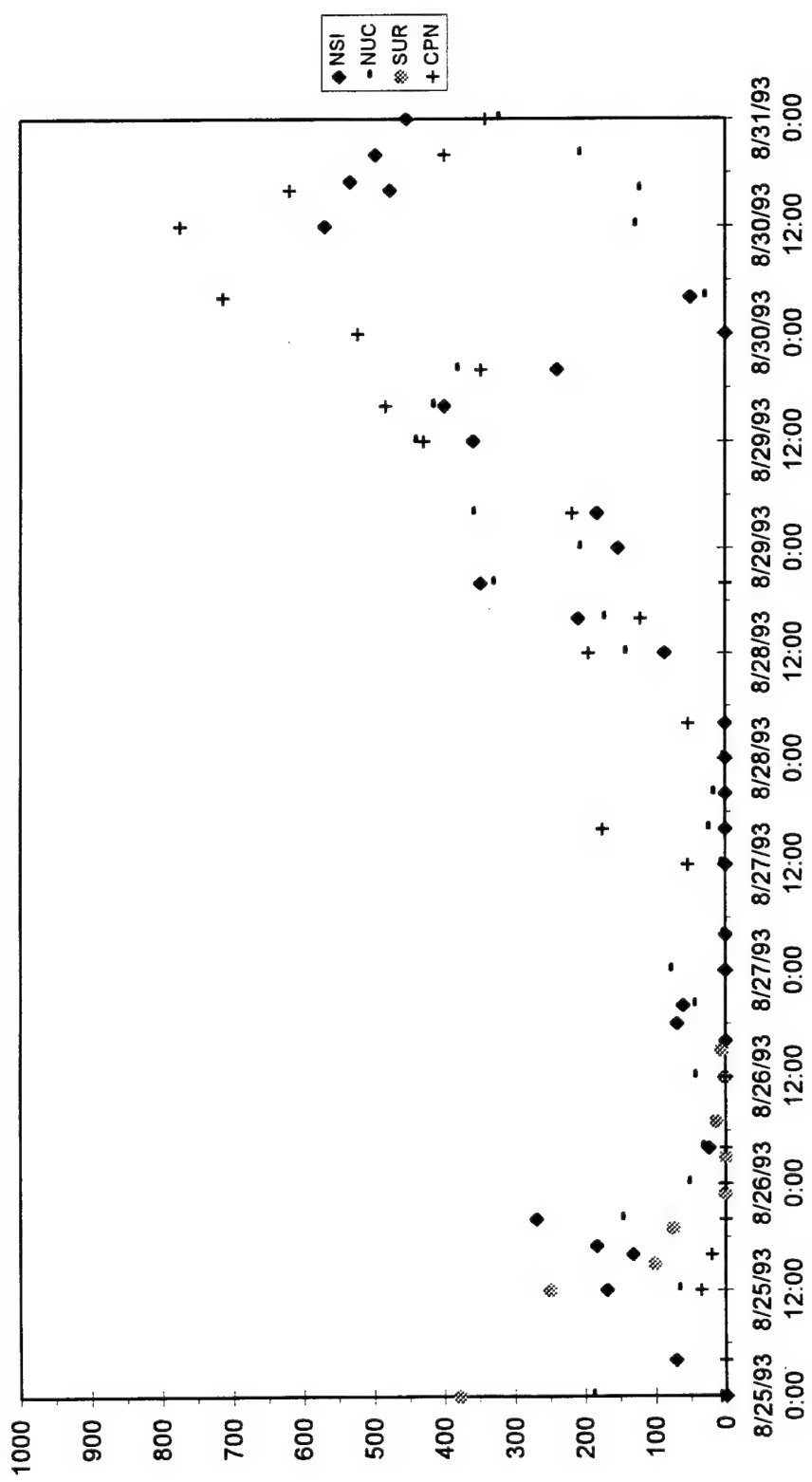


Figure 4.20 Time/Height plot of the observed duct base at: San Nicolas Island (NSI), San Clemente Island (NUC), Research Vessel Pt. Sur (SUR), and Camp Pendleton (CPN). Time is along the abscissa, height in meters AGL is along the ordinate. Note, plots on the abscissa indicate the presence of a surface duct.

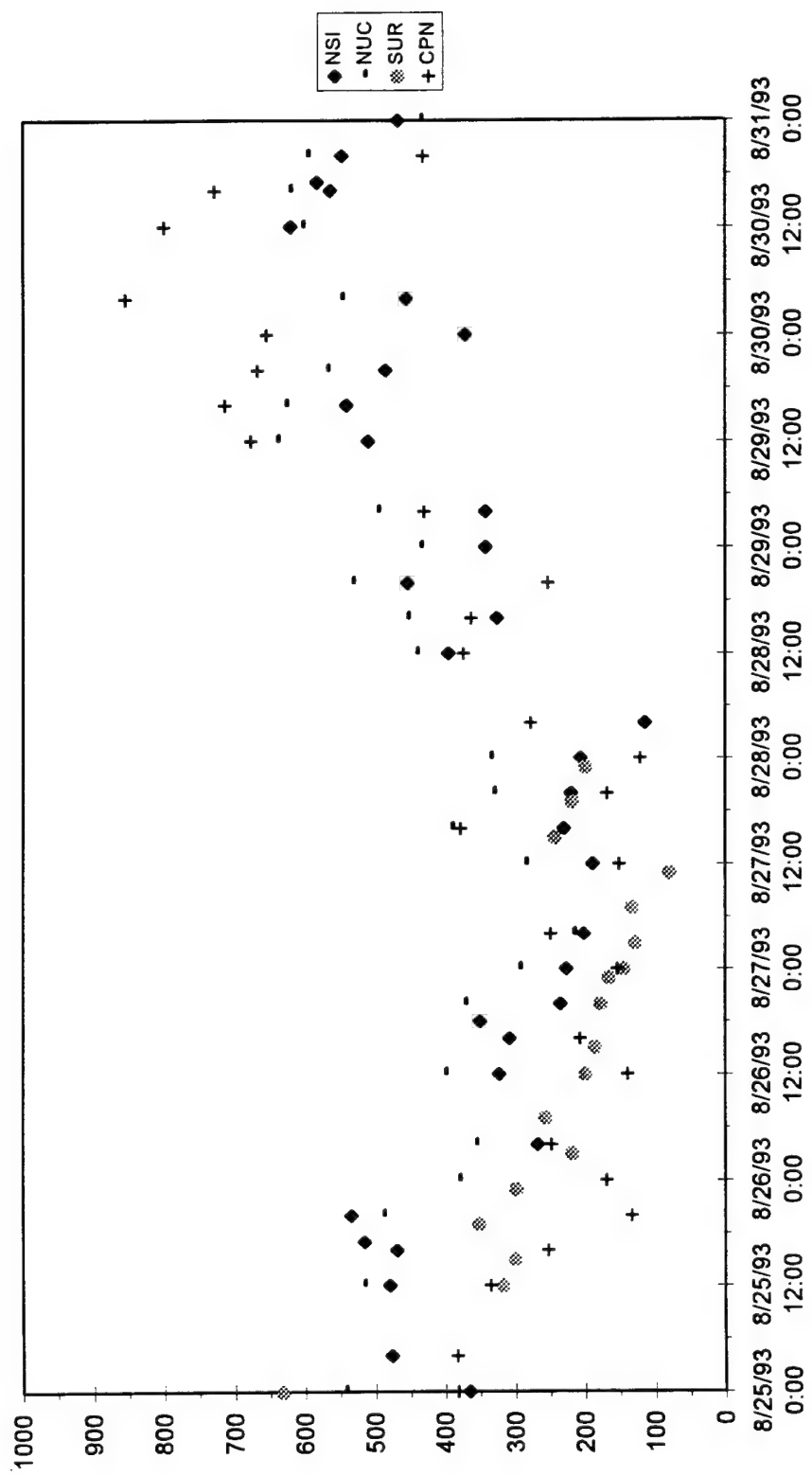


Figure 4.21 Time/Height plot of the observed trapping layer base at: San Nicolas Island (NSI), San Clemente Island (NUC), Research Vessel Pt. Sur (SUR), and Camp Pendleton (CPN). Time is along the abscissa, height in meters MSL is along the ordinate.

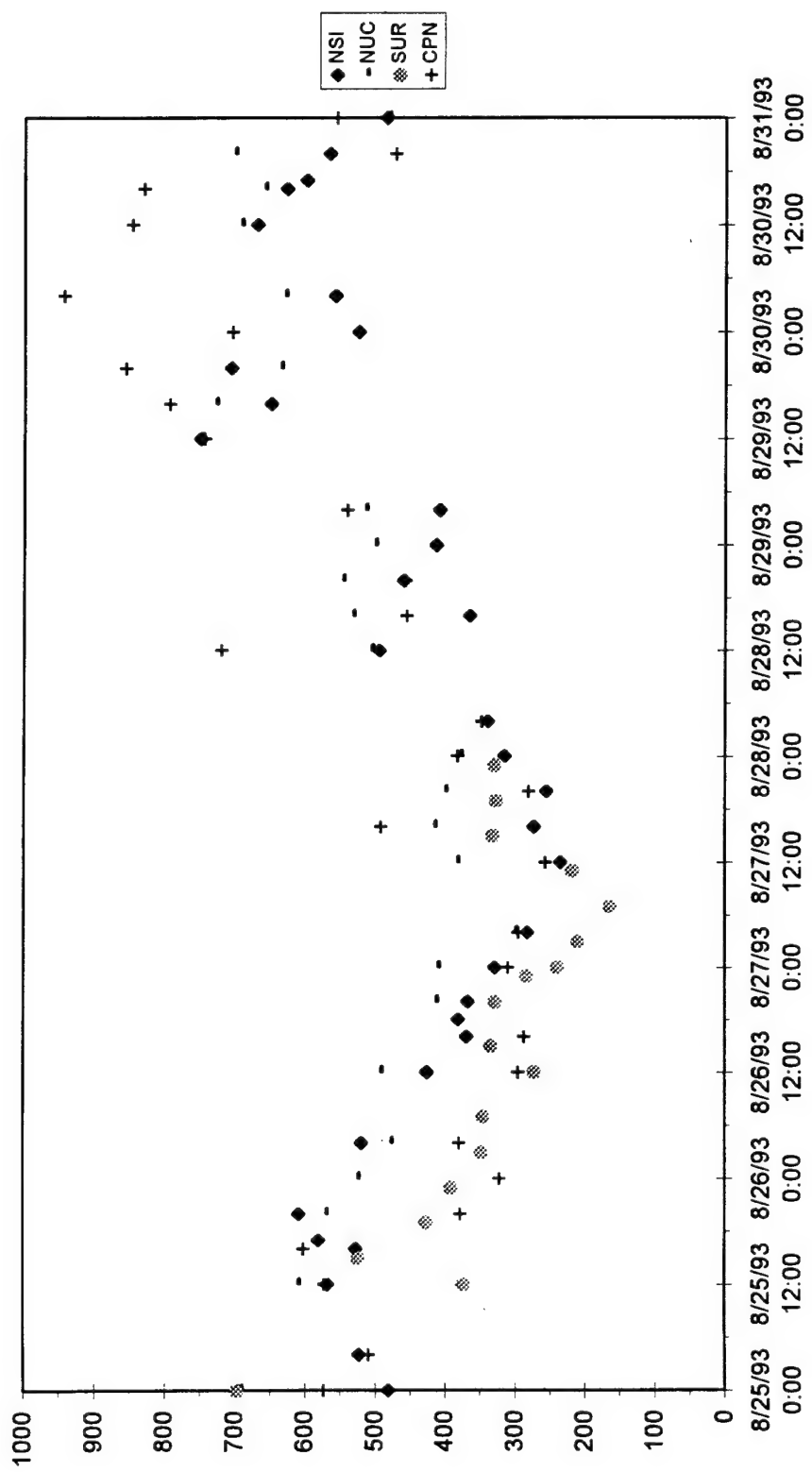


Figure 4.22 Time/Height plot of the observed trapping layer top at: San Nicolas Island (NSI), San Clemente Island (NUC), Research Vessel Pt. Sur (SUR), and Camp Pendleton (CPN). Time is along the abscissa, height in meters MSL is along the ordinate. Note, the trapping layer top is coincident with the top of the EM duct.

covers a broad area. This clearly suggests a synoptic scale origin, with the possibility for smaller amplitude mesoscale variability superimposed.

Chapter 5

EXPERIMENTAL RESULTS

This chapter presents the important findings from the MM5v1 simulations outlined in Chapter 3. The leading section will relate dominant synoptic scale forcing to the observed temporal trend in the MBL during the study period. Next, mesoscale influences on the MBL structure will be examined during a sub-period of the full seven-day simulation, including the effects of Tropical Storm Hilary. The final topic of this chapter is the presence of gravity waves and their implications for the modified refractivity field.

5.1 Synoptic Scale Results.

The MM5v1 108 km simulation developed realistic synoptic scale meteorological conditions during this study period due in part to the FDDA strategy outlined in Chapter 3. Recall that the purpose of the FDDA, applied to only the 108 and 36 km domains, is to improve the quality of the lateral boundary conditions for the 12 km domain, which is the focus of this study. Accurate 3-D synoptic scale dynamics are essential for producing realistic subsidence rates over the summertime eastern Pacific.

The 108 km simulated 500 mb GPH surface for 1200z, 27 August (Fig. 5.1) depicts the highest heights at 40°N and 135°W, with a central value of 5916 m (18 m lower than analyzed). This position is only two grid cells (216 km) west of the observed position of the high at this time (Fig. 4.2). Furthermore, the ridge axis extending through 54°N and 147°W closely matches the position of the observed ridge. At the end of the

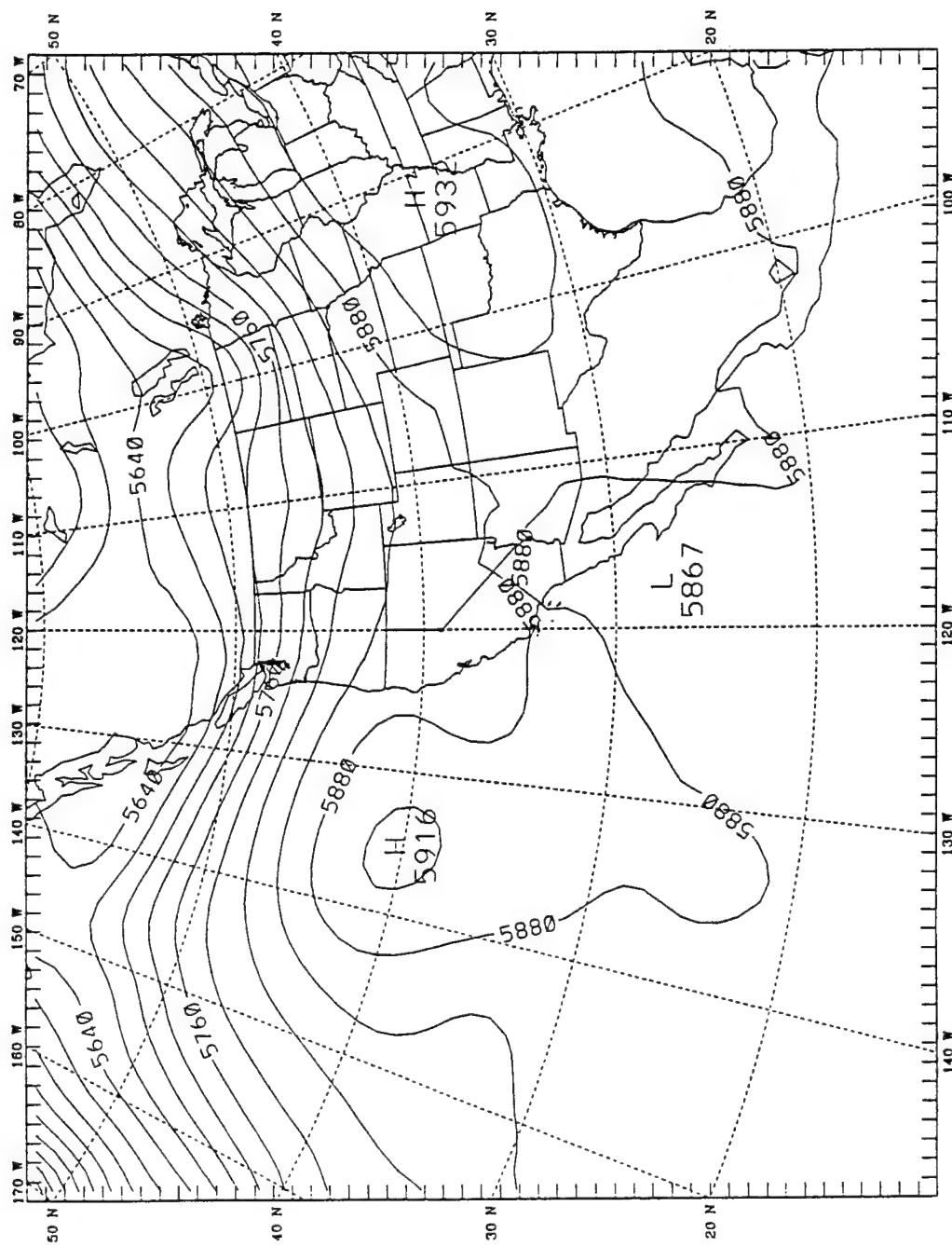


Figure 5.1 Simulated 500 mb GPH, 1200z, 27 August, 1993. The East Pacific Ridge axis extends to the northwest and southeast from the High at 133° W longitude.

seven-day simulation period, 1200z, 31 August, the 500 mb GPH pattern (Fig. 5.2) is again well correlated with the observed height field (Fig. 4.3). The positions of the 5938 m high in the north Pacific, the 5748 m offshore low near California, and the 5763 m low near 28°N and 141°W are in good agreement with the analysis, except that the intensity of the high and low centers in the model are less extreme by 8-17 m.

The temporal evolution in the 36 km simulated 500 mb GPH for three locations near the VOCAR area are shown daily at 1200z in Fig. 5.3. As for the observed height (Fig. 4.4), the model produces the highest heights from 27 to 28 August with rapidly falling heights near the end of the period for the northernmost points. The maximum error for these three points occurred at 40°N and 130°W on 27 August when the model underforecast the height by just 20 meters. The correlation coefficients between the simulated and analyzed heights for these points (from northwest to southeast) are 0.977, 0.996, and 0.952 respectively. Similar results were obtained for the synoptic scale sea level pressure field as well (not shown).

Since the 500 mb GPH heights are highest in the central period of the simulation, this period should also include the time when subsidence rates are the strongest. Recall that increased atmospheric subsidence should affect the MBL by suppressing the MBL height. As a means of investigating the long term evolution in subsidence, VOCAR area vertical velocity profiles from the 12 km mesh were examined. To help isolate the synoptic-scale component, the 0000z and 1200z vertical velocity profiles were spatially averaged over a 10 x 10 grid cell area (14,400 km²) centered over San Nicolas Island (Fig. 5.4). After spatially averaging on each model level, a three hour temporal average (e.g.

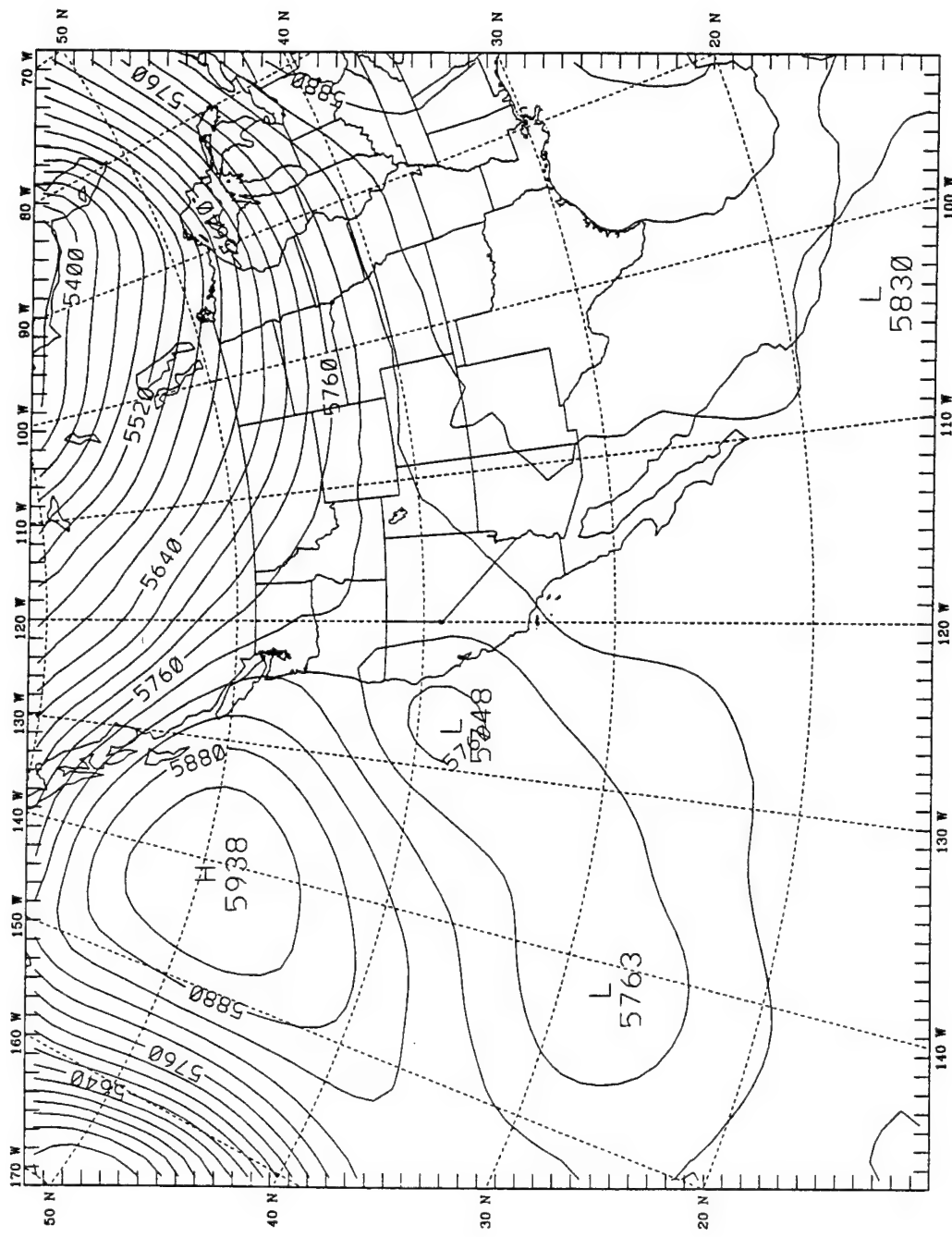


Figure 5.2 Simulated 500 mb GPH, 1200z, 31 August, 1993. The East Pacific Ridge has weakened and the High has moved to the northwest. A belt of lower heights extends from northern California to Hawaii.

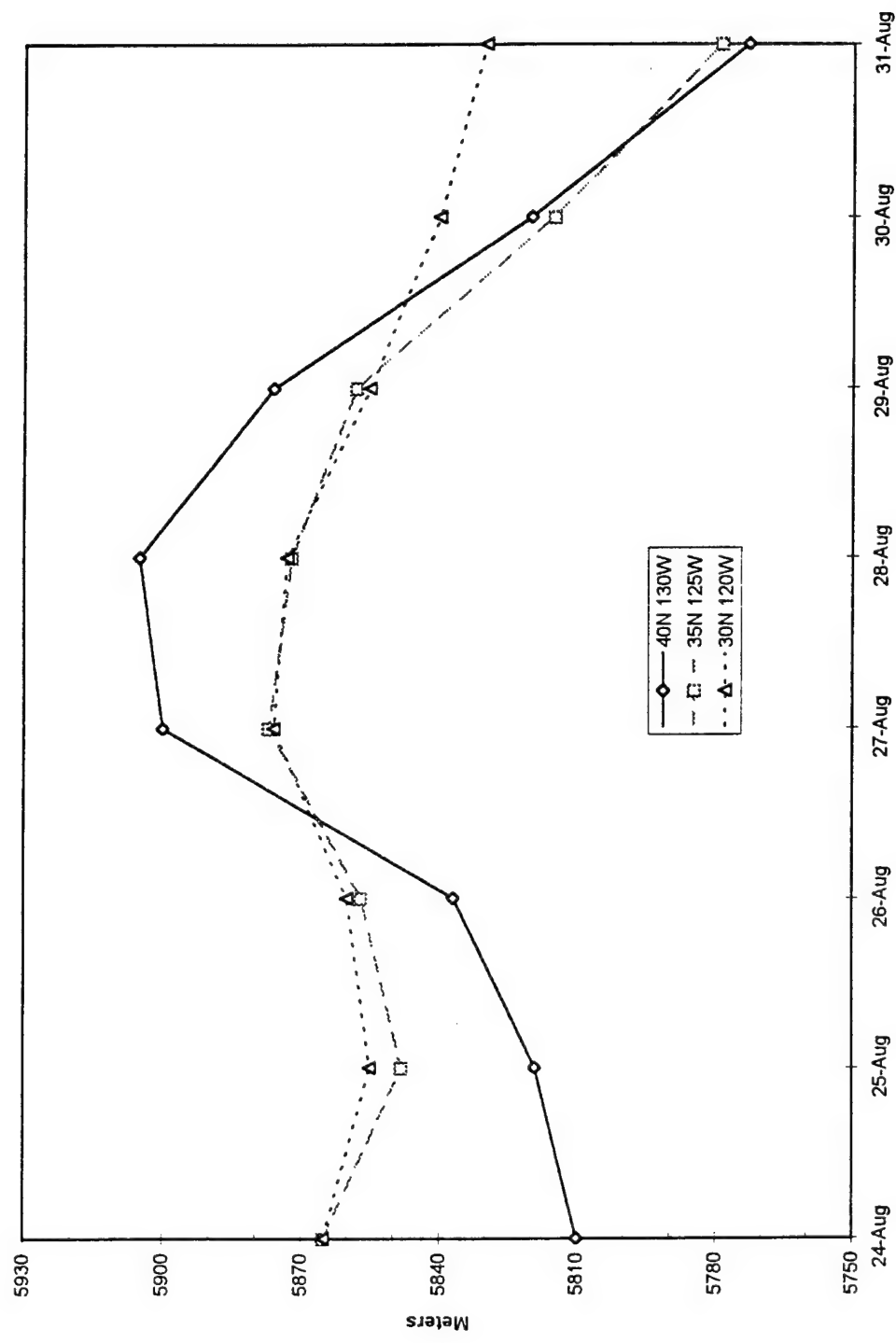


Figure 5.3 Time series of simulated 500 mb GPH for the same locations in Fig. 4.4. The model has captured the synoptic scale trend in 500 mb GPH with a maximum error of only 20 m.

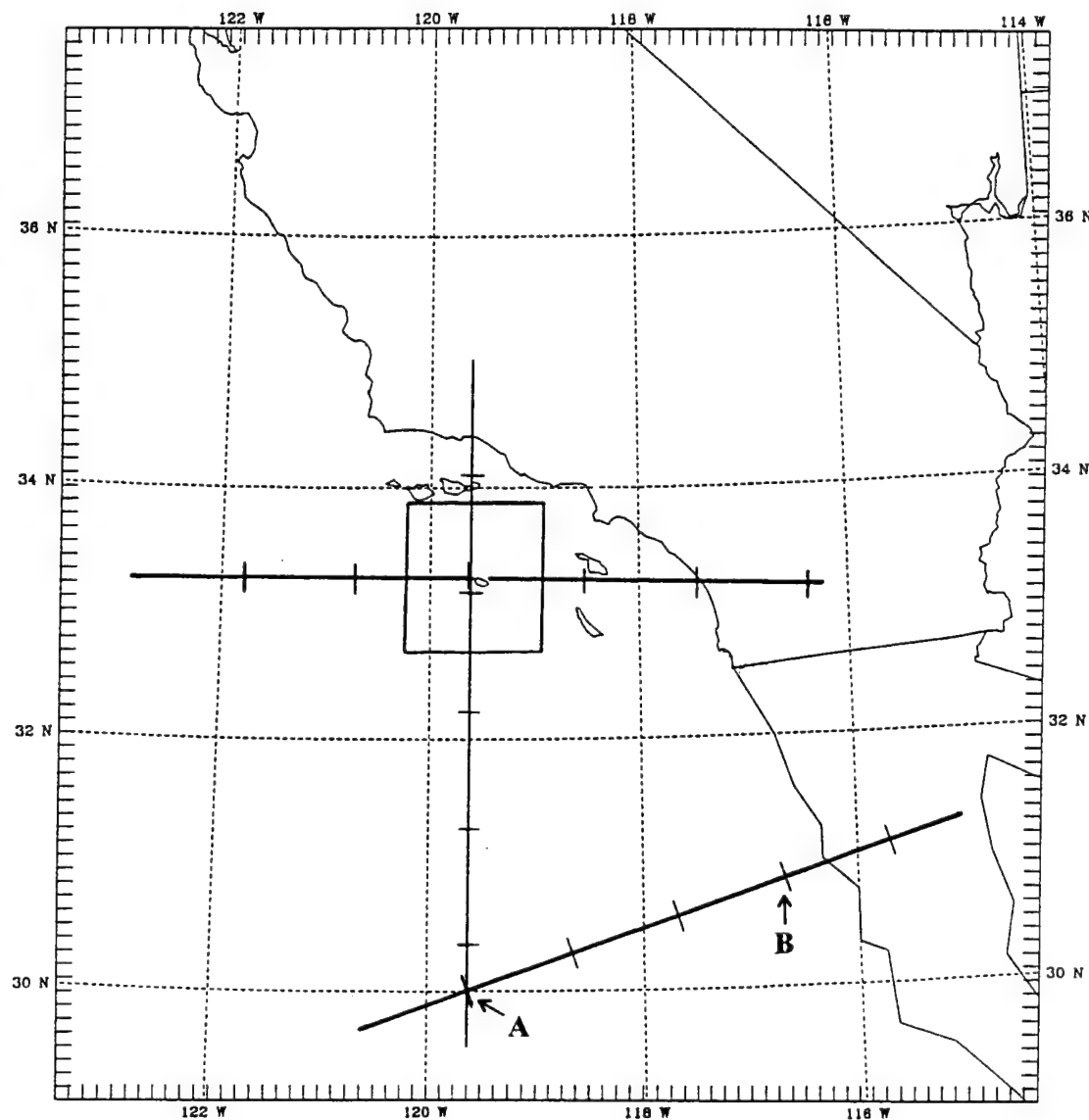


Figure 5.4 Location of cross-sections used in Chapter 5. Tick marks are hundreds of kilometers from the north, west, or southwest end of the respective cross-sections. The box delineates the area over which the vertical velocities were averaged for the profiles in Figs. 5.6-5.8.

1100z, 1200z, and 1300z) was performed to help remove high-frequency (transient) effects such as vertical velocity perturbations induced by gravity wave propagation. An instantaneous (unaveraged) vertical velocity profile for the lowest 6000 m over San Nicolas Island is shown with its accompanying smoothed (averaged) profile for 0000z, 28 August (Fig. 5.5). Note the smoother nature and broader peaks of the averaged versus the unaveraged profile. Using the averaged vertical velocity profiles, the long term subsidence trend can be established using the daily 0000z and 1200z profiles (Figs. 5.6-5.8). In general, both curves become progressively more negative over the first three days, marking a period of increased subsidence in the model that coincides with the amplification of the 500 mb ridge over the area. The subsidence then weakens during the latter portion of the period when the ridge shifts northward and 500 mb heights are falling. The temporal evolution in subsidence below 2 km in the model is consistent with the change in height of the observed EM trapping layer and duct for the same time period at San Nicolas Island (Fig. 4.16).

A strong link connecting the evolution of synoptic-scale 500 mb GPH to the EM trapping layer height is demonstrated in Figs. 5.9a and 5.9b, which shows the observed and simulated vertical motion of the trapping layer (i.e., the movement of the layer itself) at San Nicolas Island, along with the simulated vertical velocity (i.e., vertical component of the wind) at the midpoint of the trapping layer. The raw data shown in Fig. 5.9a are difficult to interpret, so they were filtered using a fast Fourier transform that removed frequencies less than 16 hours, resulting in the smoother graph (Fig. 5.9b). The simulated vertical motion of the layer is well correlated with the observed vertical motion in both

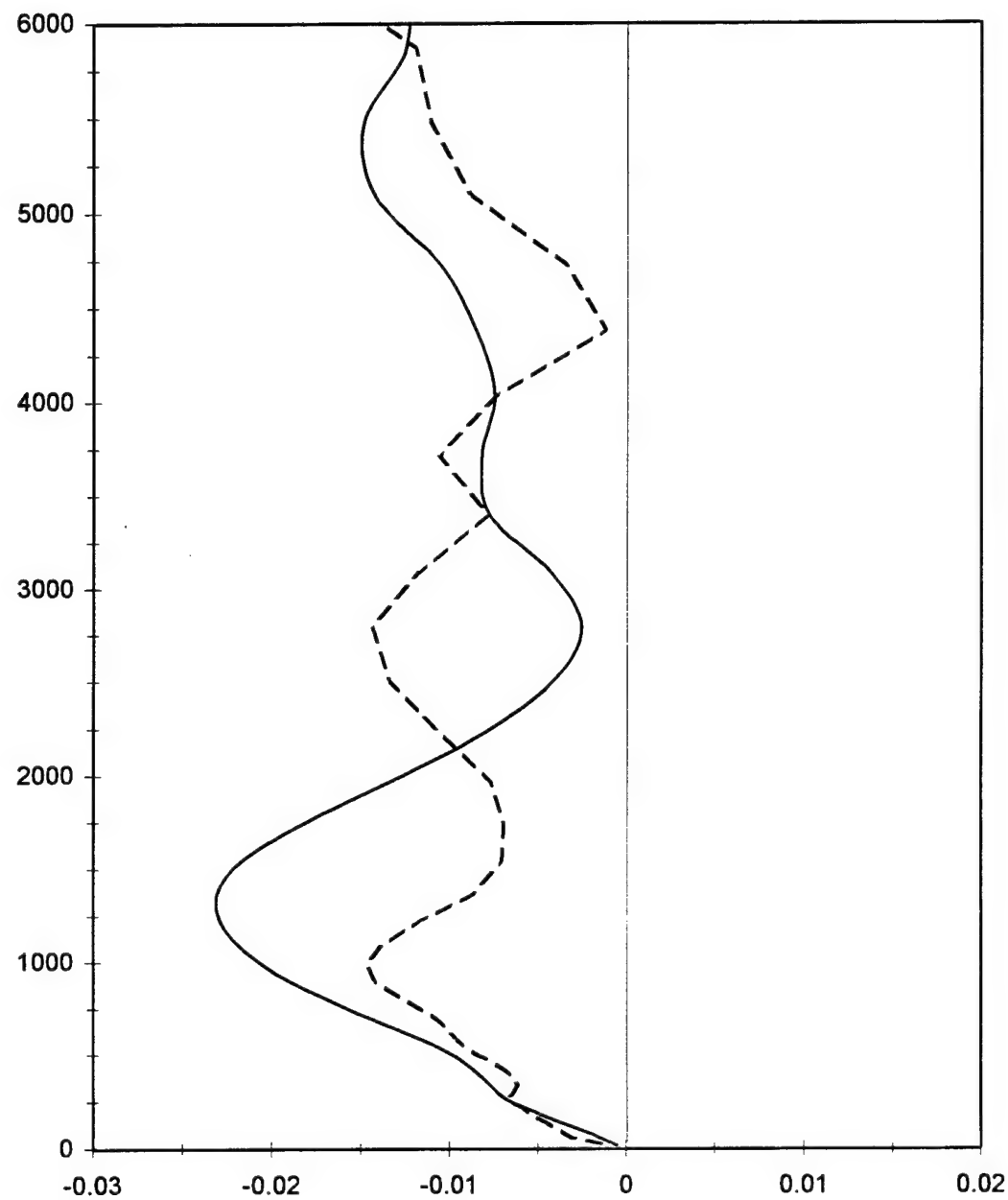


Figure 5.5 San Nicolas Island vertical velocity profiles for 28 August, 0000z. The unaveraged profile is the dashed line while the spatially and temporally averaged profile is the solid line. Vertical velocity ($m s^{-1}$) is plotted on the abscissa and height MSL (m) is plotted on the ordinate.

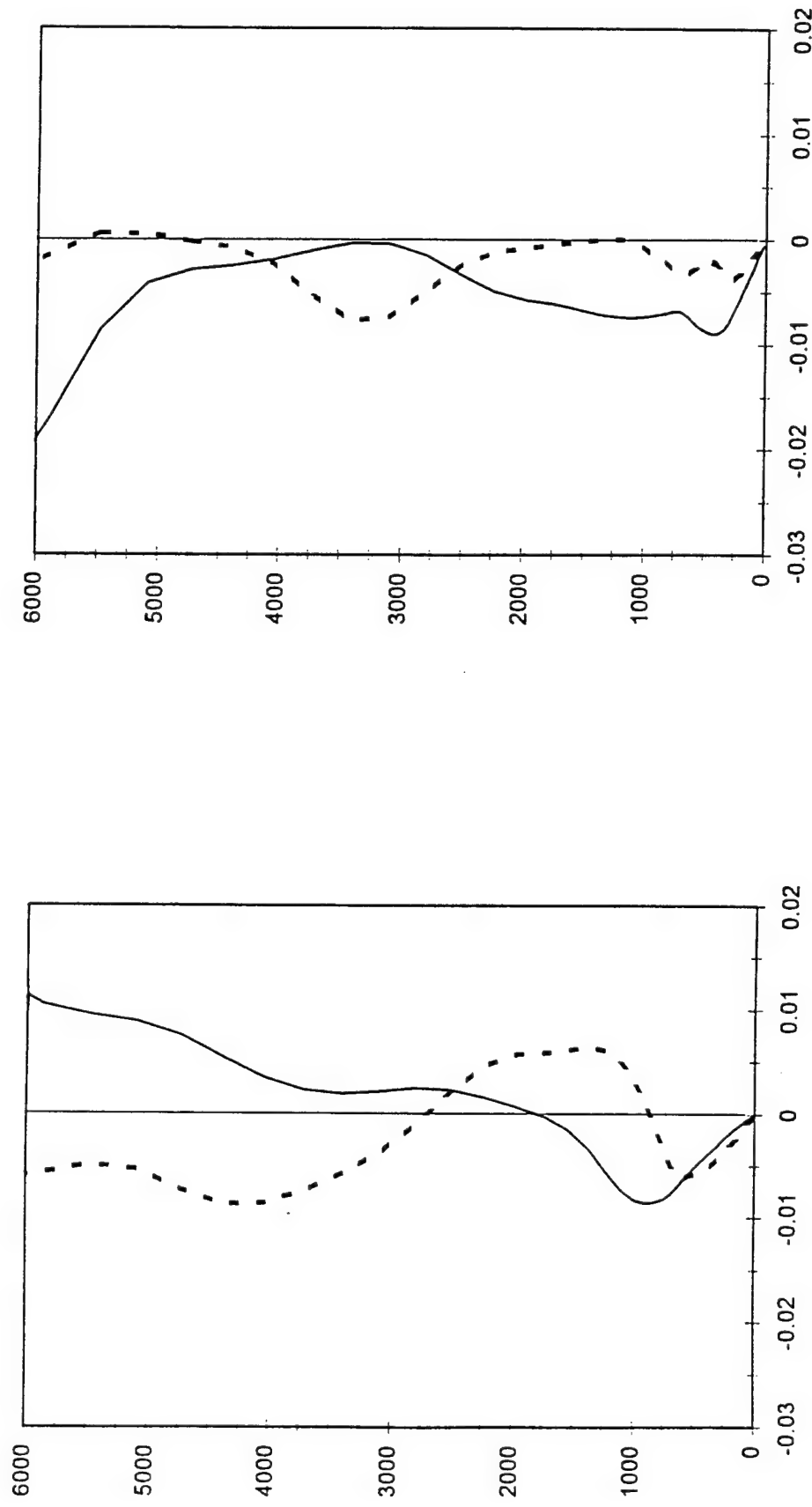


Figure 5.6 Averaged vertical velocity profiles at San Nicolas Island. The left hand graph is for 25 August 1993. The right hand graph is for 26 August 1993. The solid line is 0000z and the dashed line is 1200z. Vertical velocity (m s^{-1}) is plotted on the abscissa and height MSL (m) is plotted on the ordinate.

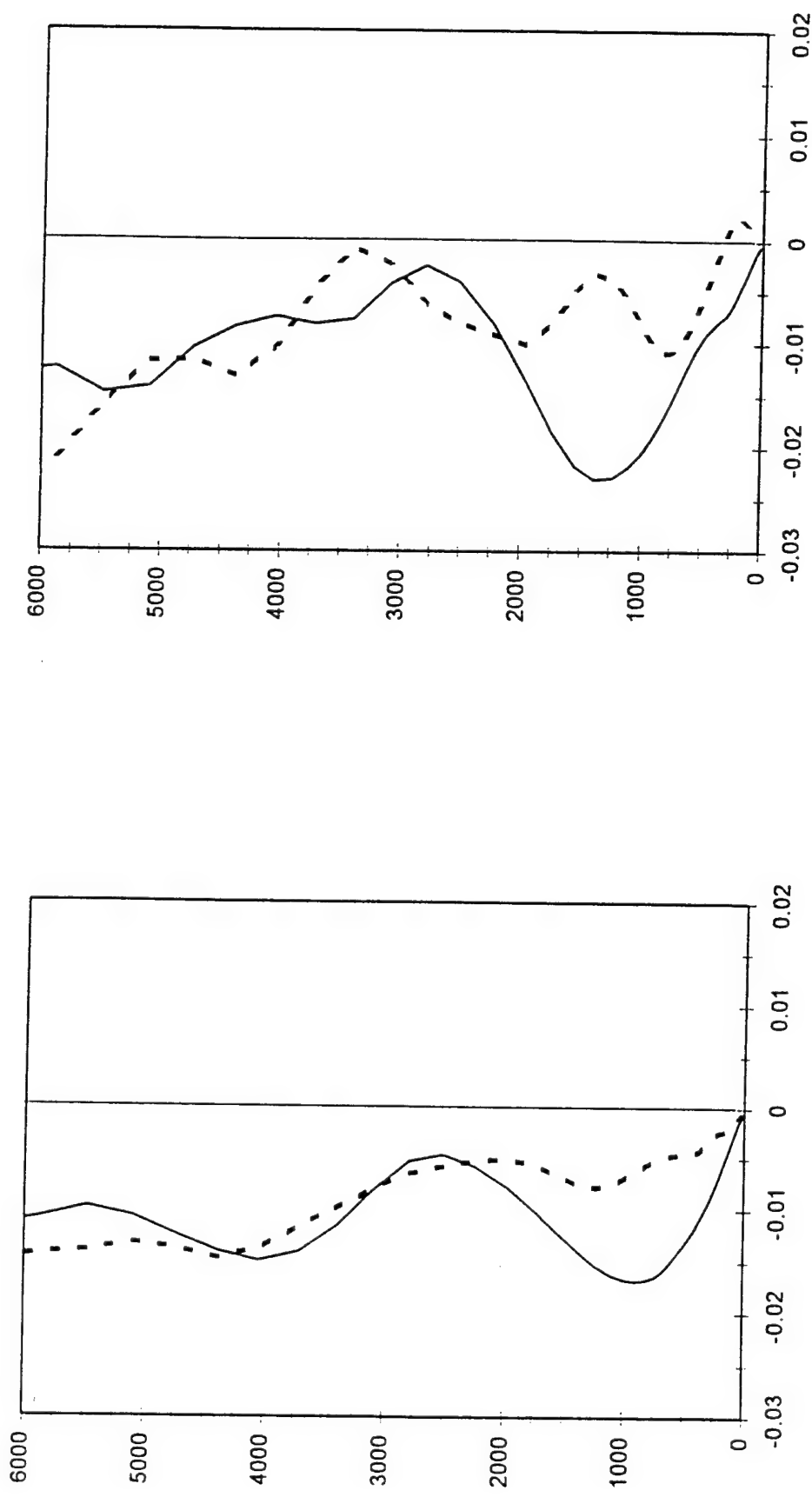


Figure 5.7 Averaged vertical velocity profiles at San Nicolas Island. The left hand graph is for 27 August 1993. The right hand graph is for 28 August 1993. The solid line is 0000z and the dashed line is 1200z. Vertical velocity (m s^{-1}) is plotted on the abscissa and height MSL (m) is plotted on the ordinate.

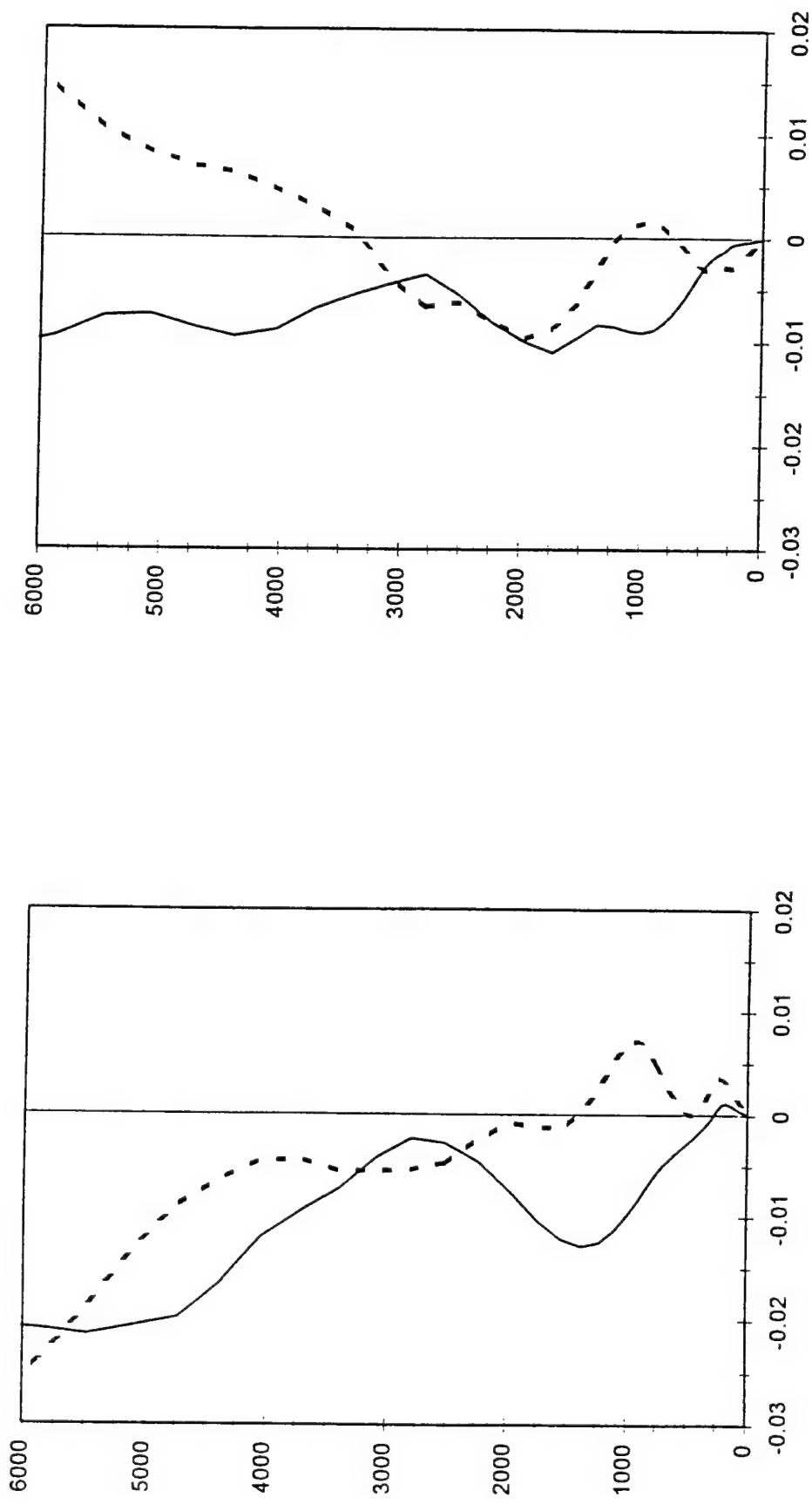


Figure 5.8 Averaged vertical velocity profiles at San Nicolas Island. The left hand graph is for 29 August 1993. The right hand graph is for 30 August 1993. The solid line is 0000z and the dashed line is 1200z. Vertical velocity (m s^{-1}) is plotted on the abscissa and height MSL (m) is plotted on the ordinate.

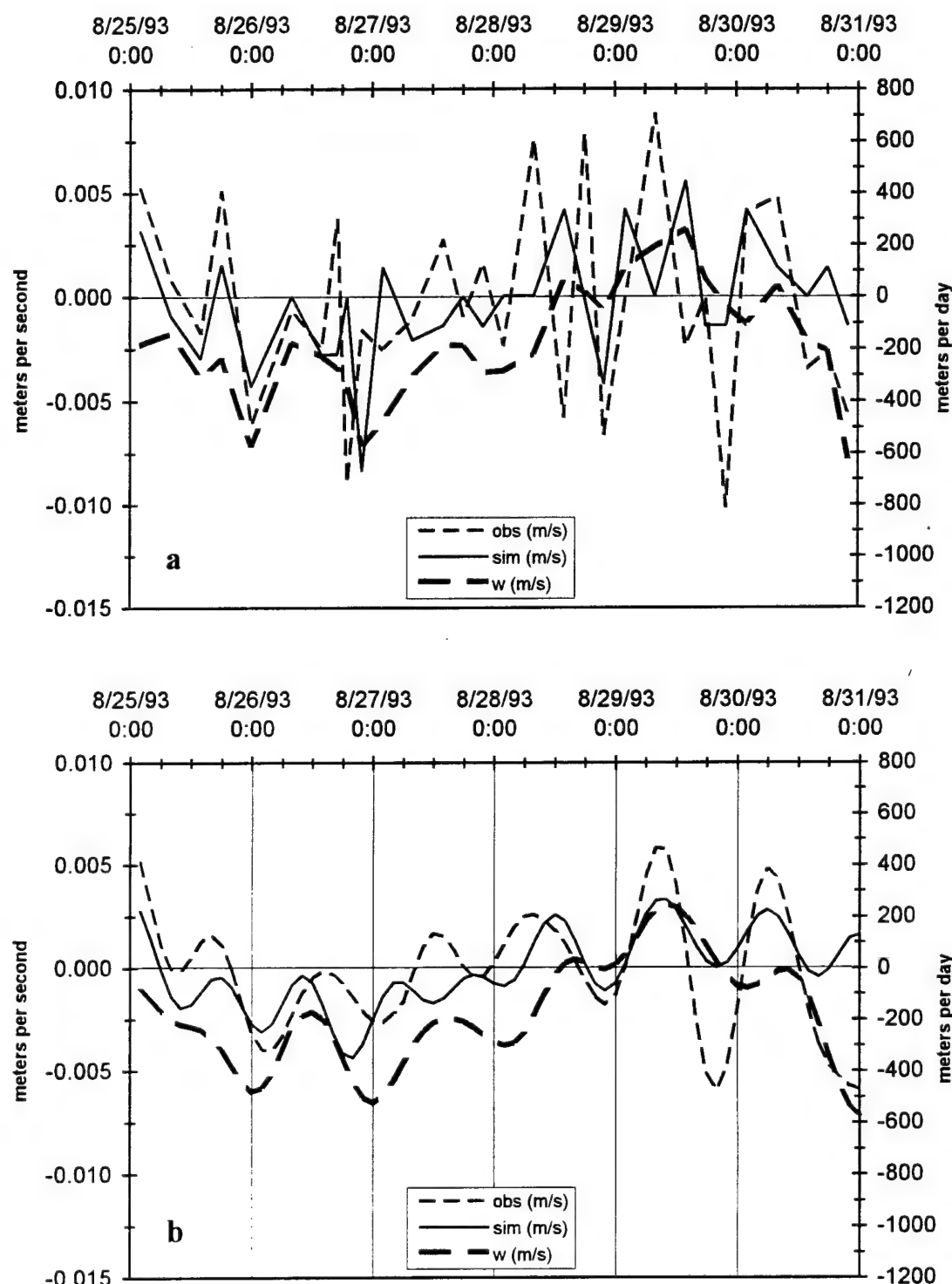


Figure 5.9 (a) Vertical motion of the observed trapping layer, simulated trapping layer, and simulated vertical velocity at the mid-point of the simulated trapping layer at San Nicolas Island. (b) Fourier representation filtering out temporal variations less than 16 hours in scale.

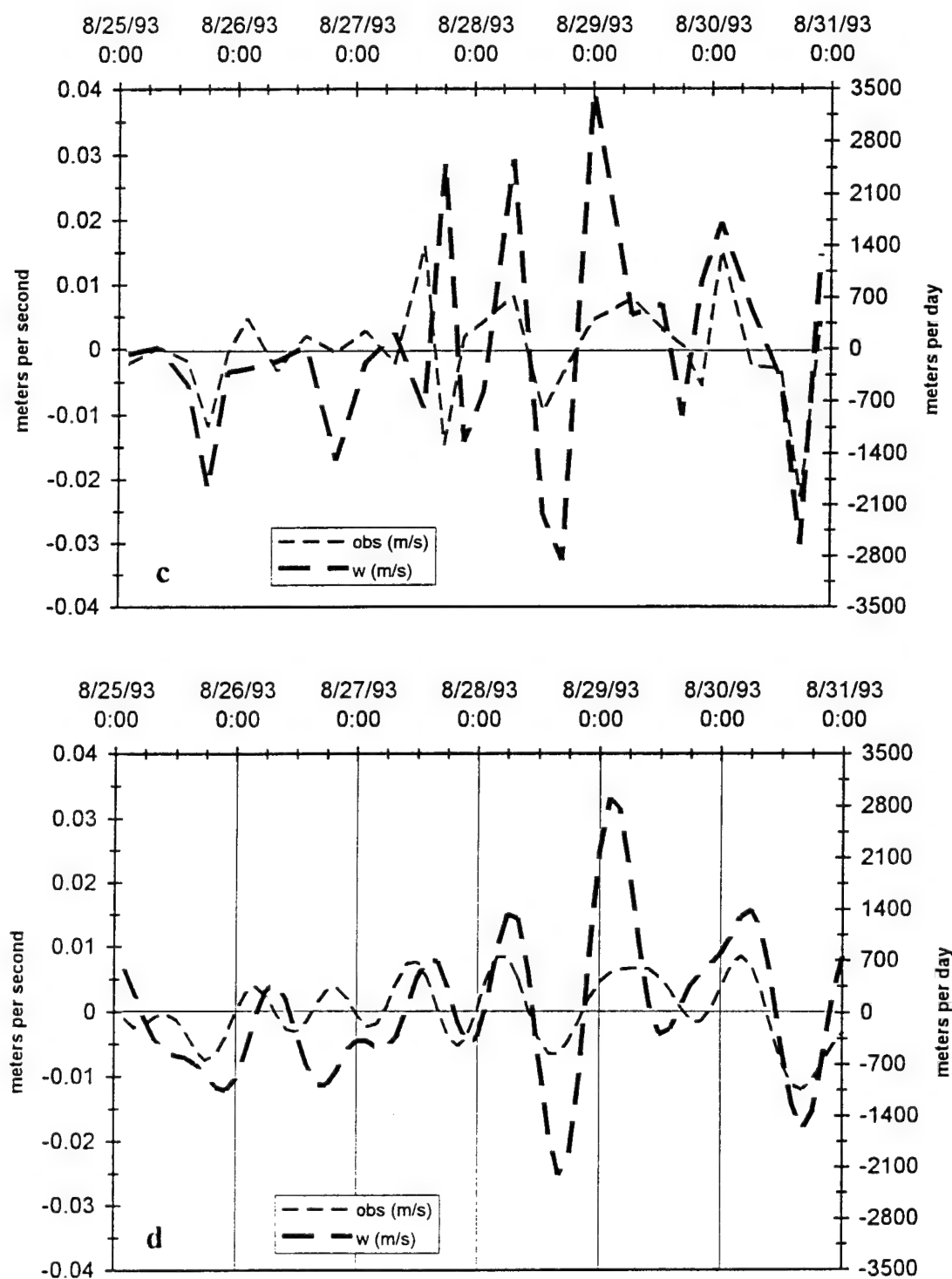


Figure 5.9 (c) Vertical motion of the observed trapping layer and simulated vertical velocity at the mid-point of the observed trapping layer at Camp Pendleton. (d) Fourier representation filtering out temporal variations less than 16 hours in scale.

magnitude and phase. The synoptic scale temporal variation (period of about six days) is clearly present as well as an embedded diurnal signal. Finally, note the simulated vertical velocity (heavy dashed lines) does not match the total vertical motion of the trapping layer (thin solid and dashed lines), especially during the first four days. This difference is due to the effects of other physical processes like surface fluxes, mixing within the MBL, and entrainment at the MBL top. The same long term trend and diurnal signal are evident at Camp Pendleton (Figs. 5.9c and 5.9d), but the magnitude of vertical motion is greater. Camp Pendleton's location at the shore places it in the region of maximum horizontal acceleration associated with the sea breeze. The simulated vertical motion of the trapping layer is not shown in Figs. 5.9c and 5.9d because the observed ducting structure was poorly represented by the model at Camp Pendleton (discussed below).

The previous discussion established synoptic scale ridging and associated subsidence as a major influence on the temporal evolution of the MBL depth in the VOCAR area. Recall from Figs. 4.16-4.19, that the long term variation in the observed EM trapping and ducting layers consisted of lowering during the first two days, followed by rising of these layers on 28-30 August. The MM5 simulated trapping and ducting layers for three VOCAR sites are shown in Figs. 5.10-5.12. Figure 5.10, San Nicolas Island, demonstrates the model's skill in producing the observed long term variation with the lowest trapping and ducting layers from 27 Aug 1200z to 28 Aug 1200z. While the model did not raise the trapping layer as rapidly as the observations indicate, it does capture the temporal variability well. This same ability to follow the observed temporal

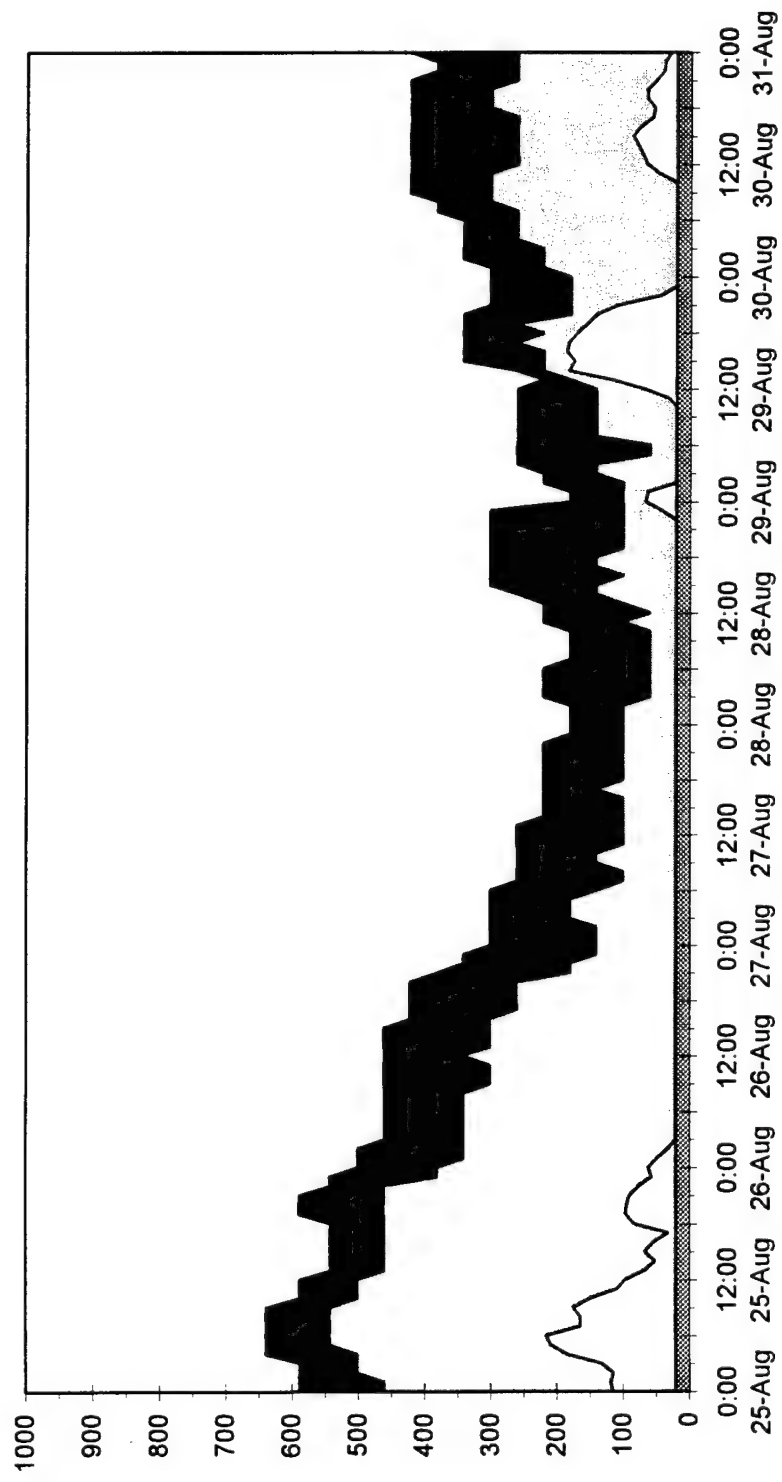


Figure 5.10 Simulated refractive structure at San Nicolas Island during the case period. Time is along the abscissa, height in meters MSL is along the ordinate. Dark shading represents the trapping layer. The ducting layer extends from the trapping layer top to the bottom edge of the light shaded region.

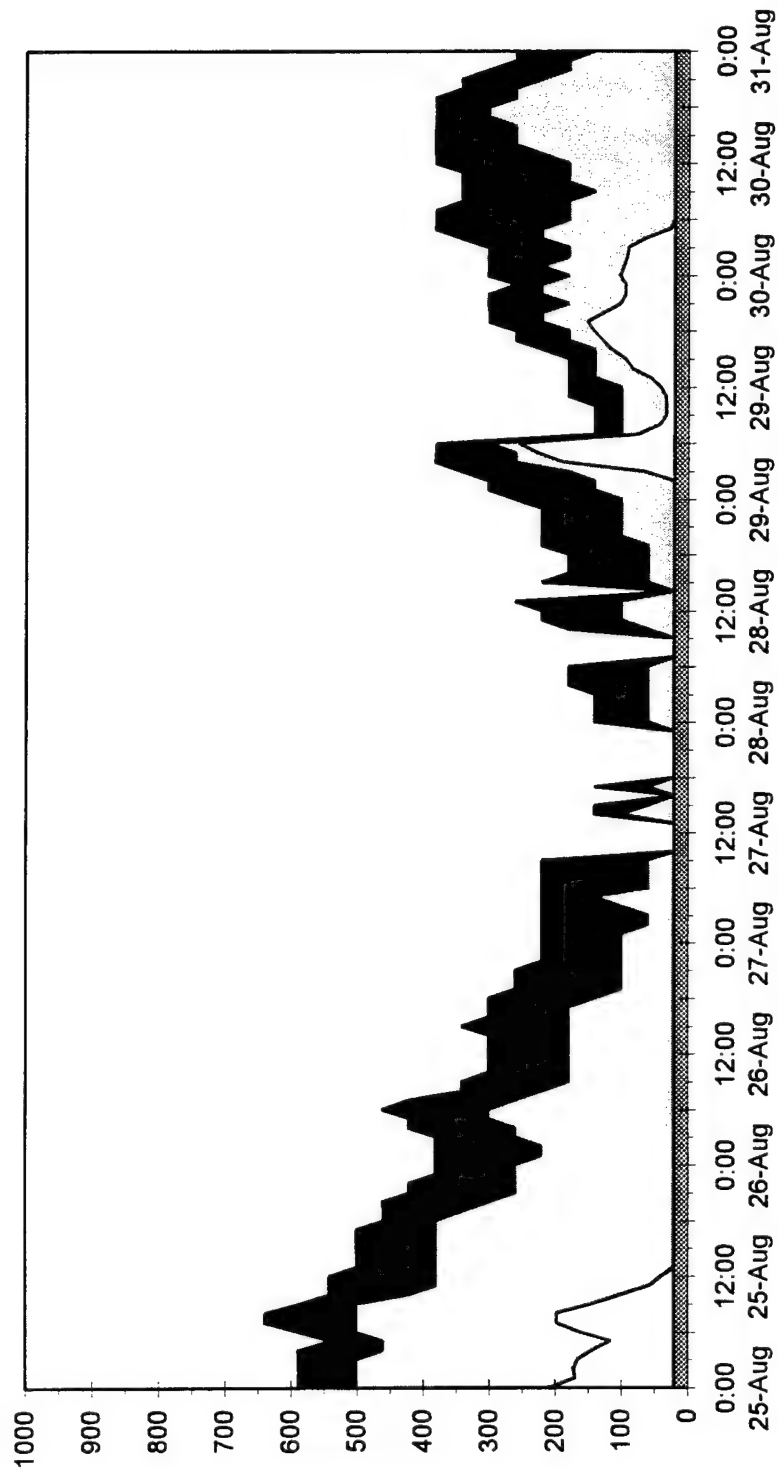


Figure 5.11 Simulated refractive structure at San Clemente Island during the case period. Time is along the abscissa, height in meters MSL is along the ordinate. Dark shading represents the trapping layer. The ducting layer extends from the trapping layer top to the bottom edge of the light shaded region.

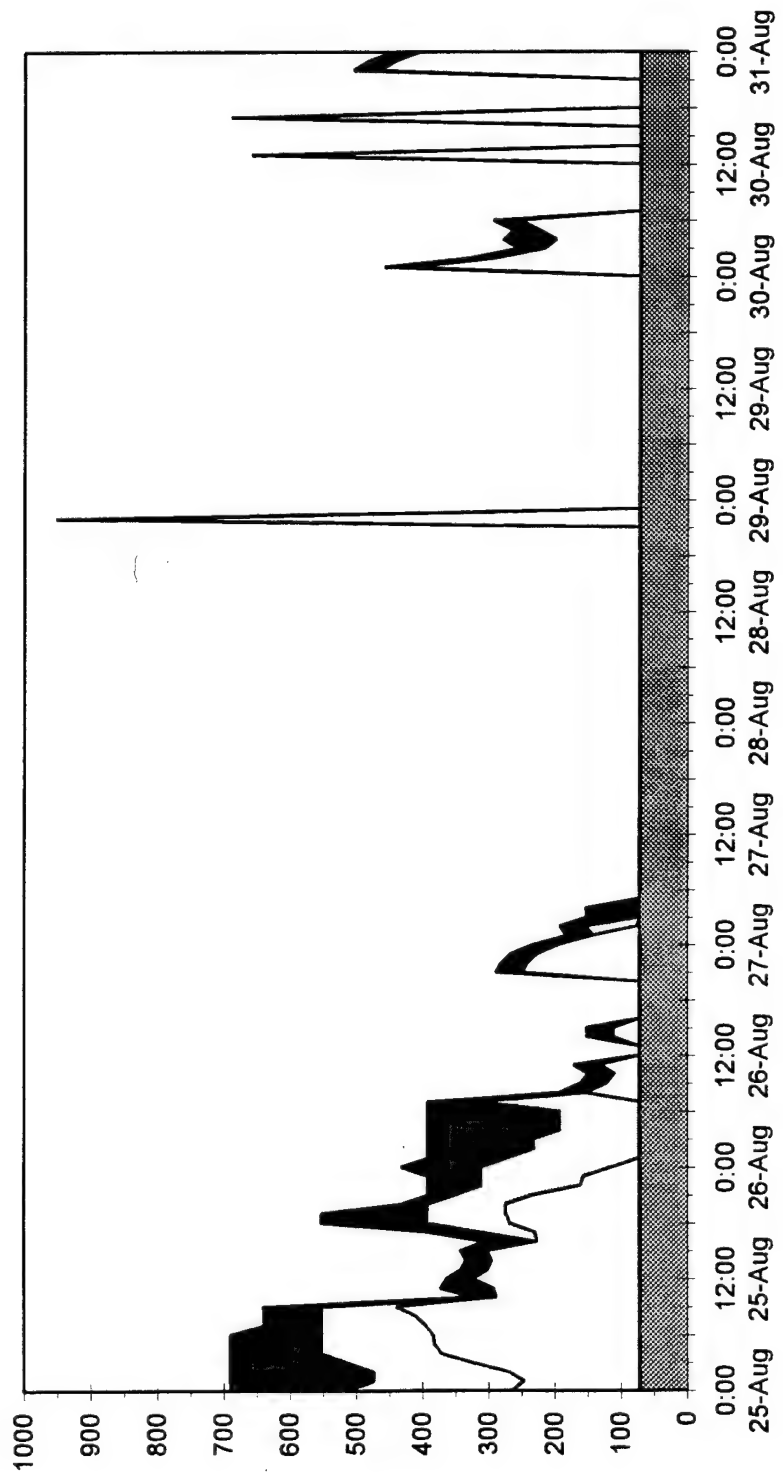


Figure 5.12 Simulated refractive structure at Camp Pendleton during the case period. Time is along the abscissa, height in meters MSL is along the ordinate. Dark shading represents the trapping layer. The ducting layer extends from the trapping layer top to the bottom edge of the light shaded region.

trend is repeated at San Clemente Island, about 80 km from shore (compare Figs. 4.17 and Fig. 5.11). At Camp Pendleton, however, the model depicts ducting properties only during the first two days and there are large differences from the observed ducting structure (compare Figs. 4.19 and Fig. 5.12). Camp Pendleton is a coastal land point, whereas San Nicolas and San Clemente Islands are far from shore ($6-9 \Delta x$). The reason for the substantially poorer representation of the trapping and ducting characteristics at Camp Pendleton, compared to San Nicolas and San Clemente Islands, is not entirely clear. It is known that the marine layer became very thin in the model solutions at Camp Pendleton around the middle of the period and even disappeared completely at times. The cause of this error are a subject for future investigation.

5.2 Mesoscale Results (25 August, 1200z - 27 August, 1200z).

The preceding section presented important results linking the six day temporal variation in MBL depth and refractive structure to changes in the synoptic-scale forcing. Mesoscale circulations and diurnal variations superimposed on this longer term synoptic trend also lead to spatial and temporal variability in the MBL height, EM trapping, and EM ducting layers. This section presents findings revealing the mesoscale effects.

In addition to the long term variation, Figures 5.6-5.8 also reveal a probable mesoscale influence which produces a subsidence maximum near 1.0-2.0 km MSL around 0000z on most days. This diurnal cycle is repeated in Figs. 5.9b and 5.9d and is likely to be associated with the heating and cooling cycle over land. The resulting sea breeze circulation is strongest near or just before 0000z, which implies that the return branch of

the circulation is strongest at that time, including a subsiding region extending out to roughly 150 km offshore. Thus, San Nicolas Island, located about 100 km from the mainland, lies in a region expected to experience subsidence during the afternoons when the mesoscale sea breeze regime is evident. In this case, the mesoscale forcing reinforces the synoptic-scale forcing to generate maximum sinking in the VOCAR area during the afternoons. As shown in Fig. 5.9, the enhanced subsidence has a direct impact on the MBL depth and the height of the trapping layer.

The diurnal (sea breeze) influence is not the only mesoscale effect detected in the MM5 12 km solution. The approach of a tropical storm from the south caused a disruption of the normal (climatological) summer regime in the VOCAR area, producing mesoscale advection patterns that significantly altered the MBL, moisture, and refractivity structure. The Case Description in Chapter 4 provided an overview of Tropical Storm Hilary, its storm track (Fig. 4.8), and the 850 mb wind fields associated with the storm (Figs. 4.9-4.11). The simulated water vapor mixing ratio (q_v) fields confirmed that Tropical Storm Hilary forced a mid-level moisture intrusion into the VOCAR area (Figs. 4.12-4.15). A north to south cross-section of the MM5 12 km simulated q_v , vertical velocity, and wind vectors in the cross-sectional plane (see Fig. 5.4) for 25 August 1200z is shown in Fig. 5.13. The top of the MBL is marked by the strong q_v gradient from about 950-930 mb. A moist plume forced by daytime convection, extending up to 750 mb, appears on the southern side of the Santa Inez Mountains while the driest air (3-4 g/kg) is found at 900 mb north of 30°N. Also note that the moisture intrusion from Tropical Storm Hilary has already begun between 870-700 mb, caused by southeasterly

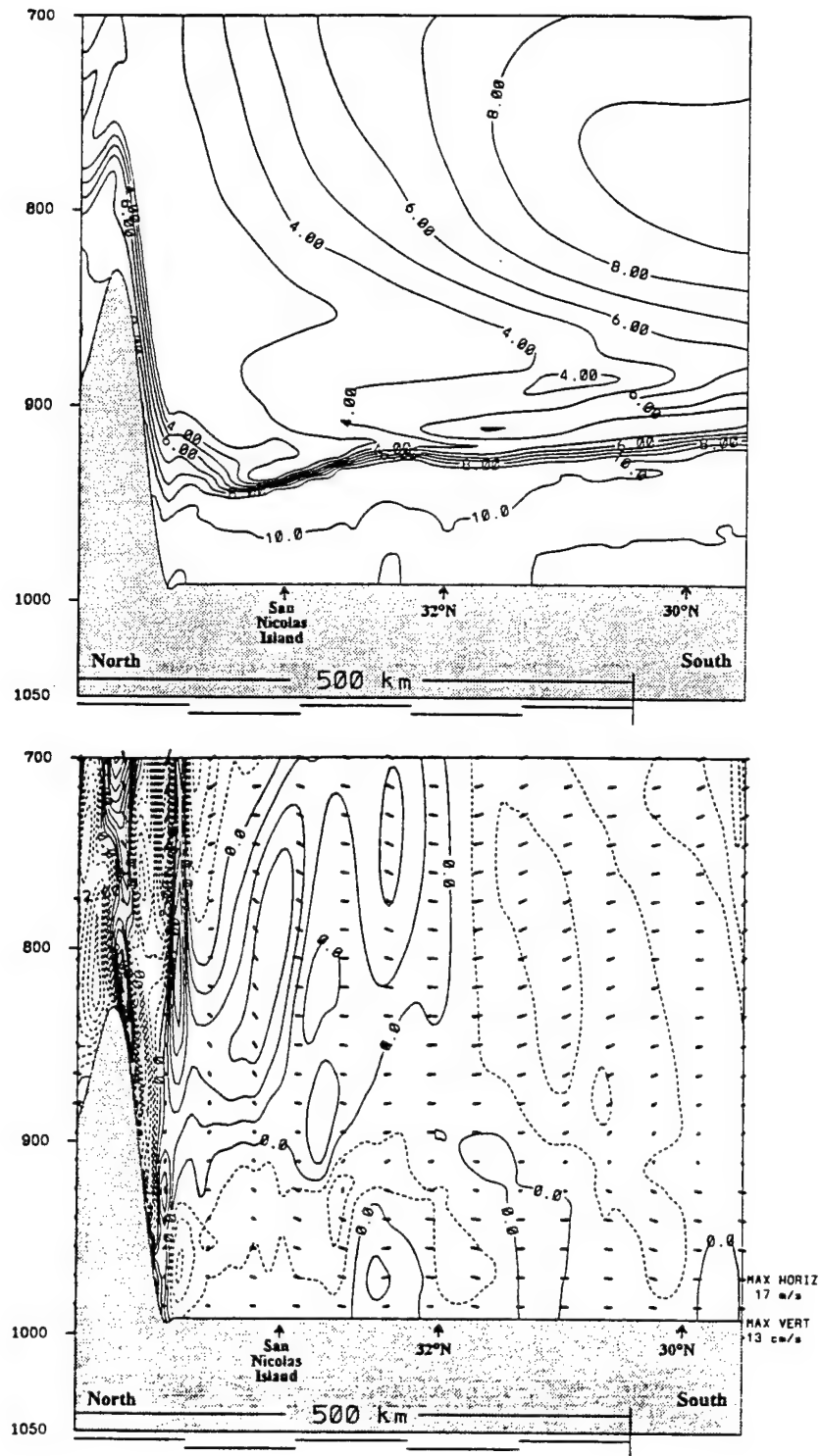


Figure 5.13 North to south cross-section (25 August, 1200z) of simulated water vapor mixing ratio (top, contour interval 1.0 g kg^{-1}), simulated vertical velocity (bottom, contour interval 0.5 cm s^{-1}), and wind vectors in the plane. Note: positive vertical velocities (solid), negative vertical velocities (dashed).

winds in that layer. By 26 August 1200z, mid-level moisture from Hilary has progressed northward to Santa Cruz Island and the MBL has lowered nearly 25 mb (220 m) across the region (Fig. 5.14). The southerly flow has strengthened and a broad area of subsidence now exists from San Nicolas Island to about 30°N. The tongue of dry air has elongated and subsided with the driest air (about 3 g/kg) at 940 mb over San Nicolas Island. Twenty-four hours later, 27 August 1200z, Hilary's moisture has progressed to the mountains and effectively ‘pinched off’ the dry air in a very thin layer at 975 mb over the VOCAR region (Fig. 5.15). Subsidence persists in the VOCAR region where the MBL has lowered another 25 mb and is only about 300 meters deep at San Nicolas Island.

This forty-eight hour trend of mid-level moistening and decreasing MBL depths was clearly depicted in the observed soundings at San Nicolas Island (see Figs. 4.12-4.15). Likewise, the model soundings for San Nicolas Island captured this trend, including the juxtaposition of the relatively cool, moist MBL air and the very thin overlying warm, dry layer (Figs. 5.16-5.18). In this series of simulated soundings, the steady subsidence and moistening in the mid-levels results in the dry ‘spike’ just above the inversion base, which has lowered and thinned over the two day period.

As discussed in Chapter 1, the presence of sharp vertical moisture gradients can lead to EM trapping and ducting conditions. Calculation of modified refractivity profiles from the meteorological variables (both observed and simulated) indicate that EM trapping and ducting layers were present at San Nicolas Island. On 25 August 1200z, an observed trapping layer of approximately 100 m resulted in an elevated duct nearly 350 m thick with a base near 200 m (Fig. 5.19). The simulated M-profile for the same time

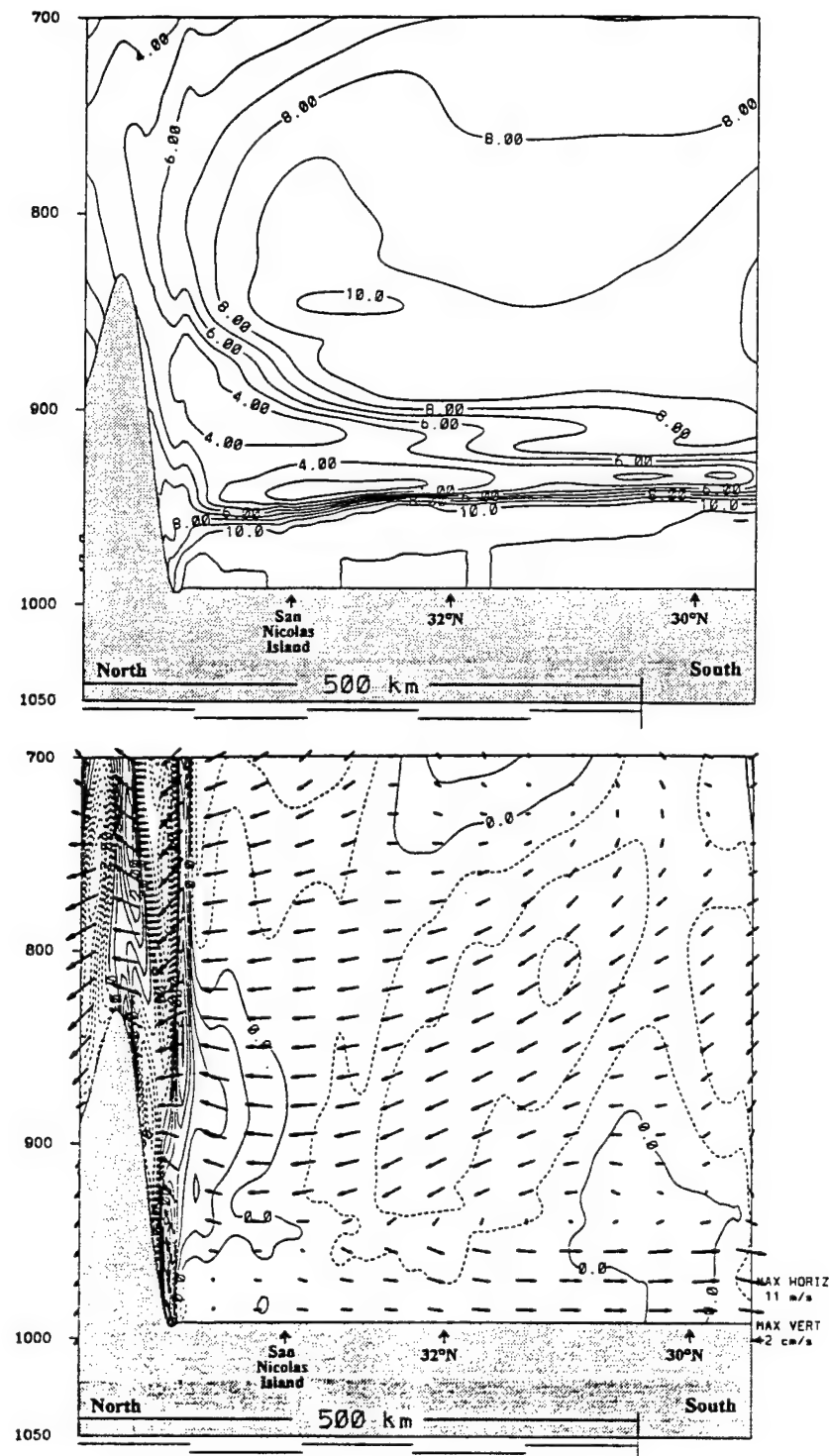


Figure 5.14 North to south cross-section (26 August, 1200z) of simulated water vapor mixing ratio (top, contour interval 1.0 g kg^{-1}), simulated vertical velocity (bottom, contour interval 0.5 cm s^{-1}), and wind vectors in the plane. Note: positive vertical velocities (solid), negative vertical velocities (dashed).

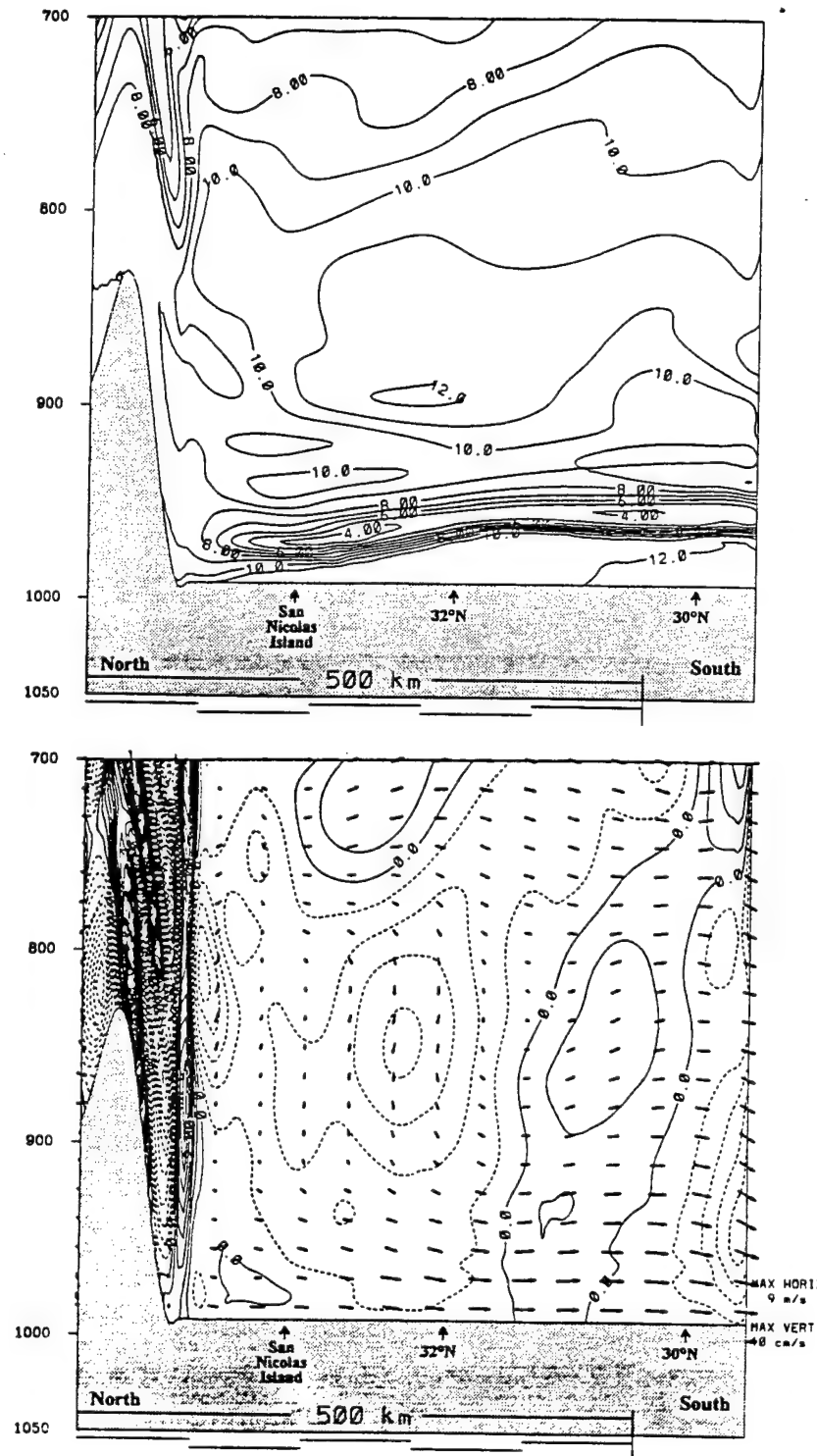


Figure 5.15 North to south cross-section (27 August, 1200z) of simulated water vapor mixing ratio (top, contour interval 1.0 g kg^{-1}), simulated vertical velocity (bottom, contour interval 0.5 cm s^{-1}), and wind vectors in the plane. Note: positive vertical velocities (solid), negative vertical velocities (dashed).

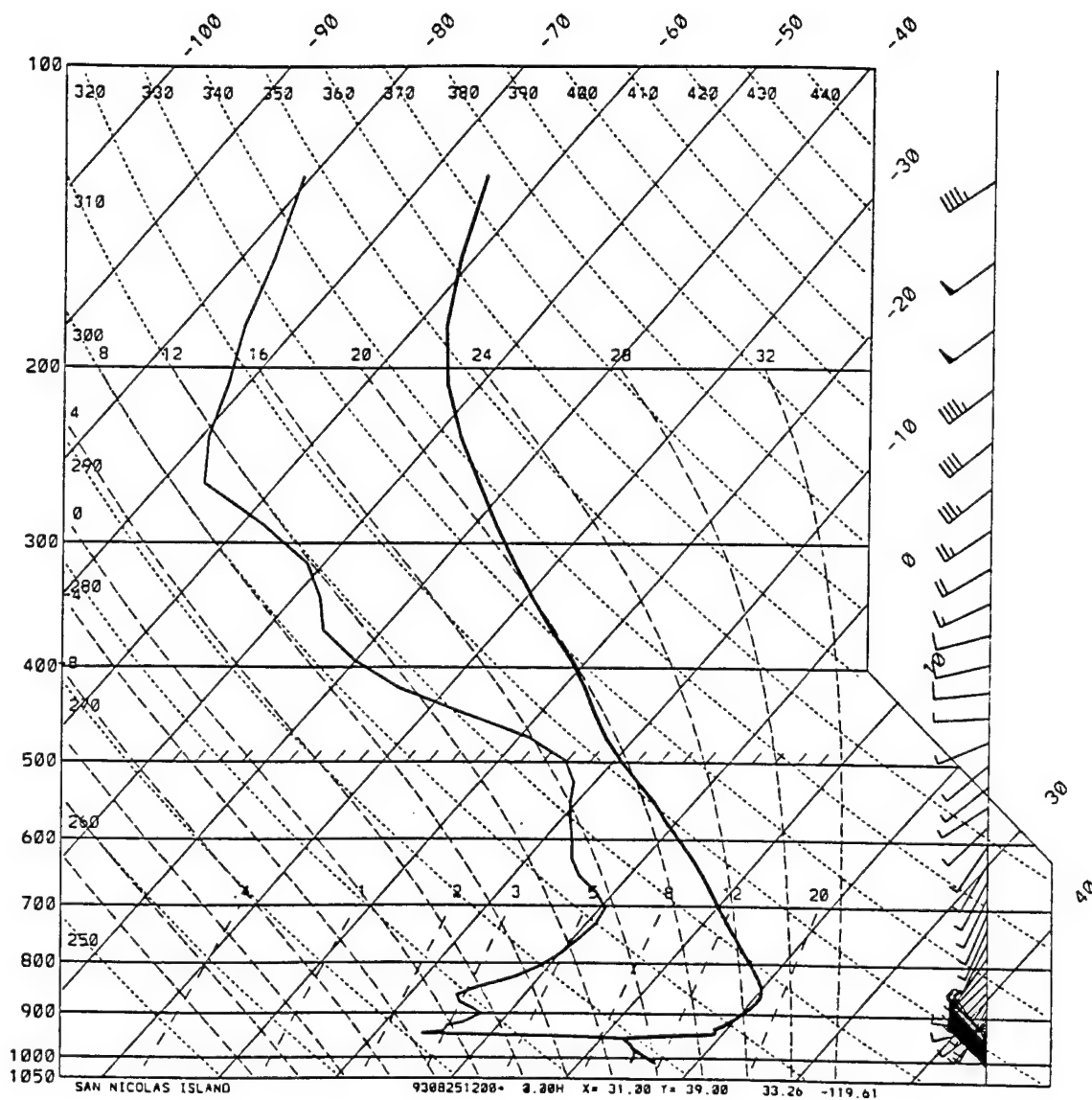


Figure 5.16 San Nicolas Island simulated Skew-T diagram, 1200z, 25 August, 1993. Note the MBL top is near 950 mb with low level northwesterly flow and southwesterly flow just above the MBL.

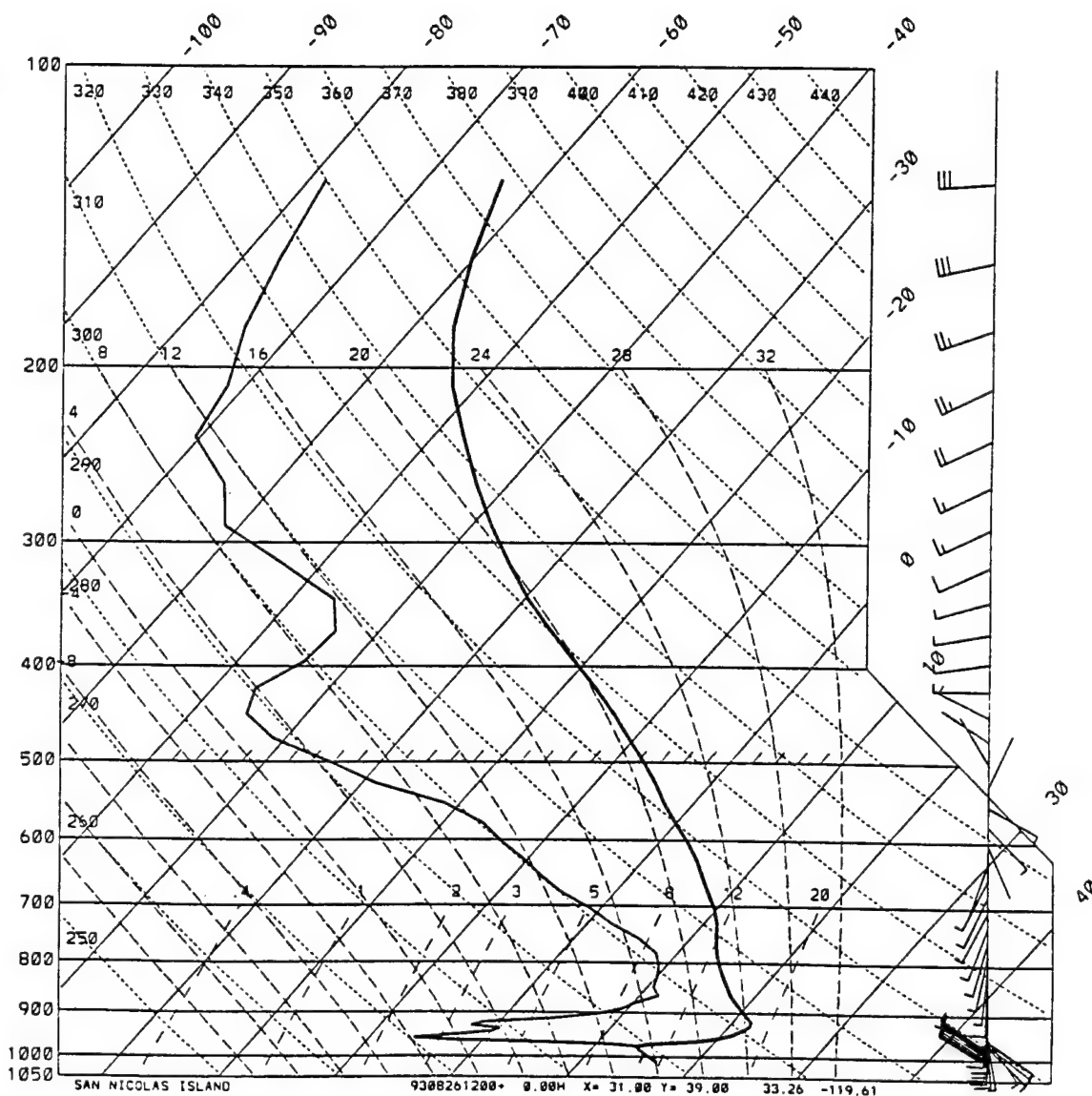


Figure 5.17 San Nicolas Island simulated Skew-T diagram, 1200z, 26 August, 1993. Moistening of the atmosphere above the MBL continues, resulting in a shallow dry layer just above the MBL. Also, the inversion base has lowered to around 975 mb.

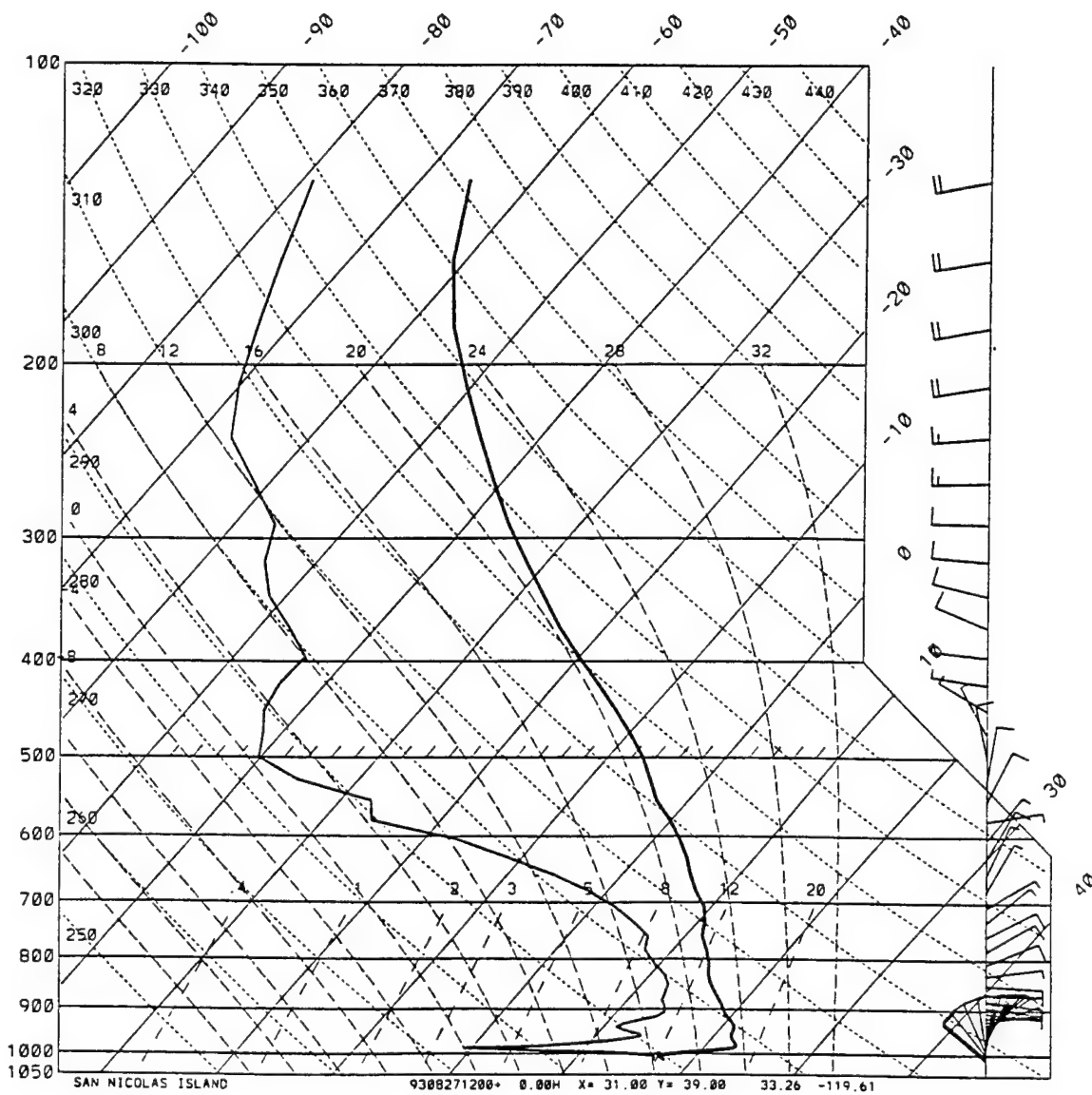


Figure 5.18 San Nicolas Island simulated Skew-T diagram, 1200z, 27 August, 1993. The deep layer of southerly flow has evolved into easterly flow from 580-925 mb. The remarkably thin dry layer atop the MBL persists and the inversion base is near 1000 mb.

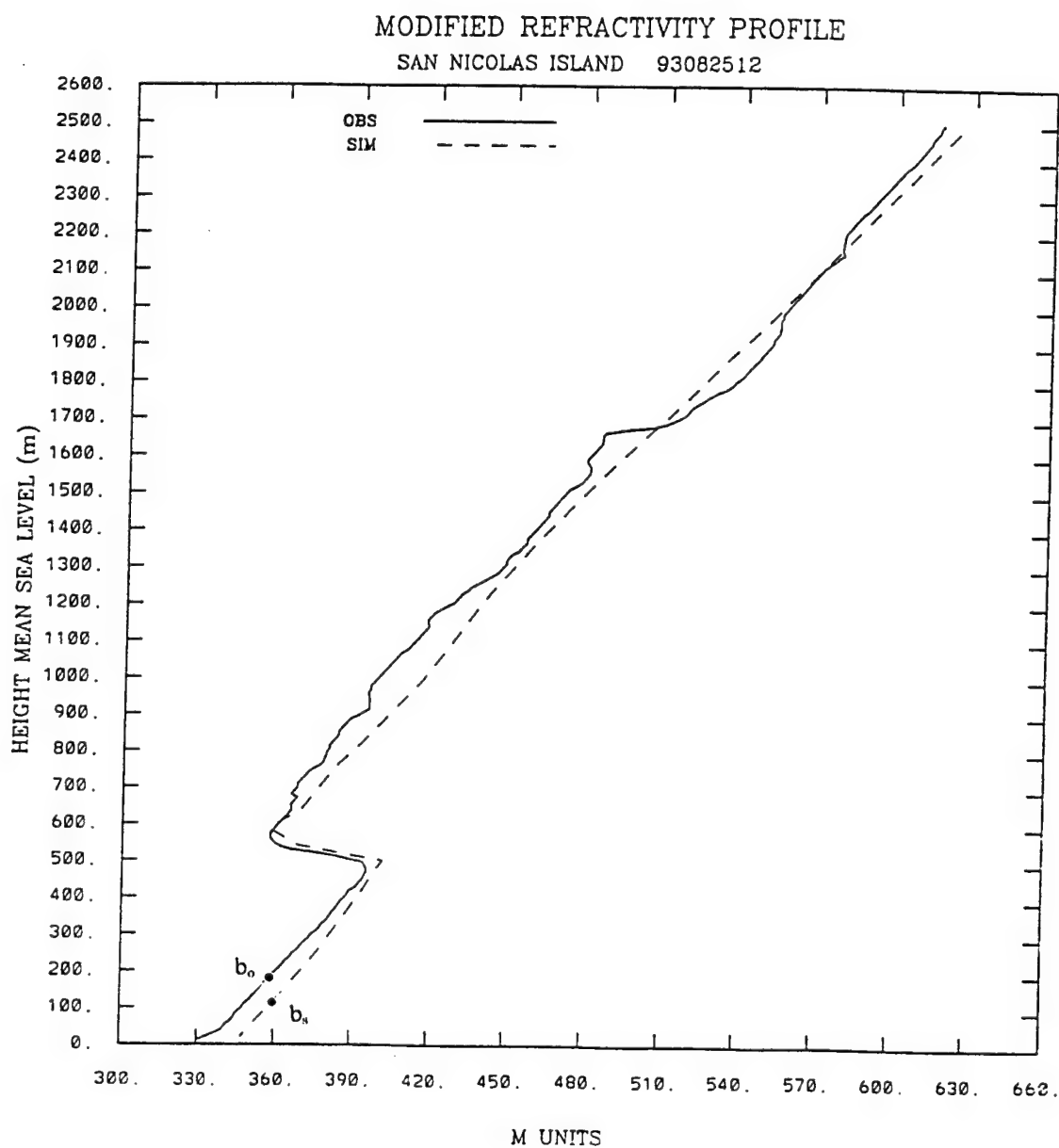


Figure 5.19 Observed (solid) and simulated (dashed) modified refractivity profiles for San Nicolas Island, 25 August, 1200z. An elevated duct exists from approximately 180-550 m. (b_o is the observed duct base, b_s is the simulated duct base)

demonstrates the model's ability to forecast ducting conditions 12 hours after the end of the dynamic initialization period (Fig. 5.19). One day later, the observed trapping layer base had dropped nearly 200 m and the duct base lowered to the surface (Fig. 5.20). Thereafter, the trapping layer base continued to drop another 150 m by 27 August 1200z (Fig. 5.21), when the observed M-profile exhibits a very sharp minimum near 225 m above ground level (AGL). The trapping layer at this time is only about 20-30 m deep, which can be detected only because of the very fine vertical resolution of the research quality soundings obtained during VOCAR (Fig. 4.15). The evolution of the M-profile in these three figures, especially the compression of the M inversion, underscores the importance of the mesoscale processes affecting the thin dry layer just above the MBL. The model's ability to simulate the evolution of the M-profile after 60 hrs of integration is quite impressive (Fig. 5.21), especially considering that its greatest vertical resolution (40 m layers) extends only to 600 m AGL.

Finally, the spatial variability of the modified refractive index is examined. Recall that modified refractivity in standard atmospheric conditions is monotonic with respect to height (see Fig. 1.1). In a vertical cross-section with potential trapping layers, however, $dM/dz < 0$ and $M(z)$ is no longer monotonic, so the isopleths of modified refractivity can "fold" over themselves. This M-field "folding" is evident in the north-south vertical cross-sections of the simulated modified refractivity field (Figs. 5.22-5.24). This series of figures also demonstrates the mesoscale structure and temporal evolution of the trapping layer and duct in the cross-section, as they evolved from an elevated-duct condition (Fig. 5.22) to a surface-duct condition (Figs. 5.23 and 5.24). These cross-sections reveal that

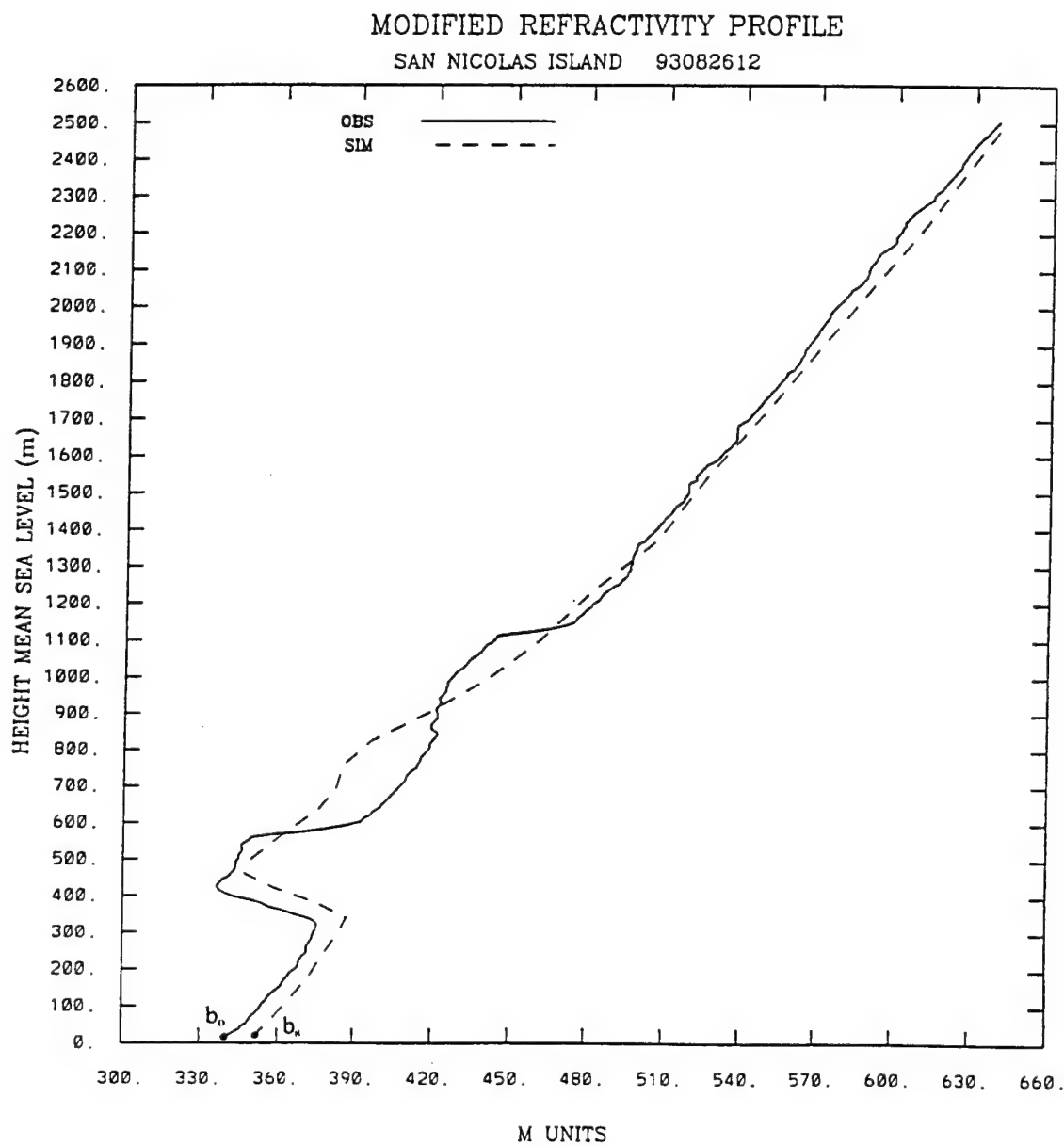


Figure 5.20 Observed (solid) and simulated (dashed) modified refractivity profiles for San Nicolas Island, 26 August, 1200z. A surface duct extends to approximately 415 m. The simulated profile is after 36 hrs of integration. (b_o is the observed duct base, b_s is the simulated duct base)

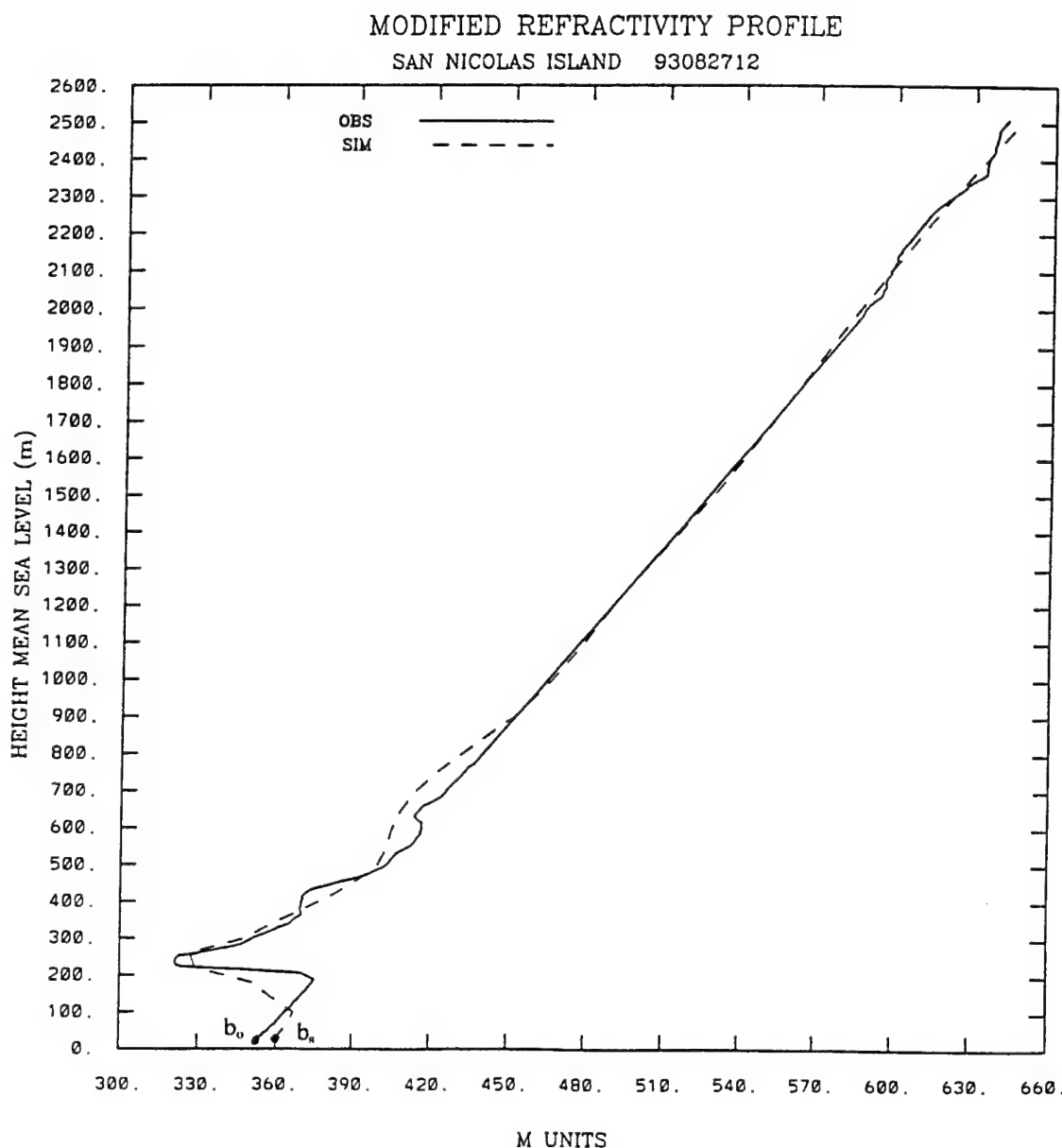


Figure 5.21 Observed (solid) and simulated (dashed) modified refractivity profiles for San Nicolas Island, 27 August, 1200z. A surface duct extends to approximately 220 m. The simulated profile is after 60 hrs of integration. (b_o is the observed duct base, b_s is the simulated duct base)

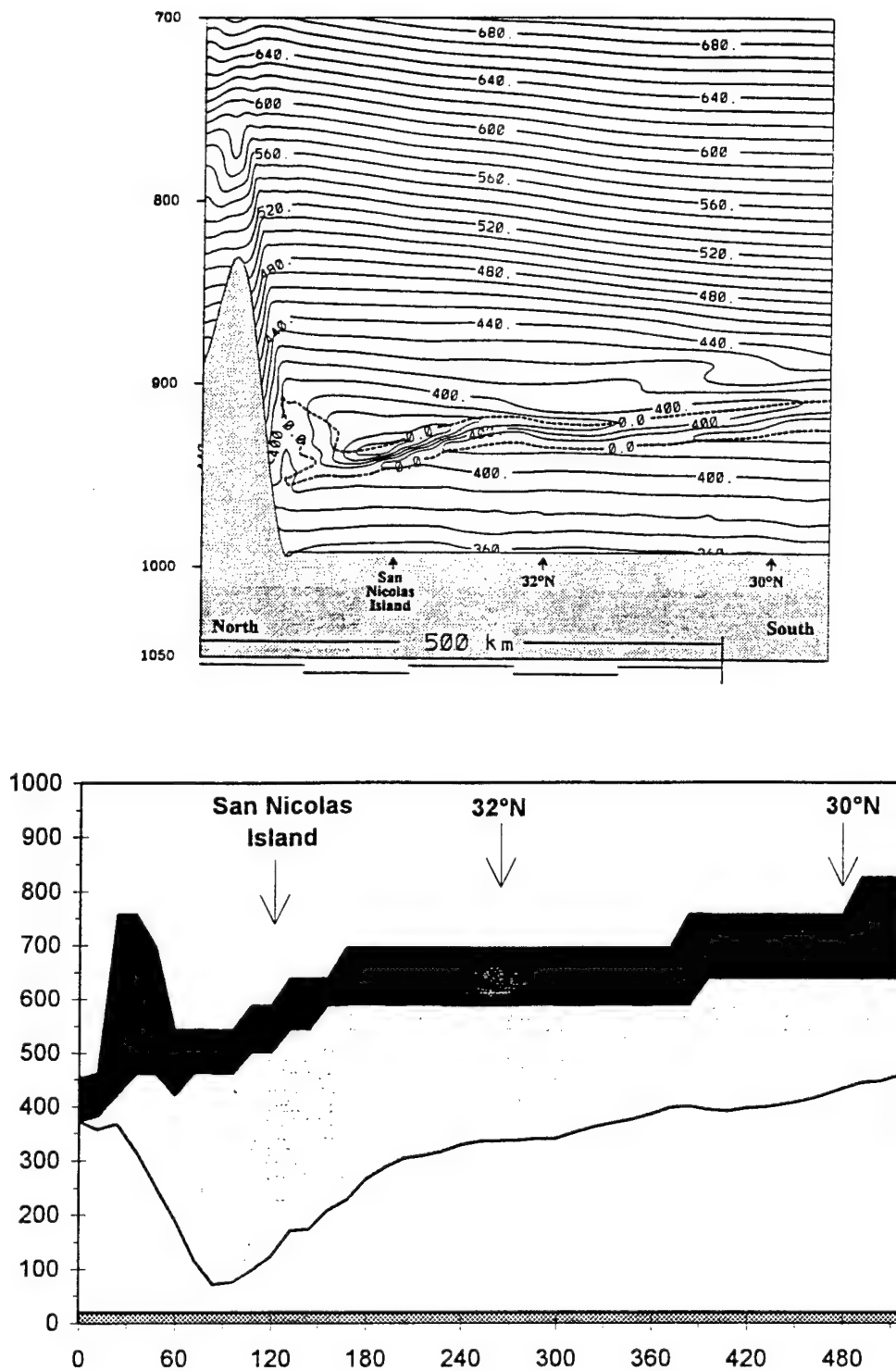


Figure 5.22 North to south cross-section of simulated modified refractivity (top, contour interval 10 M units), simulated trapping layer (top, dashed), and simulated refractive structure (bottom, trapping layer is the dark band, EM duct is the light band) on 25 August, 1200z.

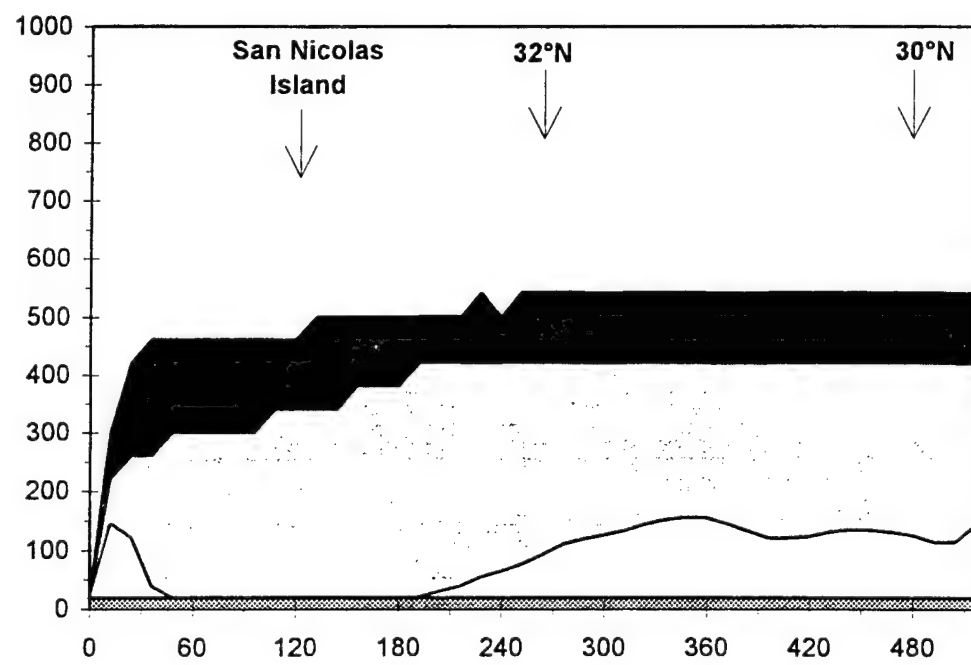
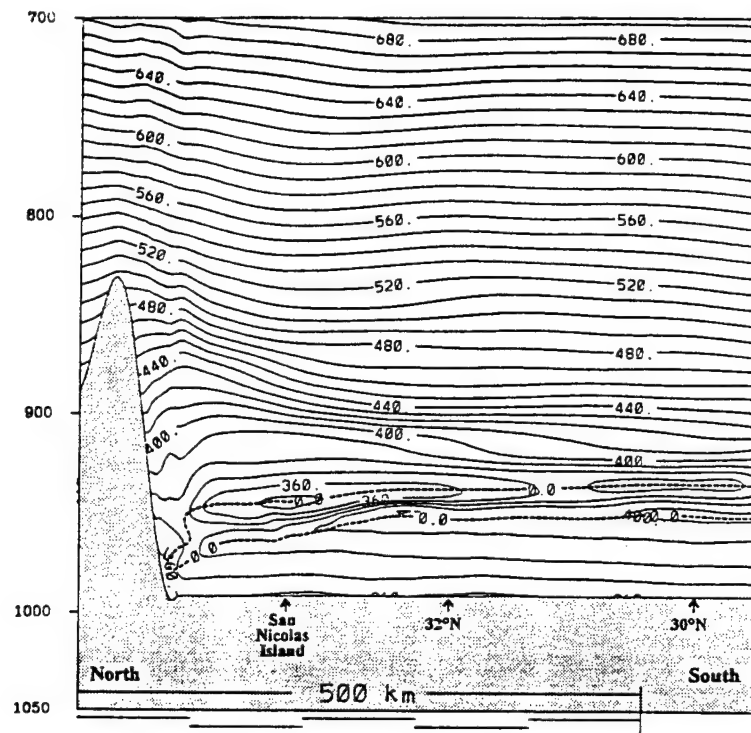


Figure 5.23 North to south cross-section of simulated modified refractivity (top, contour interval 10 M units), simulated trapping layer (top, dashed), and simulated refractive structure (bottom, trapping layer is the dark band, EM duct is the light band) on 26 August, 1200z.

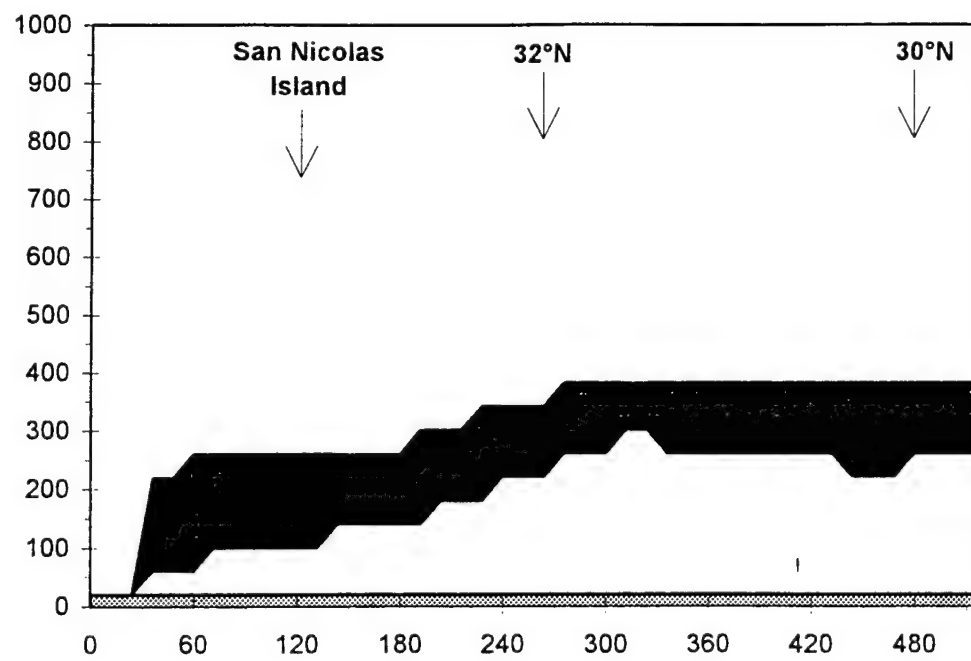
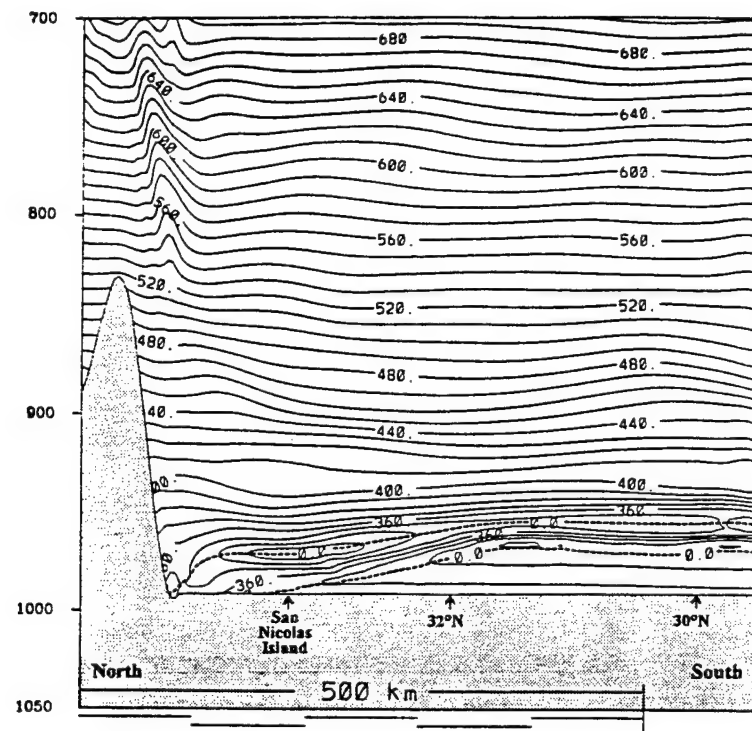


Figure 5.24 North to south cross-section of simulated modified refractivity (top, contour interval 10 M units), simulated trapping layer (top, dashed), and simulated refractive structure (bottom, trapping layer is the dark band, EM duct is the light band) on 27 August, 1200z.

the mesoscale spatial variability of the ducting characteristics is forecasted to be quite significant. An ability to accurately predict the primary aspects of this spatial and temporal variability in real time clearly provides an advantage for a variety of remote sensing and communications related applications.

5.3 Gravity Waves.

Although it is critical to understand how the temporal evolution and spatial structure of the trapping and ducting layer are dependent on the synoptic and mesoscale development, the impact of even smaller-scale processes on the modified refractivity field is also of vital importance. In addition to the effects of turbulence, it is hypothesized that an important cause of these smaller-scale disturbances is internal gravity waves propagating along the MBL top. The phenomenon of gravity wave propagation along the interface of two fluids with differing densities, such as the cool, moist MBL and the warm, dry air atop the MBL is well known and has been studied by Klemp et al. (1995). To investigate the presence of gravity waves in the 12 km domain and to gain insight into potential amplitudes and periods, MM5v1 output (with ten minute frequency) was animated using 3-D visualization software. While computer animation cannot be included here, the important results can be summarized using model generated cross-sections taken along the direction of propagation.

Based on this diagnosis, Figs. 5.25-5.26 present the modified refractivity field and vertical velocity for a train of gravity waves traveling from the Baja peninsula towards the west-southwest (see Fig. 5.4) over a three hour period on 27 August. The “folded”

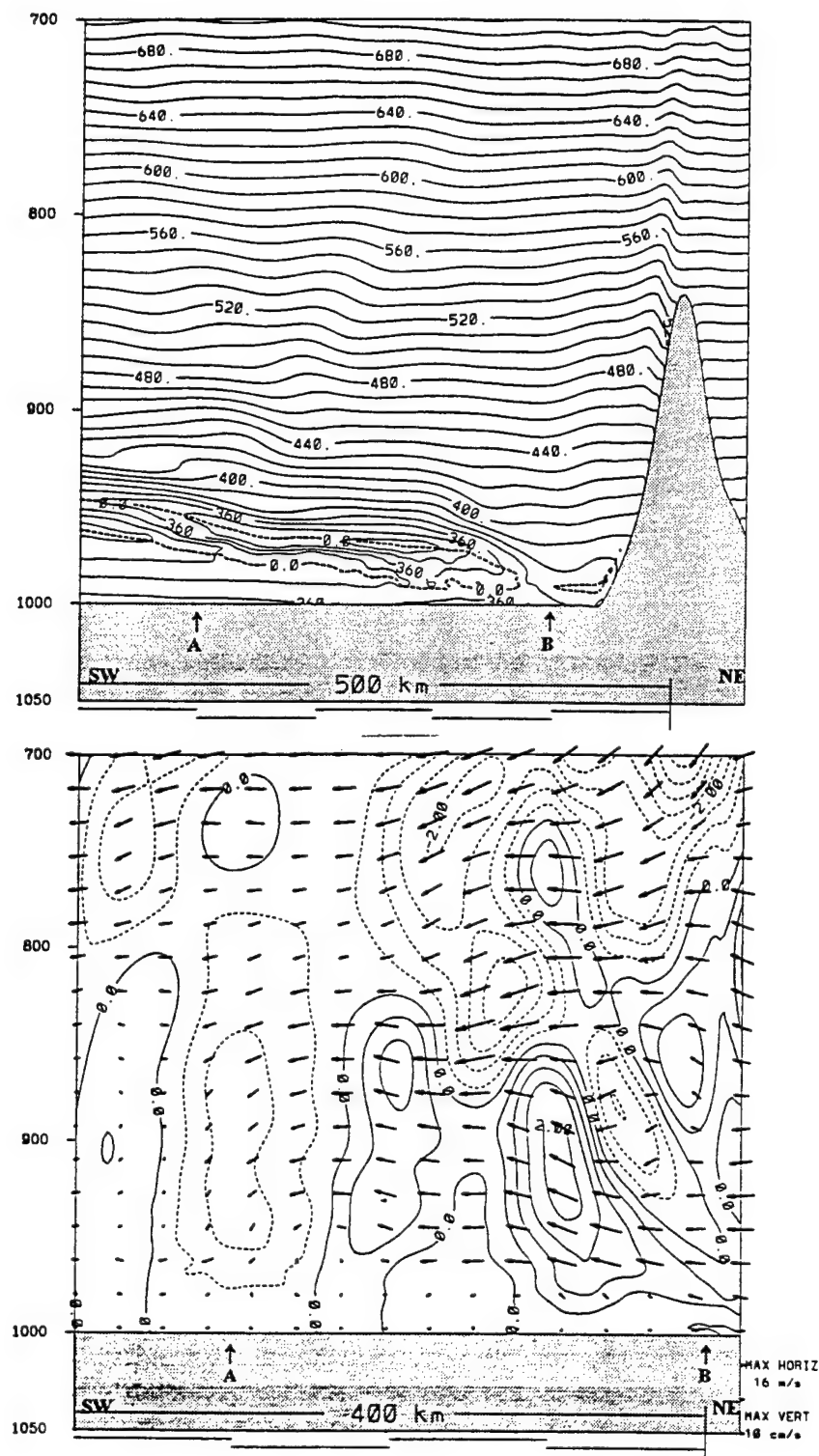


Figure 5.25 Southwest to Northeast cross-section through Baja of simulated modified refractivity (top, contour interval 10 M units), simulated trapping layer (top, dashed), simulated vertical velocity (bottom, contour interval 0.5 cm s⁻¹), and wind vectors in the plane on 27 August, 0700z. Note: positive vertical velocities (solid), negative vertical velocities (dashed).

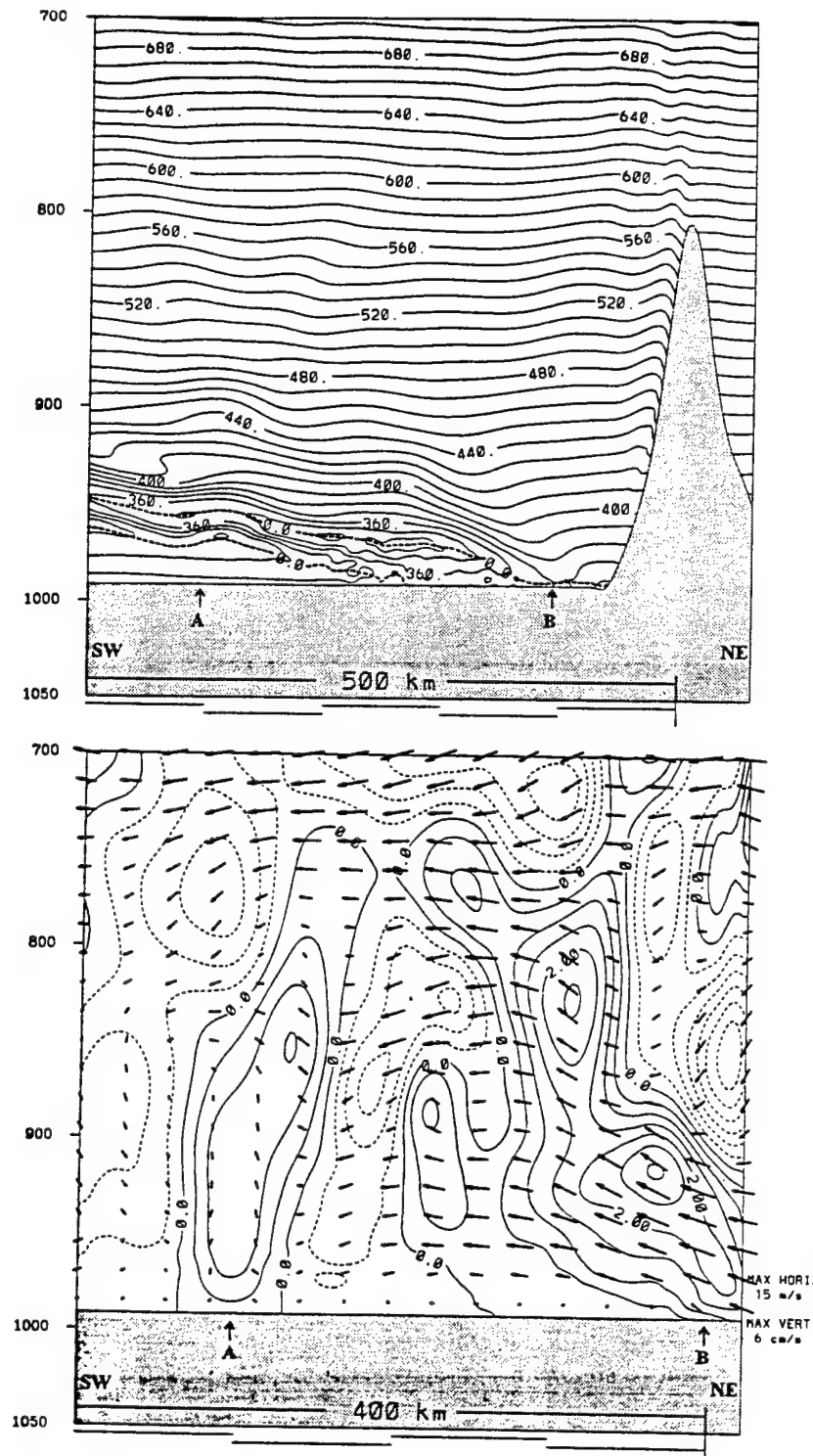


Figure 5.26 Southwest to Northeast cross-section through Baja of simulated modified refractivity (top, contour interval 10 M units), simulated trapping layer (top, dashed), simulated vertical velocity (bottom, contour interval 0.5 cm s^{-1}), and wind vectors in the plane on 27 August, 1000z. Note: positive vertical velocities (solid), negative vertical velocities (dashed).

structure of the M field in the lower portion of Fig. 5.25 produces an EM trapping layer at 0700z, enclosed by the heavy dashed line. Over the ocean, the vertical velocity field, M field, and the trapping layer exhibit a crest-trough-crest wave pattern with a dominant horizontal wavelength of about 120-160 km. This particular pattern can be followed over the next three hours as the wave propagates southwestward with a phase speed on the order of 9.3 m s^{-1} and a period of approximately 4.8 hours. Over the three hour example shown here, the wave pattern has shifted about one-half wavelength (80 km). These propagating gravity waves caused a local displacement of the trapping layer top and base on the order of 64 m at 30°N . This rise in the trapping layer at 30°N corresponds to a mean vertical advection rate of 0.6 cm s^{-1} . Also, in the near-shore region (littoral) (Pt. B, Figs. 5.25-5.26), the trapping layer periodically breaks into discontinuous segments and then becomes re-established as the gravity waves leave the coastline. Naturally, these changes in the trapping layer can lead to periodicity in the ducting characteristics of the marine environment.

Preliminary analysis indicates that the weakening remnants of Tropical Storm Hilary, discussed in the previous section, is the cause of these gravity waves. The tropical storm had been downgraded to a tropical depression by 1200z, 26 August and further weakened into a low pressure system by 1200z, 27 August (see Fig. 4.8). Simulated wind fields at 420 m above the ground demonstrate the northward progression of the weakening low pressure system and its associated cyclonic winds (Figs. 5.27-5.29). Fig. 5.27 shows 20 m s^{-1} easterly winds impinging upon the Baja mountains, averaging 1000 m elevation with peaks near 1800 m. The strong flow continues as the cyclone center

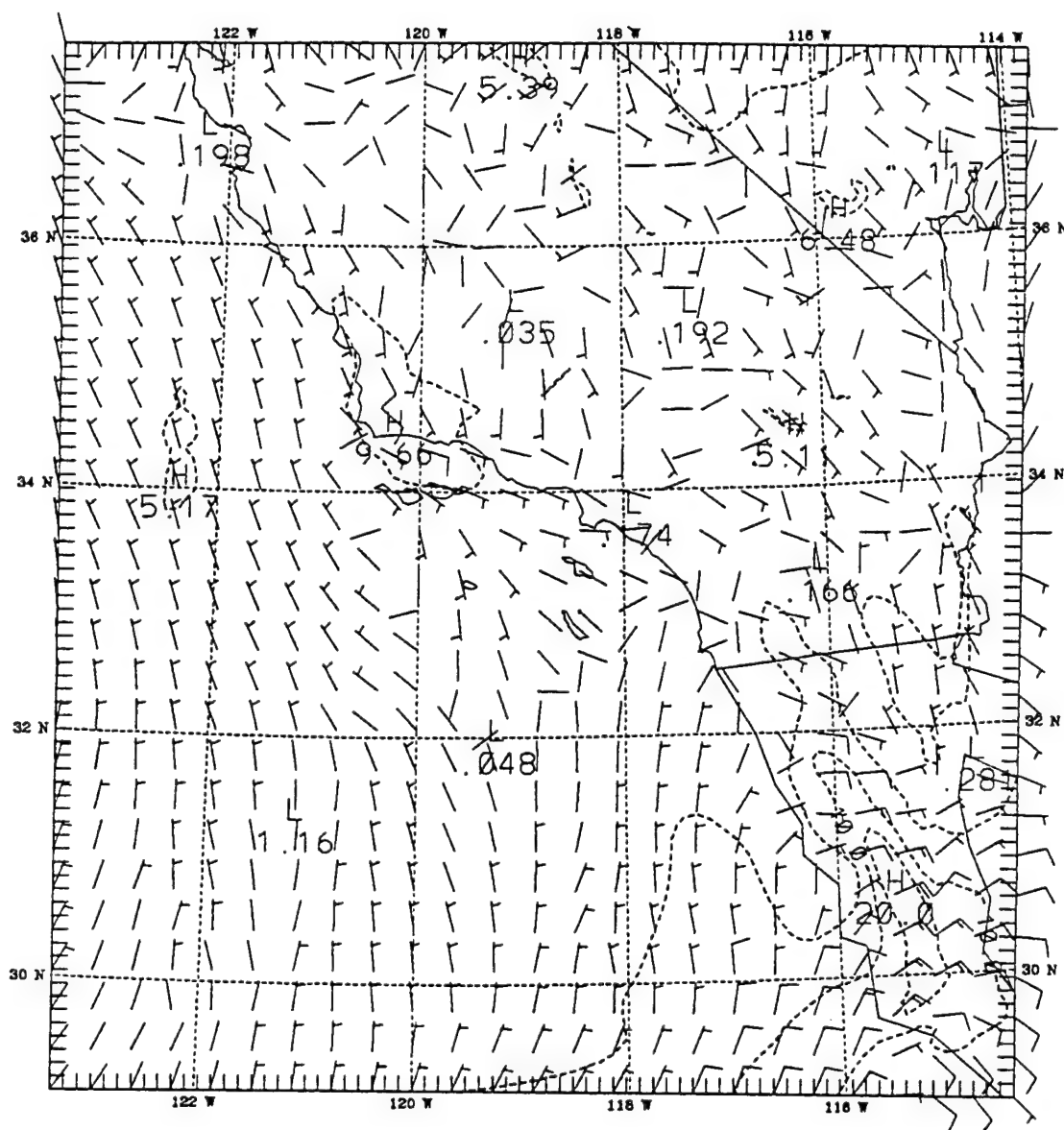


Figure 5.27 Wind field at 400 m AGL on 26 August, 1800z. The region of strongest velocities is over the Baja Peninsula. Isotach contour interval is 5 m s^{-1} .

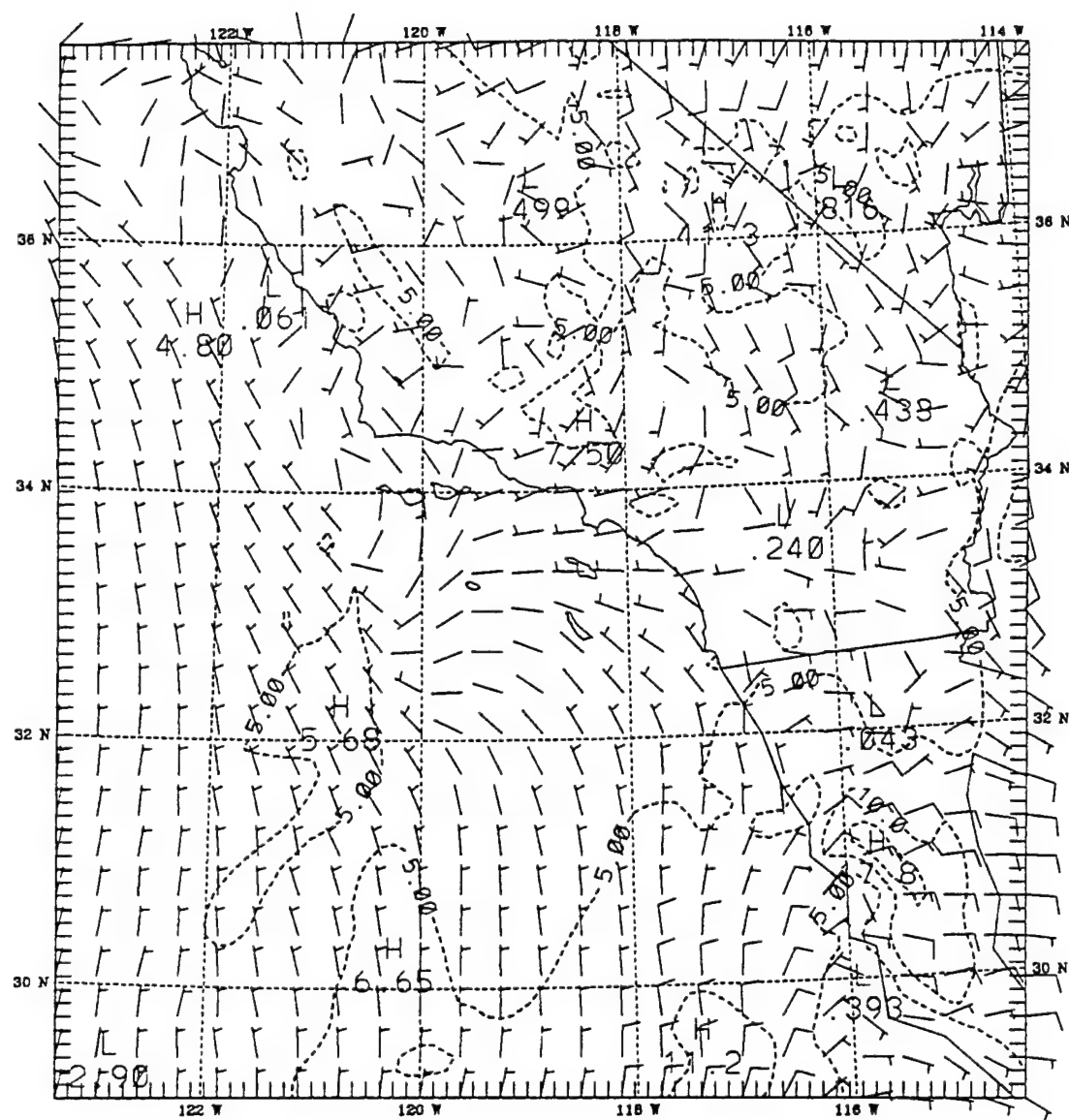


Figure 5.28 Wind field at 400 m AGL on 27 August, 0000z. The region of strongest velocities is over the Baja Peninsula. Isotach contour interval is 5 m s^{-1} .

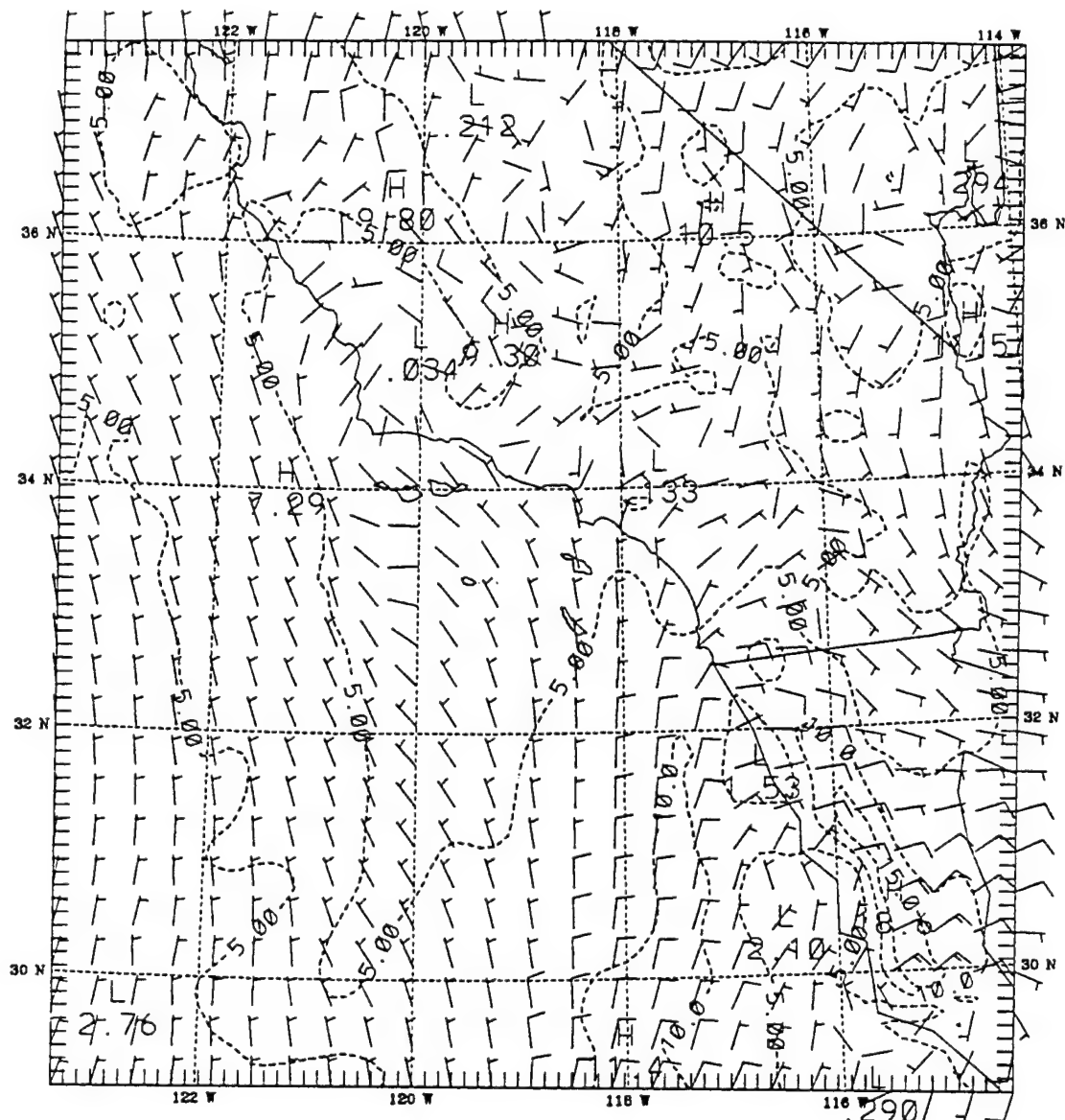


Figure 5.29 Wind field at 400 m AGL on 27 August, 0600z. The region of strongest velocities is over the Baja Peninsula. Isotach contour interval is 5 m s⁻¹.

eventually appears in the domain at 0600z, 27 August (Fig. 5.29). Although the storm was weakening in this period, strong vertical motions associated with the storm were enhanced by strong horizontal winds flowing over and around the mountainous Baja terrain thereby inducing gravity waves on the leeward (oceanward) side of the Baja peninsula.

A second case of gravity wave propagation was analyzed for a west-east cross-section through San Nicolas Island (see Fig. 5.4) approximately 360 km north of the Baja cross-section. These VOCAR area gravity waves (Figs. 5.30-5.31) occurred at the same time as those in the Baja area (Figs. 5.25-5.26), but are well north of the strong cyclonic circulation of the dying tropical depression. In this example, gravity waves with wavelengths averaging 224 km were detected propagating westward from the coast with phase speeds on the order of 13.5 m s^{-1} . These waves have a period of nearly 4.6 hours with a maximum local trapping layer displacement of 67 m in a 2 hour period (0.9 cm s^{-1}). Although the triggering mechanism for this train of gravity waves is not clearly understood, preliminary analysis indicates that wind/terrain interactions are a likely cause.

While the phase speed (higher) and wavelength (longer) of the VOCAR area gravity waves differ from those detected propagating away from the Baja peninsula, both examples point to modulations in the EM trapping, and hence ducting, layers over the ocean. Finally, the model grid used here (12 km) has, by definition, a resolution limit of 24 km, and waves shorter than 50-60 km are unlikely to be resolved well. Thus, the potential exists that even shorter gravity waves may affect EM propagation, but which remain unresolved in these experiments.

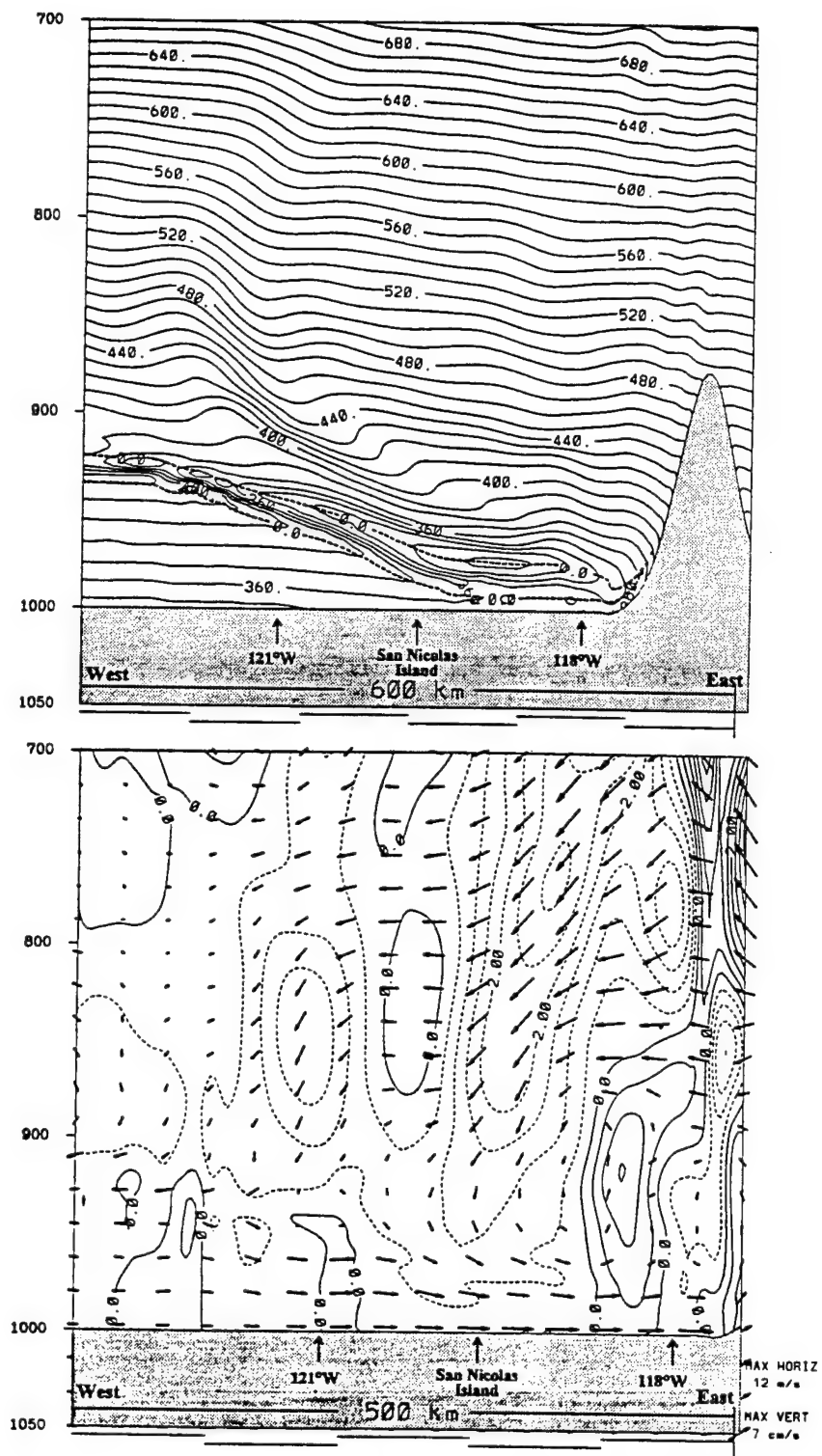


Figure 5.30 West to East cross-section through San Nicolas Island of simulated modified refractivity (top, contour interval 10 M units), simulated trapping layer (top, dashed), simulated vertical velocity (bottom, contour interval 0.5 cm s^{-1}), and wind vectors in the plane on 27 August, 0700z. Note: positive vertical velocities (solid), negative vertical velocities (dashed).

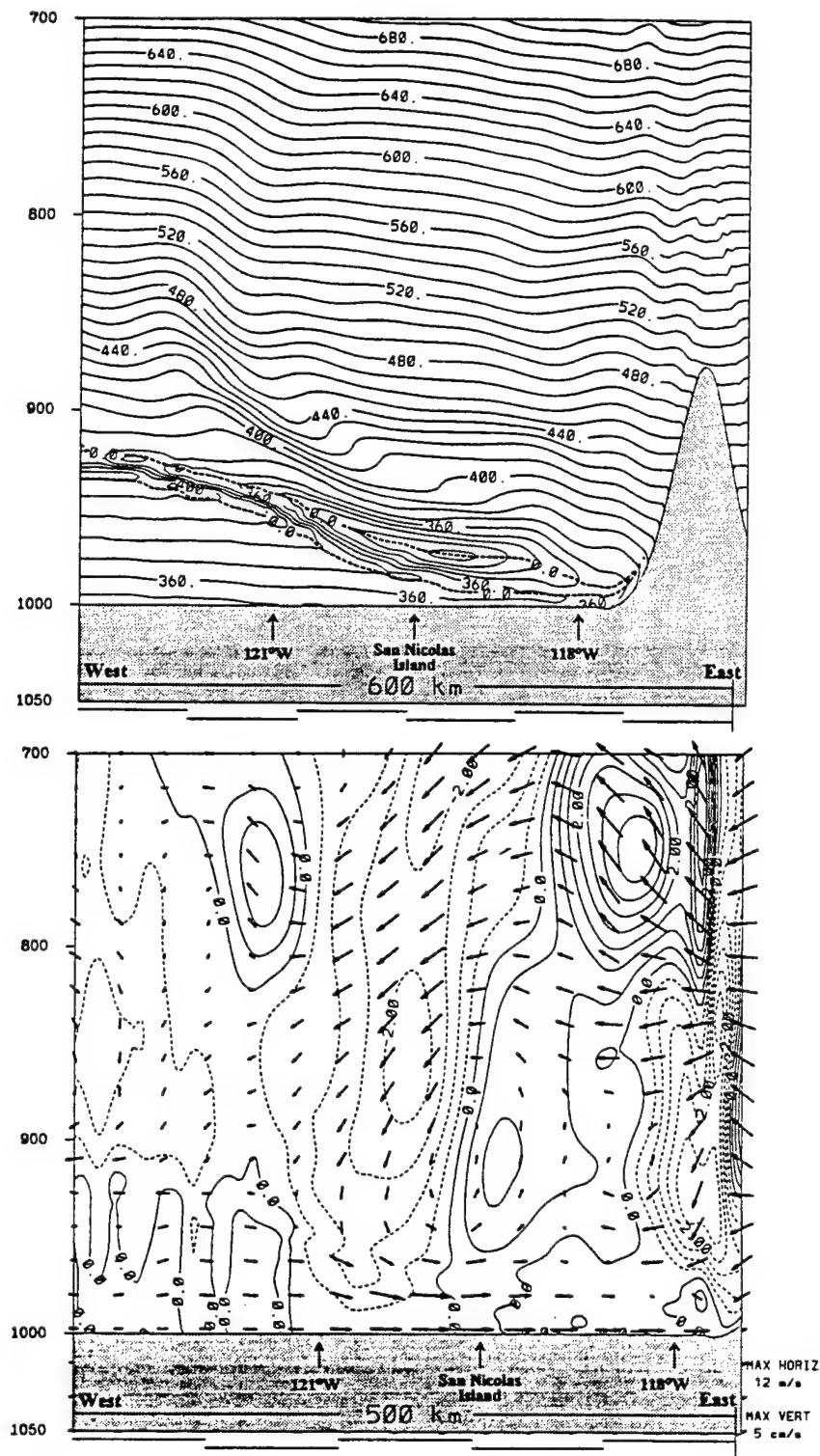


Figure 5.31 West to East cross-section through San Nicolas Island of simulated modified refractivity (top, contour interval 10 M units), simulated trapping layer (top, dashed), simulated vertical velocity (bottom, contour interval 0.5 cm s^{-1}), and wind vectors in the plane on 27 August, 0900z. Note: positive vertical velocities (solid), negative vertical velocities (dashed).

Chapter 6

SUMMARY AND CONCLUSIONS

Temporally and spatially varying 3-D meteorological fields determine the atmosphere's 3-D refractive index field, which affects the propagation of electromagnetic (EM) waves in the atmosphere. EM propagation models can accurately predict the behavior of propagating radio waves and microwaves if they have reliable fields of total atmospheric pressure (p), temperature (T), and atmospheric vapor pressure (e). Initialization of these propagation models with relatively few meteorological upper air observations, however, generates inferior modified refractivity (M) profiles that fail to accurately represent wave propagation and ducting characteristics over a relatively large domain. As expected, this weakness in the initialization process is compounded in data void areas, especially over oceans and in the littoral, where the most detailed M profiles are required.

A further complication in the analysis and prediction of accurate M profiles in these regions is the generally poor performance of numerical meteorological models in representing the MBL structure. Aside from sparse data availability, several numerical factors contribute to degraded MBL predictions. Typically, synoptic-scale and mesoscale models are not configured with sufficient vertical resolution to resolve the generally shallow MBL structures which often contain very strong vertical gradients of temperature and water vapor. Also, while vertical diffusion is necessary for computational stability, application of a vertical diffusion that is too strong can weaken and smooth these sharp

moisture gradients which contribute greatly to EM ducting conditions. Finally, insufficient horizontal resolution may limit the ability to simulate important variability in the key fields, including the propagation of gravity waves.

In addition to these numerical factors, several physical processes also play a key role in developing realistic MBL structure in an atmospheric model. Among these processes, heat and moisture fluxes from the underlying ocean surface and cloud top radiational cooling are not resolved explicitly and must be parameterized. Since cloud top radiational cooling plays such a strong role in MBL development, a model's radiation and cloud schemes are of particular importance. Specifically, realistic interaction of shortwave absorption (heating) and longwave emission (cooling) by both stratus and stratocumulus topped marine boundary layers is essential. As such, radiation schemes should incorporate the effects of drop size distributions consistent with observations in both stratus and stratocumulus clouds.

This research demonstrates that mesoscale atmospheric numerical models are a potentially important source of information to assist in determining the refractivity structure, both spatially and temporally. In this study, MM5v1 was configured with 53 computational layers (40 m vertical resolution in the MBL) on three mesh sizes (108, 36, and 12 km). A dynamic MBL initialization scheme (Leidner 1995) was used to construct representative MBL structure in a 12 hour pre-forecast period. Upper level (≥ 850 mb) winds, temperature, and moisture were nudged toward 12 hourly NWS gridded global analyses on the 108 and 36 km domains to ensure the 7 day simulation remained in phase with synoptic scale features. The background vertical diffusion was reduced to $0.01 \text{ m}^2 \text{ s}^{-1}$

on all sigma levels and the MBL cloud top absorption of shortwave radiation was limited to 1/3 of the longwave cooling rate as discussed in Chapter 3. The Blackadar HIRPBL (Blackadar 1976, 1979, Zhang and Anthes 1982) was used to parameterize boundary layer processes.

The period of interest for this investigation, 24-31 August 1993, was during the VOCAR study and was marked by enhanced synoptic scale subsidence from the East Pacific Ridge early in the episode, a mesoscale Tropical Storm, and smaller scale internal gravity waves. Special observations of the MBL, trapping layer, and ducting layer heights from VOCAR indicate a long term variation characterized by decreasing heights in the first three days of the study period. In the final portion of the period, these heights increase with time. On August 26-27, radiosondes over the VOCAR area revealed a sharp, thin, dry "spike" just above the MBL. This feature was also detected in dropsondes at the same times and locations. Observed M profiles showed that the EM duct had a complex structure that varied in space and time, and which evolved from an elevated duct to a surface based duct, and then lifted to become an elevated duct again later in the period. A spectral analysis of the movement of the trapping layer at San Nicolas Island indicated a weak to moderate diurnal signal in the refractivity structure, but Camp Pendleton (on the coast) appears to have stronger diurnal forcing.

Comparison of the atmospheric mesoscale model simulations with the observations led to the following conclusions:

- An advanced mesoscale numerical weather prediction system (MM5v1 in this case), with appropriate numerics, physics, and sufficient vertical resolution can accurately represent the 3-D Modified Refractivity field in the California Bight.
- A mesoscale numerical weather prediction system can provide high resolution meteorological quantities required to accurately forecast many aspects of the 3-D modified refractivity field 3 to 4 days in advance.
- The MM5 model captured the long term synoptic-scale trend in the meteorological fields, which were found to be strongly forced by changes in the strength of the large scale subsidence rate. In particular, the subsidence rate is a major factor in determining the height of the MBL, and hence, the EM trapping layer base, duct base, and duct top.
- Mesoscale diurnal effects can enhance the local near shore subsidence rate, especially during the afternoon, and aid in the lowering of the MBL. This enhanced subsidence in turn affects the M field. In the week of August 24-31, however, the diurnal effects appear to be secondary to the large scale subsidence rate.
- Internal gravity waves were detected in the MM5 12 km solutions. These waves propagate along the top of the MBL with phase speeds ranging from $9-14 \text{ m s}^{-1}$,

wavelengths from 120-250 km, and a period of about 4-5 hours. Perturbations in the vertical velocity field extend up to at least 700 mb, with w -amplitudes of about 0.01 m s⁻¹ at 950 mb, near the height of the EM trapping layer. This results in a local vertical displacement of the EM trapping layer and the duct on order of 50-70 m as the waves pass.

Areas of future work should include sensitivity testing using various boundary layer schemes, simulations on a finer mesh, and improved cloud and radiation models. It is possible that a Turbulent Kinetic Energy (TKE) approach to the MBL would enable the model to better predict M profiles. In addition, investigations using a spectral representation of the MBL structure (Otte and Wyngaard 1996) suggest that the inversion layer structure at the top of the MBL could be parameterized more realistically, as well. If successful, this would allow more accurate prediction of the trapping layer structure and the duct. Simulations on a 4 km grid would provide better resolution of coastal dynamics. With this improved resolution, investigation of sea breeze effects and gravity wave propagation would be more accurate and could allow evaluation of forcing mechanisms that ultimately affect the refractivity conditions. Application of enhanced cloud and radiation schemes that provide more realistic treatment of effects due to MBL stratus and stratocumulus is essential to the prediction of MBL structure and should receive additional study. Finally, advanced mesoscale models need to be linked with large-eddy simulations in order to represent the full range of variability, including turbulence, needed to account for the observed variation of received signal strength in ducting conditions.

REFERENCES

Babin, S. M., 1995: A case study of subrefractive conditions at Wallops Island, Virginia. *J. Appl. Meteor.*, **34**, 1028-1038.

Bean, B. R., and E. J. Dutton, 1966. Radio Meteorology. Natl. Bur. Stand., Monogr. 92, Supt. Doc. U. S. Govt. Printing Office, Washington, D. C.

Beardsly, R. C., C. E. Dorman, C. A. Friehe, L. K. Rosenfeld and C. D. Winant, 1987: Local atmospheric forcing during the Coastal Ocean Dynamics Experiment 1. A description of the marine boundary layer and atmospheric conditions over a northern California upwelling region. *JGR*, **92**, 1467-1488.

Bechtold, P., C. Fravalo and J. P. Pinty, 1992: A model of marine boundary-layer cloudiness for mesoscale applications. *J. Atmos. Sci.*, **49**, 1723-1744.

Blackadar, A. K., 1976: Modeling the nocturnal boundary layer. *Preprints of Third Symposium on Atmospheric Turbulence and Air Quality*, Raleigh, NC, 19-22 October 1976, Amer. Meteo. Soc., Boston, 46-49.

Blackadar, A. K., 1979: High resolution models of the planetary boundary layer. *Advances in Environmental Science and Engineering*, 1, No. 1. Pfafflin and Ziegler, Eds., Gordon and Breach Sci. Publ., New York, 50-85.

Bretherton, C. S., 1994: A turbulence closure model of marine stratocumulus clouds. Part I: The diurnal cycle of marine stratocumulus during FIRE 1987. *J. Atmos. Sci.*, submitted.

Bridger, A. F. C., W. C. Brick and P. F. Lester, 1993: The structure of the marine inversion off the Central California Coast: Mesoscale conditions. *Mon. Wea. Rev.*, **121**, 335-351.

Brost, R. A., D. H. Lenschow and J. C. Wyngaard, 1982: Marine stratocumulus layers. Part I: Mean conditions. *J. Atmos. Sci.*, **39**, 800-817.

Burk, S. D. and W. T. Thompson, 1997: Mesoscale modeling of summertime refractive conditions in the Southern California Bight. *J. Appl. Meteor.*, **36**, 22 pp.

Davies, R. and A. R. Alves, 1989: Flux divergence of thermal radiation within stratiform clouds. *J. Geophys. Res.*, **94**(D13), 16,277-16,286.

Doviak, R. J. and D. S. Zrnic', 1993. *Doppler Radar and Weather Observations*. Academic Press, Inc., 10 pp.

Dudhia, J., 1989: Numerical study of convection observed during the winter monsoon experiment using a mesoscale two-dimensional model. *J. Atmos. Sci.*, **46**, 3077-3107.

Dudhia, J., 1993: A nonhydrostatic version of the Penn State-NCAR Mesoscale Model: Validation tests and simulation of an Atlantic cyclone and cold front. *Mon. Wea. Rev.*, **121**, 1493-1513.

Duynkerke, P. G. and P. Hignett, 1993: Simulation of diurnal variation in a stratocumulus-capped marine boundary layer during FIRE. *Mon. Wea. Rev.*, **121**, 3291-3300.

Elliot, D. L. and J. J. O'Brien, 1977: Observational studies of the marine boundary layer over an upwelling region. *Mon. Wea. Rev.*, **105**, 86-98.

Grell, G. A., J. Dudhia and D. R. Stauffer: 1994: *A Description of the Fifth-Generation Penn State/NCAR Mesoscale Model (MM5)*. NCAR Technical Note 398+STR, National Center for Atmospheric Research, Boulder, CO, 138 pp.

Hittney, H. V. and J. H. Richter, 1976: Integrated refractive effects prediction system (IREPS). *Nav. Eng. J.*, **88**, 257-262.

Klemp, J. B., R. Rotunno, and W. C. Skamarock, 1995: Shallow-water model simulations of coastally trapped disturbances. *Preprints of Seventh Conference on Mountain Meteorology*, Amer. Meteo. Soc., Boston, 197-202.

Lacis, A. L. and J. E. Hansen, 1974: A parameterization of the absorption of solar radiation in the earth's atmosphere. *J. Atmos. Sci.*, **31**, 118-133.

Leidner, S. M., 1995: *Improving California Coastal-Zone Numerical Weather Prediction by Dynamic Initialization of the Marine Boundary Layer*, The Graduate School, The Pennsylvania State University, 30 pp.

Oliver, D. A., W. S. Lewellen, and G. G. Williamson, 1978: The interaction between turbulent and radiative transport in the development of fog and low-level stratus. *J. Atmos. Sci.*, **35**, 301-316.

Otte, M. J. and J. C. Wyngaard, 1996: A general framework for an "unmixed-layer" PBL model. *J. Atmos. Sci.*, **53**, 2652-2670.

Neiburger, M., D. Johnson and C. Chien, 1961: *Studies of the Structure of the Atmosphere over the Eastern Pacific Ocean in Summer: I Inversion Over the Eastern North Pacific Ocean*, Univ. Calif. Publ. Meteor., **1**, No. 1, 94 pp.

Richter, J. H., 1994: Relevance of decision aids to the new NATO strategy in Propagation, Modelling, and Decision Aids for Communications, Radar, and Navigation Systems. AGARD-LS-196, Paper 6.

Rogers, C. D., 1967: The radiative heat budget of the troposphere and lower stratosphere. Rept. No. A2, Planetary Circulations Project, Dept. of Meteorology, M.I.T., 99 pp.

Sauvageot, H., 1992. *Radar Meteorology*. Artech House, Inc., 35 pp.

Seaman, N. L., D. R. Stauffer, and A. M. Lario-Gibbs, 1995: A multiscale four dimensional data assimilation system applied in the San Joaquin valley during SARMAP: Part I: Modeling design and basic performance characteristics. *J. Appl. Meteor.*, **34**, 1739-1761.

Stauffer, D. R., and N. L. Seaman, 1994: Multiscale four-dimensional data assimilation. *J. Appl. Meteor.*, **33**, 416-434.

Stephens, G. L., 1978: Radiation profiles in extended water clouds. I: Theory. *J. Atmos. Sci.*, **35**, 2111-2122.

Stephens, G. L., 1984: The parameterization of radiation for numerical weather prediction and climate models. *Mon. Wea. Rev.*, **112**, 826-867.

Zhang, D. -L., and R. A. Anthes, 1982: A high-resolution model of the planetary boundary layer-sensitivity test and comparison with SESAME-79 data. *J. Appl. Meteor.*, **114**, 1330-1339.